High-Frequency Modeling and Analyses for Buck and Multiphase Buck Converters

Yang Qiu

Dissertation submitted to the Faculty of the
Virginia Polytechnic Institute and State University
in partial fulfillment of the requirements for the degree of

Doctor of Philosophy
in
Electrical Engineering

Fred C. Lee, Chairman
Daan van Wyk
Ming Xu
Yilu Liu
Guo-Quan Lu

November 30th, 2005
Blacksburg, Virginia

Keywords: high frequency, sideband effect, multi-frequency model, buck converter, multiphase

High-Frequency Modeling and Analyses for Buck and Multiphase Buck Converters

Yang Qiu

(Abstract)

Future microprocessor poses many challenges to its dedicated power supplies, the voltage regulators (VRs), such as the low voltage, high current, fast load transient, etc. For the VR designs using multiphase buck converters, one of the results from these stringent challenges is a large amount of output capacitors, which is undesired from both a cost and a motherboard real estate perspective. In order to save the output capacitors, the control-loop bandwidth must be increased. However, the bandwidth is limited in the practical design. The influence from the switching frequency on the control-loop bandwidth has not been identified, and the influence from multiphase is not clear, either. Since the widely-used average model eliminates the inherent switching functions, it is not able to predict the converter's high-frequency performance. In this dissertation, the primary objectives are to develop the methodology of high-frequency modeling for the buck and multiphase buck converters, and to analyze their high-frequency characteristics.

First, the nonlinearity of the pulse-width modulator (PWM) scheme is identified. Because of the sampling characteristic, the sideband components are generated at the output of the PWM comparator. Using the assumption that the sideband components are well attenuated by the low-pass filters in the converter, the conventional average model only includes the perturbation-frequency components. When studying the high-frequency performance, the sideband frequency is not sufficiently high as compared with the perturbation one; therefore, the assumption for the average model is not good any more. Under this condition, the converter response cannot be reflected by the average model. Furthermore, with a closed loop, the generated sideband components at the output voltage appear at the input of the PWM comparator, and then generate the perturbation-frequency components at the output. This causes the sideband effect to happen. The perturbation-

frequency components and the sideband components are then coupled through the comparator. To be able to predict the converter's high-frequency performance, it is necessary to have a model that reflects the sampling characteristic of the PWM comparator. As the basis of further research, the existing high-frequency modeling approaches are reviewed. Among them, the harmonic balance approach predicts the high-frequency performance but it is too complicated to utilize. However, it is promising when simplified in the applications with buck and multiphase buck converters. Once the nonlinearity of the PWM comparator is identified, a simple model can be obtained because the rest of the converter system is a linear function.

With the Fourier analysis, the relationship between the perturbation-frequency components and the sideband components are derived for the trailing-edge PWM comparator. The concept of multi-frequency modeling is developed based on a single-phase voltage-mode-controlled buck converter. The system stability and transient performance depend on the loop gain that is affected by the sideband component. Based on the multi-frequency model, it is mathematically indicated that the result from the sideband effect is the reduction of magnitude and phase characteristics of the loop gain. With a higher bandwidth, there are more magnitude and phase reductions, which, therefore, cause the sideband effect to pose limitations when pushing the bandwidth.

The proposed model is then applied to the multiphase buck converter. For voltage-mode control, the multiphase technique has the potential to cancel the sideband effect around the switching frequency. Therefore, theoretically the control-loop bandwidth can be pushed higher than the single-phase design. However, in practical designs, there is still magnitude and phase reductions around the switching frequency in the measured loop gain. Using the multi-frequency model, it is clearly pointed out that the sideband effect cannot be fully cancelled with unsymmetrical phases, which results in additional reduction of the phase margin, especially for the high-bandwidth design. Therefore, one should be extremely careful to push the bandwidth when depending on the interleaving to cancel the sideband effect.

The multiphase buck converter with peak-current control is also investigated. Because of the current loop in each individual phase, there is the sideband effect that

cannot be canceled with the interleaving technique. For higher bandwidths and better transient performances, two schemes are presented to reduce the influence from the current loop: the external ramps are inserted in the modulators, and the inductor currents are coupled, either through feedback control or by the coupled-inductor structure. A bandwidth around one-third of the switching frequency is achieved with the coupled-inductor buck converter, which makes it a promising circuit for the VR applications.

As a conclusion, the feedback loop results in the sideband effect, which limits the bandwidth and is not included in the average model. With the proposed multi-frequency model, the high-frequency performance for the buck and multiphase buck converters can be accurately predicted.

TO MY PARENTS

FEIZHOU QIU AND CUIZHEN LIU

AND TO MY WIFE

JUANJUAN SUN

Acknowledgments

I would like to express my sincere appreciation to my advisor, Dr. Fred C. Lee, for his continued guidance, encouragement and support. It is an honor to be one of his students here at the Center for Power Electronics Systems (CPES), one of the best research centers in power electronics. In the past years, I am always amused by his great intuition, broad knowledge and accurate judgment. The most precious things I learned from him are the ability of independent research and the attitude toward research, which can be applied to every aspects of life and will benefit me for the rest of my life.

I would also like to thank Dr. Ming Xu for his enthusiastic help during my research at CPES. His selfless friendship and leadership helped to make my time at CPES enjoyable and rewarding. From him, I learned so much not only in the knowledge of power electronics but also in the research methodologies. His valuable suggestions helped to encourage my pursuing this degree.

I am grateful to the other members of my advisory committee, Dr. Daan van Wyk, Dr. Yilu Liu, Dr. Guo-Quan Lu, and Dr. Dan Y. Chen for their support, comments, suggestions and encouragement.

I am especially indebted to my colleagues in the VRM group and the ARL group. It has been a great pleasure to work with the talented, creative, helpful and dedicated colleagues. I would like to thank all the members of my teams: Dr. Peng Xu, Dr. Pit-Leong Wong, Dr. Kaiwei Yao, Dr. Wei Dong, Dr. Francisco Canales, Dr. Bo Yang, Dr. Jia Wei, Mr. Mao Ye, Dr. Jinghai Zhou, Dr. Yuancheng Ren, Mr. Bing Lu, Mr. Yu Meng, Mr. Ching-Shan Leu, Mr. Doug Sterk, Mr. Kisun Lee, Mr. Julu Sun, Dr. Shuo Wang, Dr. Xu Yang, Mr. Yonghan Kang, Mr. Chuanyun Wang, Mr. Dianbo Fu, Mr. Arthur Ball, Mr. Andrew Schmit, Mr. David Reusch, Mr. Yan Dong, Mr. Jian Li, Mr. Bin Huang, Mr. Ya Liu, Mr. Yucheng Ying, and Mr. Yi Sun. It was a real honor working with you guys.

I would like to thank my fellow students and visiting scholars for their help and guidance: Dr. Peter Barbosa, Mr. Dengming Peng, Dr. Jinjun Liu, Dr. Jae-Young Choi, Dr. Qun Zhao, Dr. Zhou Chen, Dr. Jinghong Guo, Dr. Linyin Zhao, Dr. Rengang Chen, Dr.

Zhenxue Xu, Dr. Bin Zhang, Dr. Xigen Zhou, Ms. Qian Liu, Mr. Xiangfei Ma, Mr. Wei Shen, Dr. Haifei Deng, Ms. Yan Jiang, Ms. Huiyu Zhu, Mr. Pengju Kong. Mr. Jian Yin, Mr. Wenduo Liu, Dr. Zhiye Zhang, Ms. Ning Zhu, Ms. Jing Xu, Ms. Yan Liang, Ms. Michele Lim, Mr. Chucheng Xiao, Mr. Hongfang Wang, Mr. Honggang Sheng, and Mr. Rixin Lai.

I would also like to thank the wonderful members of the CPES staff who were always willing to help me out, Ms. Teresa Shaw, Ms. Linda Gallagher, Ms. Teresa Rose, Ms. Ann Craig, Ms. Marianne Hawthorne, Ms. Elizabeth Tranter, Ms. Michelle Czamanske, Ms. Linda Long, Mr. Steve Chen, Mr. Robert Martin, Mr. Jamie Evans, Mr. Dan Huff, Mr. Callaway Cass, Mr. Gary Kerr, and Mr. David Fuller.

My heartfelt appreciation goes toward my parents, Feizhou Qiu and Cuizhen Liu, who have always provided support and encouragement throughout my further education.

Finally, with deepest love, I would like to thank my wife, Juanjuan Sun, who has always been there with her love, support, understanding and encouragement for all of my endeavors.

This work was supported by the VRM consortium (Artesyn, Delta Electronics, Hipro Electronics, Infineon, Intel, International Rectifier, Intersil, Linear Technology, National Semiconductor, Renesas, and Texas Instruments), and the Engineering Research Center Shared Facilities supported by the National Science Foundation under NSF Award Number EEC-9731677. Any opinions, findings and conclusions or recommendations expressed in this material are those of the author and do not necessarily reflect those of the National Science Foundation.

This work was conducted with the use of SIMPLIS software, donated in kind by Transim Technology of the CPES Industrial Consortium.

Table of Contents

List of Tables

List of Figures

Chapter 1. Introduction

1.1 Background: Voltage Regulators

In the past four decades, the Moore's law, which states "transistor density … doubles every eighteen months", has successfully predicted the evolution of microprocessors, as shown in Figure 1.1 [1]. Currently, the latest processors from Intel consist of hundreds of millions of transistors [2]. It is predicted that in 2015, there will be tens of billions of transistors in a single chip [3].

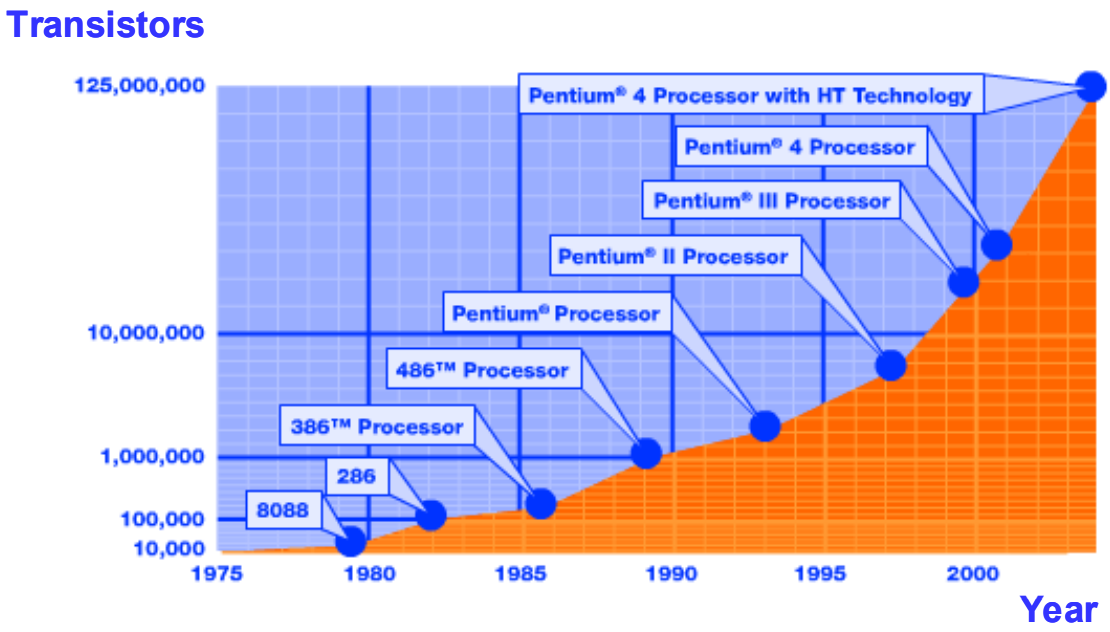

Figure 1.1. Intel's roadmap of number of integrated transistors in one microprocessor.

More integrated transistors leads to better computing performance. As shown in Figure 1.2 [4], the computing speed, as measured in millions of instructions per second (MIPS), increases dramatically in the past four decades. It is predicted that in around 2015, the microprocessor can deal with 10 trillion instructions per second [4].

However, the more transistors packed into smaller spaces, and the higher computing performances, the more power the microprocessors consume. Currently, a three-percent increase in power consumption is required for a one-percent improvement in

microprocessor performance [3]. Since all the electric power consumed by the microprocessor is transferred to heat eventually, stringent challenges have been posed on the thermal management. There is the prevision that if the development of the processors still follows Moor's law but without improvements of the power management, a power loss density of tens of thousands watts per square centimeter is possible [3].

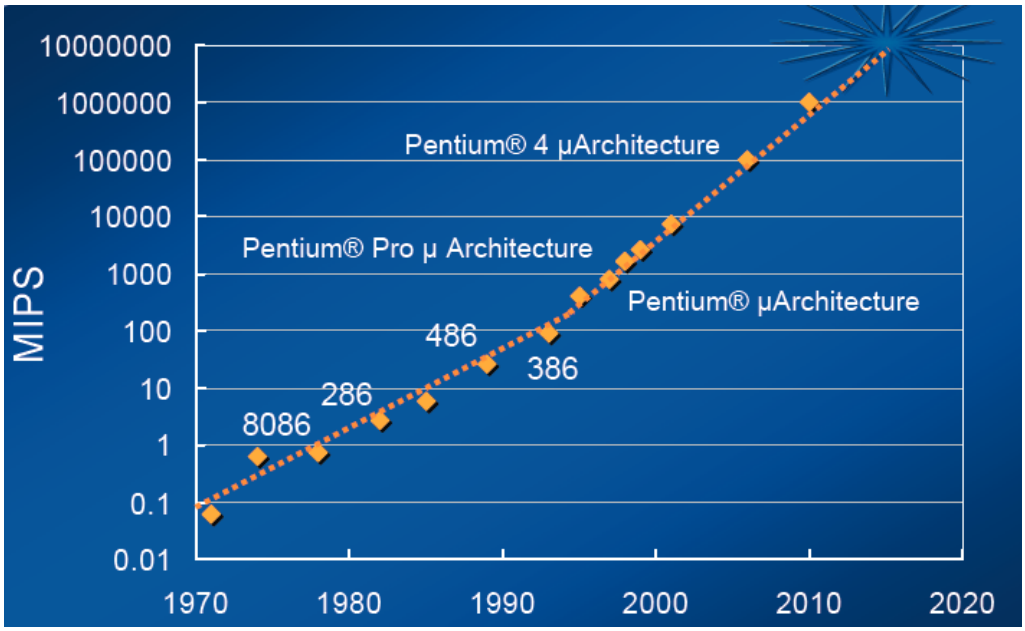

Figure 1.2. Intel's roadmap of computing performance for the microprocessors.

New power management technologies for the transistors in the microprocessor have been introduced in the past decade. One of the solutions is to decrease the microprocessor supply voltage. Starting with the Intel Pentium processor, microprocessors began to use a non-standard power supply of less than 5 V, and the supply voltages have been and will continuously be decreased. On the other hand, the increasing number of transistors in the microprocessors results in continuous increase of the microprocessor current demands, as shown in Figure 1.3 [5][6]. Although new technologies, such as the multi-core structure for the microprocessors, may slow down the trend, it is expected that the challenges to the power supply is still stringent [6]. Moreover, due to the high computing speed, the microprocessors' load transition speeds also increase. In the mean time, the voltage deviation window during the transient is becoming smaller and smaller, since the output

voltage keeps decreasing. The low voltage, high current, fast load transition speed, and tight voltage regulation impose challenges on the power supplies of the microprocessors.

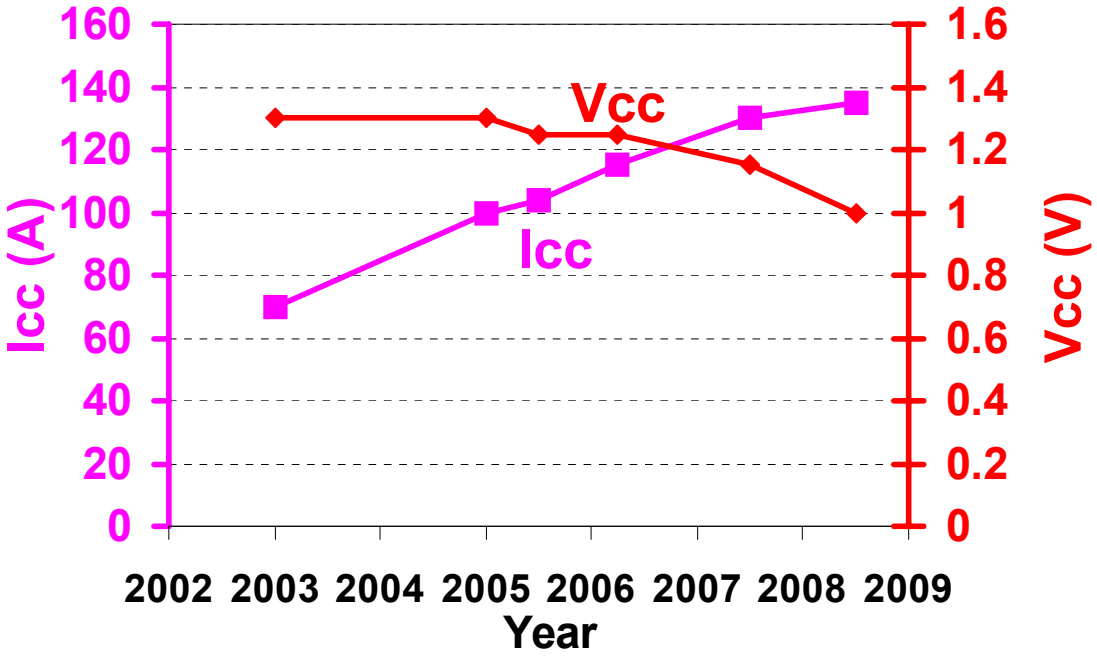

Figure 1.3. The roadmap of microprocessor supply voltage and current.

When using the 5-V legacy voltage level, the microprocessor was powered by a centralized silver box. Because the parasitic resistors and inductors of the connections between it and the microprocessors have a severe negative impact on the power quality, it is no longer practical for the bulky silver box to provide energy directly to the microprocessor for the low-voltage high-current applications. Therefore, the voltage regulator (VR) is introduced as the dedicated power supply.

For the low-end microprocessor VR, a single conventional buck or synchronous buck topology, as shown in Figure 1.4, is utilized for power conversion [7][8][9]. As the microprocessor power consumption increases continuously, it is impossible to use a single device as the top or bottom switches in the buck converter. To handle the required high current, more devices in parallel are necessary.

Meanwhile, the earlier VRs operated at low switching frequencies with high filter inductances. However, the large output-filter inductance limits the energy transfer speed.

In order to meet the microprocessor requirements, huge output-filter capacitors and decoupling capacitors are needed to reduce the voltage spike during the load transient.

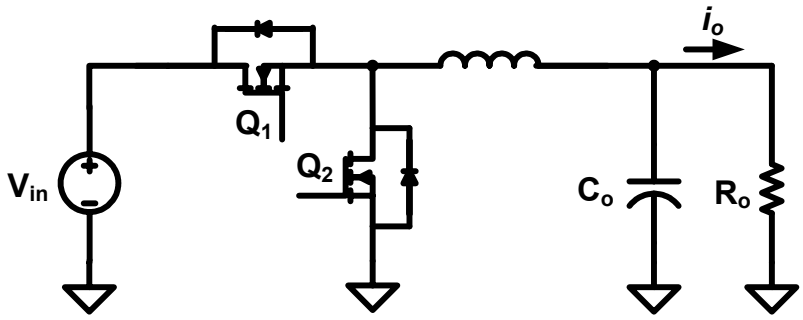

Figure 1.4. A single-phase synchronous buck converter.

In order to reduce the VR output capacitance to save the total cost and to increase the power density, high inductor current slew rates are preferred. With smaller inductances, larger inductor current slew rates are obtained; therefore, a smaller output capacitance can be used to meet the transient requirements. In order to greatly increase the transient inductor current slew rate, the inductances need to be reduced significantly, as compared with those in conventional designs.

On the other hand, small inductances result in large current ripples in the circuit's operation at the steady state. The large current ripple usually causes a large turn-off loss. In addition, it generates large steady-state voltage ripples at the VR output capacitors. The steady-state output voltage ripples can be so large that they are comparable to transient voltage spikes. It is impractical for the converter to work this way.

To solve the aforementioned issues, VPEC/CPES proposes to parallel phases instead of devices, as shown in Figure 1.5 [10][11][12][13][1]. It consists of n identical converters with interconnected inputs and outputs. Based on this structure, the interleaving technology is introduced by phase shifting the duty cycles of adjacent channels with a degree of $360^o/n$. With the proposed multiphase buck converter, the output current ripples are greatly decreased, as shown in Figure 1.6. Therefore, the steady-state output voltage ripples are significantly reduced, making it possible to use very small inductances in VRs to improve the transient responses.

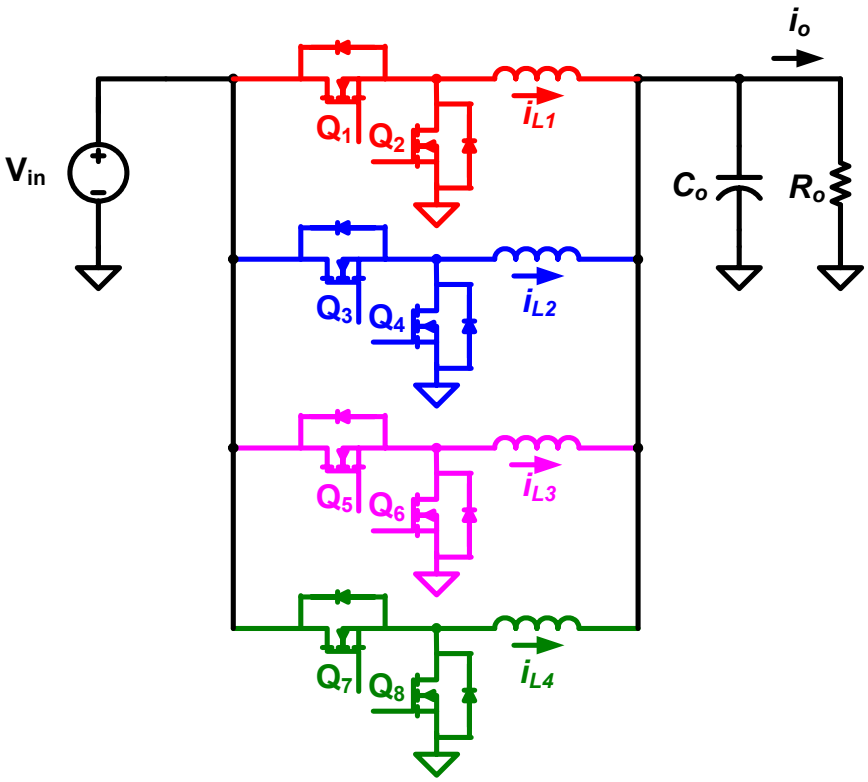

Figure 1.5. A multiphase buck converter.

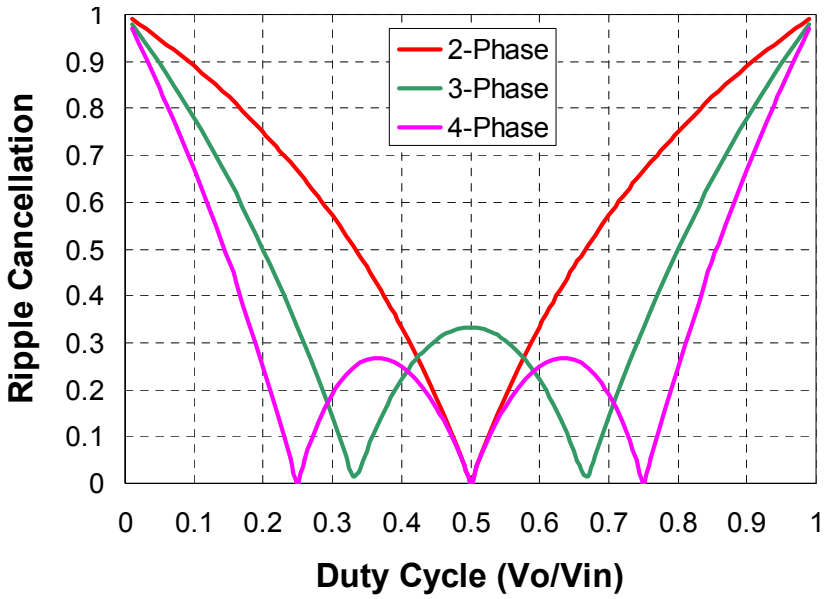

Figure 1.6. Current ripple cancellations in multiphase VRs.

Besides the benefits of smaller steady-state voltage ripples and transient voltage spikes, the multiphase buck converter makes the thermal dissipation more evenly distributed. Studies also show that in high-current applications, the overall cost of the converter can be reduced using this technology. Therefore, many semiconductor companies, such as Intersil, National Semiconductor, Texas Instruments, Analog Devices, On Semiconductor, and Volterra, have produced dedicated control ICs for multiphase VRs. The concept of applying interleaving to VRs is so successful that it has become an industry standard practice in the VR applications.

1.2 Challenges to VR High-Frequency Modeling

As the microprocessors develops, the power management related issues become much more critical for future microprocessors and much more difficult to deal with. If today's low-frequency solution is still employed to meet the future transient requirement, more capacitors have to be paralleled. Based on the microprocessor power delivery path [14] and the specifications, it can be calculated [15][16] that the bulk capacitor number will increase by 40%, and the decoupling capacitor number will double, as shown in Figure 1.7. As the result, the cost of capacitors will increase 60%. Therefore, how to meet the requirement of fast transient response with fewer output capacitors becomes one of the most challenging issues to the VR designers.

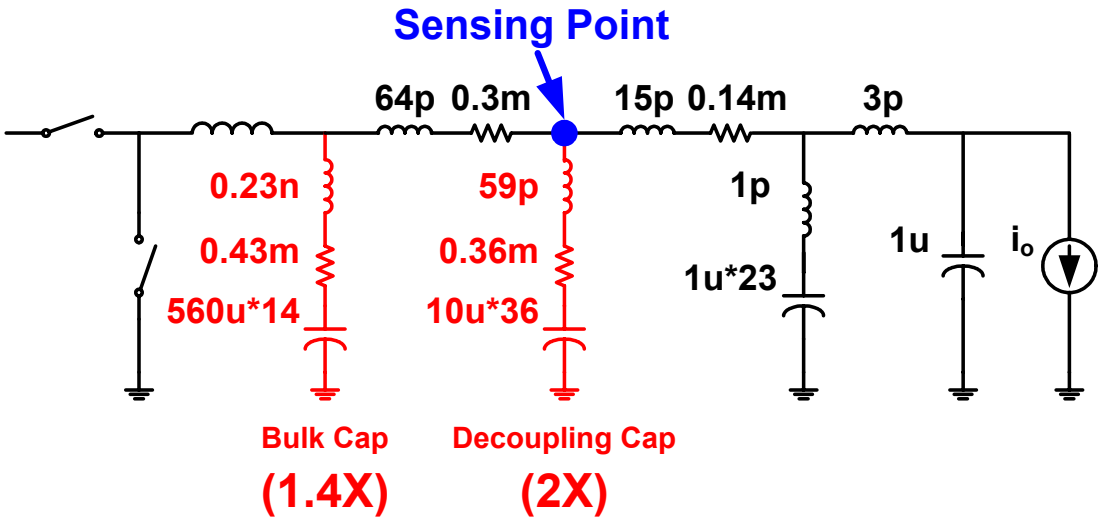

Figure 1.7. Future microprocessor demands more capacitors if today's solution is still followed.

To reduce the output capacitors, several nonlinear methods have been proposed [17][18]. Approaches using hybrid filters have also been introduced [19][20]. However, these methods are not yet ready for the practical VR applications. From the standpoint of an industry product, the linear control method is preferred [8][21].

For the buck VRs with linear control methods, it has been shown that there are two fundamental limitations to the inductor current slew rate [15][16][22][23][24][25]. Assuming constant input and output voltages, the inductance value determines the slew rate when the duty cycle is saturated. Without the duty-cycle saturation, the feedback control loop's bandwidth determines the slew rate. With a higher bandwidth, a faster inductor current slew rate is achievable. Consequently, fewer output capacitors are needed for the desired transient performance, as shown in Figure 1.8 [15][16]. Therefore, to reduce the output capacitance, high-bandwidth designs are mandatory.

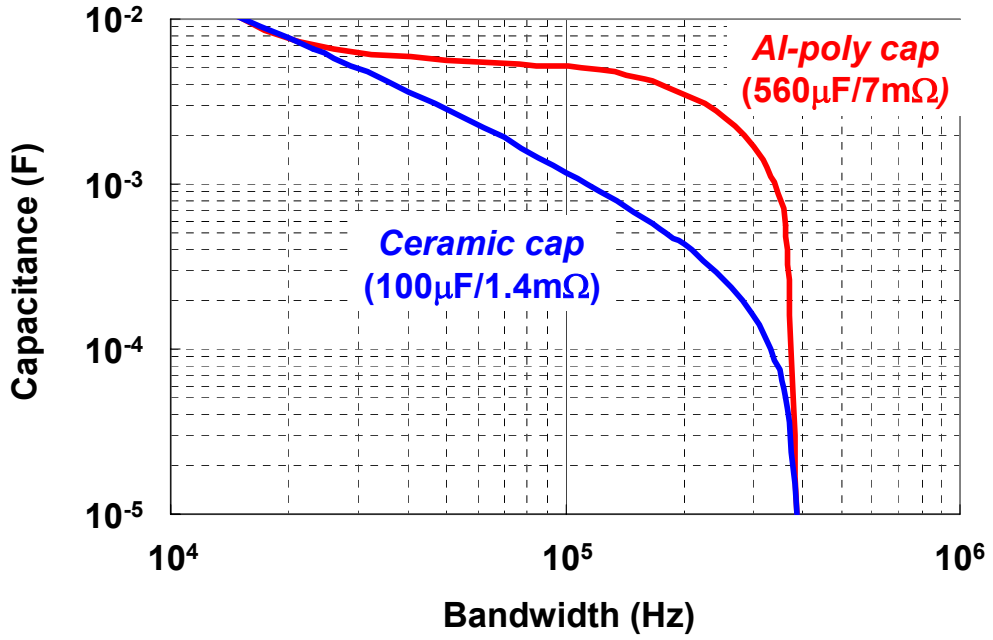

Figure 1.8. The relationship between VR's bandwidth and the output bulk capacitance for future microprocessors based on today's power delivery path.

In today's practice of multiphase buck VRs, the bandwidth can only be pushed to around 1/10~1/6 of the switching frequency. Higher switching frequencies are required for higher bandwidths. For example, to eliminate the bulk capacitors, a 390-kHz bandwidth is

necessary. Assuming the bandwidth of one-sixth switching frequency is achievable, a switching frequency higher than 2.3 MHz is required.

However, higher switching frequency means more switching-related losses and lower efficiency. As an example, Figure 1.9 compares the efficiency for a 4-phase synchronous buck VR running at 300-kHz and 1-MHz switching frequencies. This 12-V input, 0.8-V 70-A output VR uses one HAT2168 as the top switch and two HAT2165 as the bottom switch for each phase. From 300 kHz to 1 MHz, the efficiency degrades around 5% [16].

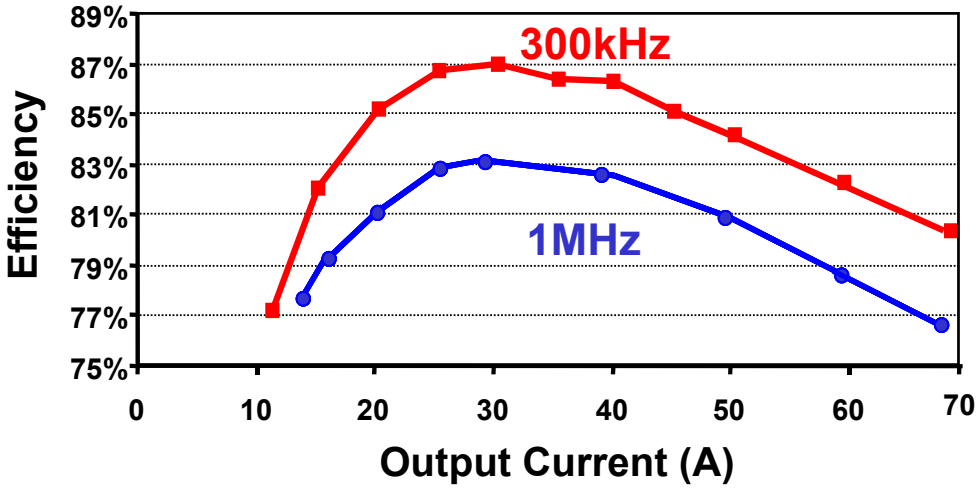

Figure 1.9. VRs' efficiency suffers a lot as the switching frequency increases.

Because of the efficiency consideration, it is expected that the bandwidth can be pushed as high as possible with a certain switching frequency. Therefore, it is necessary to investigate the bandwidth limitations for the buck and multiphase buck converters.

To study the issues of pushing the bandwidth, the switching-model simulation results from SIMPLIS software are analyzed. Figure 1.10 compares the loop gains, T_v, with different bandwidths for a 1-MHz single-phase voltage-mode-controlled buck converter, as in Figure 1.11. With same poles and zeroes but different DC gain in the compensator, there is more phase delay when the bandwidth is pushed from 100 kHz to 400 kHz. At 400 kHz, the phase delay is 145^o for the 400-kHz-bandwidth design, while it is 126^o for the 100-kHz-bandwidth case. Therefore, a higher bandwidth results in additional phase delays in the loop gain. Besides, with a 3-pole 2-zero compensator, the phase delay is 270^o at the

switching frequency. Therefore, there exists a limitation for the control loop bandwidth, which is related to the switching frequency.

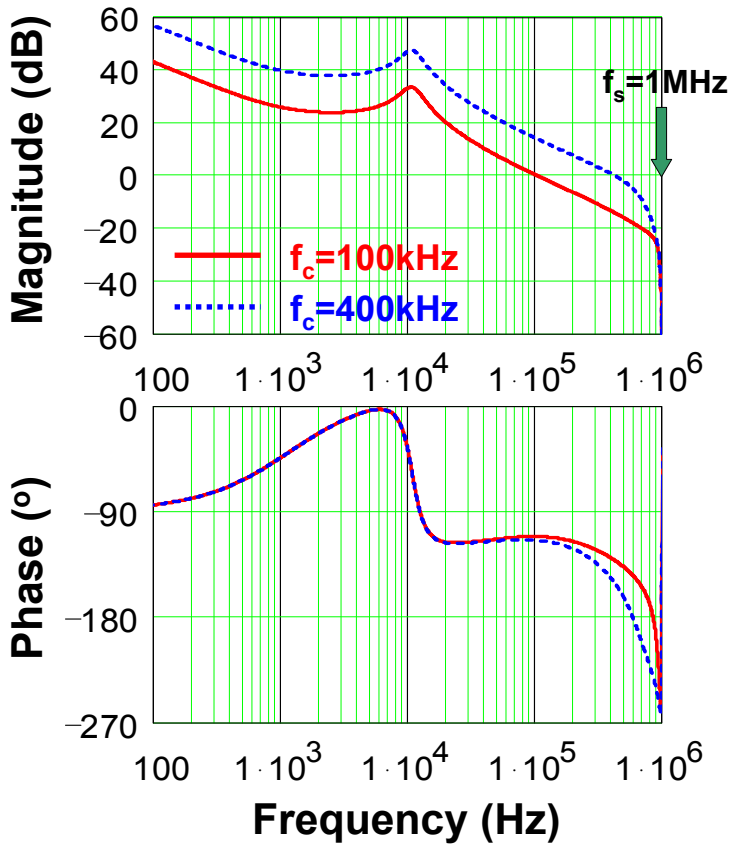

Figure 1.10. Simulated loop gains of a 1-MHz buck converter with voltage-mode control. (Red solid line: 100-kHz-bandwidth design; Blue dotted line: 400-kHz-bandwidth design.)

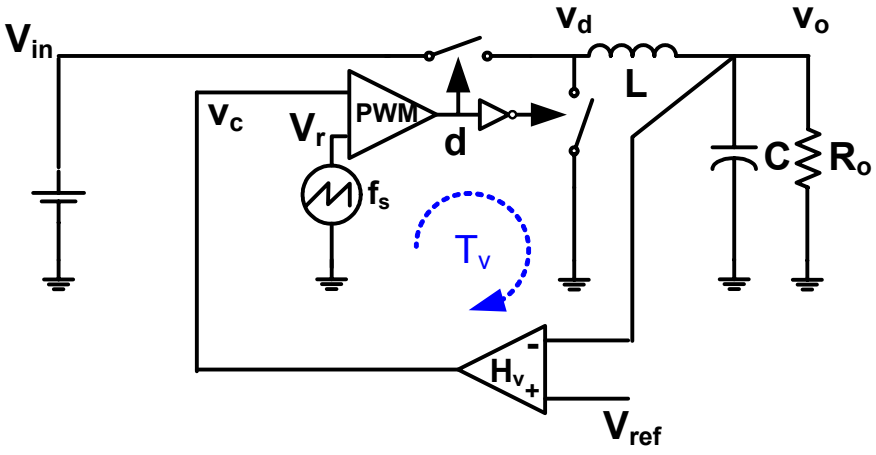

Figure 1.11. A single-phase voltage-mode-controlled buck converter.

In the past, most of the feedback controller designs have been based on the average model [26][27] for buck converters. The multiphase buck has also been simplified to single-phase buck converters in the average model [23]. However, according to the observations above, the switching frequency plays an important role in the loop gain at the high-frequency region. The highest achievable bandwidth is related to the switching frequency. Because the state-space averaging process eliminates the inherent sampling nature of the switching converter, the accuracy of the average model is questionable at frequencies approaching half of the switching frequency [28].

As an example, for the 1-MHz single-phase buck converter with voltage-mode control, Figure 1.12 compares the loop gain calculated from the average model with that obtained in the switching-model simulation using SIMPLIS. For the case with a 100-kHz bandwidth of the voltage loop, the average model agrees with the simulation up to around half of the switching frequency.

However, for the 400-kHz bandwidth design, the average model is only good up to 100 kHz, i.e., one-tenth of the switching frequency. The simulation result has a 25^{o} more phase delay at the crossover frequency as compared with the average model. This excessive phase drop would result in undesired transient or stability problems if a high-bandwidth converter is designed based on the average model, which cannot predict the high-frequency behaviors.

For a better understanding of the characteristics of the control loop, the fundamental relationship between the control-loop bandwidth and the switching frequency should be clarified. To obtain an analytical insight, a simple model including the switching frequency information is desired. To address these issues, the primary objective of this dissertation is to investigate the influence from the switching frequency on the converter performances. The methodology of high-frequency modeling for the buck and multiphase buck converters is developed and utilized to analyze their high-frequency characteristics.

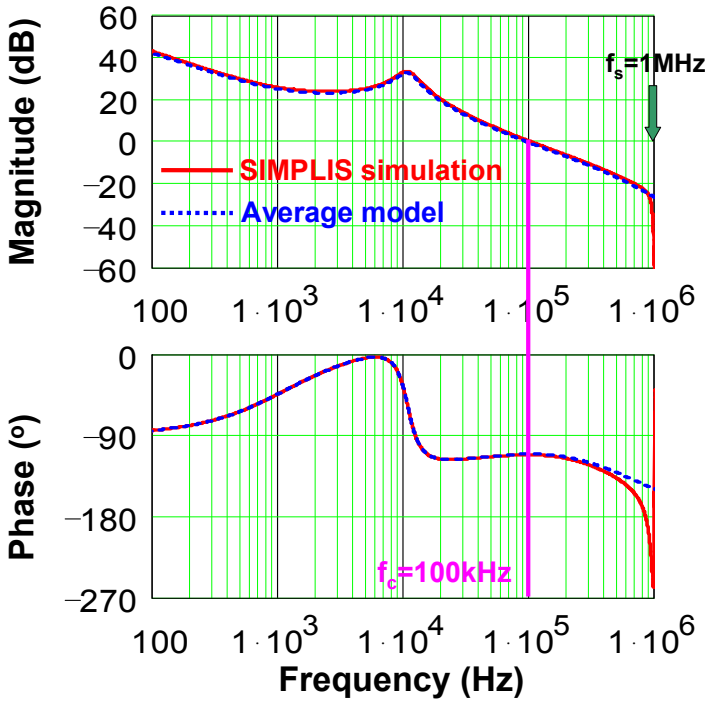

(a) The 100-kHz bandwidth design.

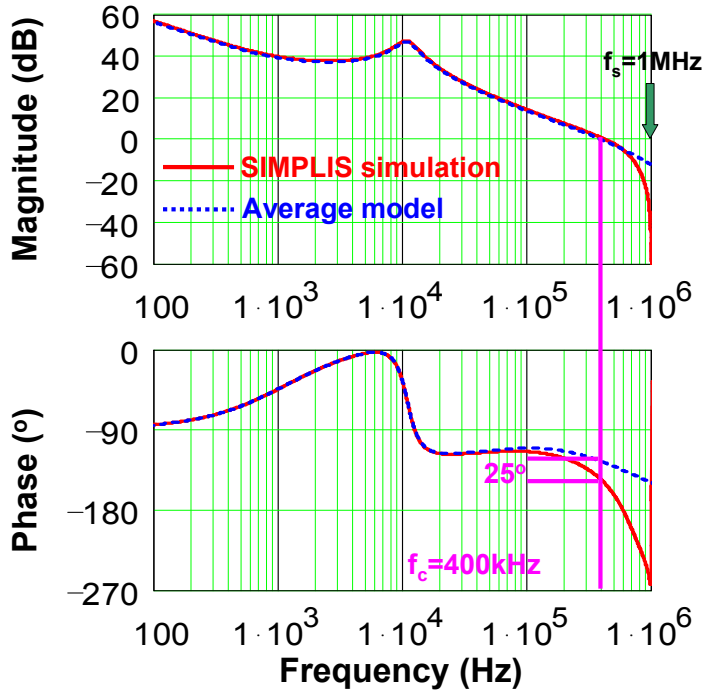

(b) The 400-kHz bandwidth design.

Figure 1.12. Comparison of loop gains between SIMPLIS simulation and average model for a 1-MHz buck converter with voltage-mode control.

(Red solid line: SIMPLIS simulation result; Blue dotted line: average-model result.)

1.3 Dissertation Outlines

This dissertation consists of six chapters. They are organized as follows. First, the background information of VRs and the needs for VR high-frequency modeling are introduced. Then, the characteristics of the pulse-width modular (PWM) converters are reviewed. The sideband effect as a result of feedback control is identified. After that, based on the harmonic balance approach, the concept of multi-frequency modeling is developed to address the sideband effect for a single-phase voltage-mode-controlled buck converter. Next, following the same approach, this model is applied to the multiphase buck converter. At last, the influence from the current feedback loop is investigated. Several methods to achieve high-bandwidth designs for VR applications are explored.

The detailed outline is elaborated as follows.

Chapter 1 is the background review of existing VR technologies and the need for high-frequency VR modeling. Multiphase buck converters have become the standard practice for VRs in the industry. In order to improve the transient response, the control-loop bandwidth must be increased. However, the bandwidth is limited in the practical design. The relationship between the switching frequency and the control-loop bandwidth is not clear. Since the conventional average model eliminates the inherent switching functions, it is not able to predict the high-frequency performance. The primary objectives of this dissertation are to develop the methodology of high-frequency modeling for the buck and multiphase buck converters, and to analyze their high-frequency characteristics.

Chapter 2 discusses the nonlinearity of the PWM scheme and reviews the existing approaches to model this nonlinearity. Because of the inherent sampling function of the PWM comparator, sideband-frequency components are generated in the converter. With a feedback control loop, the sideband component appears at the input of the comparator and generates the perturbation-frequency component again. Through the comparator, the sideband components and the perturbation-frequency components are coupled. With the assumption of low-pass filters in the converter, the conventional average model only includes the perturbation frequency and regards the PWM comparator as a simple gain. Therefore, it does not reflect these phenomena. To be able to predict the converter's high-frequency performance, it is necessary to have a model that reflects the sampling

characteristic of the PWM comparator. As the basis of further research, the existing high-frequency modeling approaches are reviewed. The harmonic balance approach is able to predict the high-frequency performance but it is complicated to utilize. However, for the applications with buck and multiphase buck converters, once the nonlinearity of the PWM comparator is identified, a simplified model can be obtained.

Chapter 3 introduces the multi-frequency model to predict the system behavior. With the Fourier analysis, the relationship between the sideband components and the perturbation-frequency components are derived for the PWM comparator. The concept of multi-frequency modeling is developed based on a single-phase voltage-mode-controlled buck converter. The influences of the sideband effect are investigated quantitatively.

In Chapter 4, the proposed model is applied to the multiphase buck converter. For voltage-mode control, the multiphase technique has the potential to cancel the sideband effect around the switching frequency. Therefore, it is theoretically possible to push the control-loop bandwidth higher than the designs with single-phase buck converter. However, the asymmetry among phases results in design risks to push the control-loop bandwidth in implementations. Considering the inductors with practical tolerances as an example, the limitation of bandwidth is discussed.

Chapter 5 analyzes the multiphase buck converters with peak-current control. In the current loop of each phase, there is a sideband effect that cannot be canceled with the interleaving technique. For higher bandwidth and better transient performances, two schemes are presented to reduce the influence from the current loop: the external ramps are inserted to the modulators, and the inductor currents are coupled, either through feedback control or by the coupled-inductor structure. The sample-data model for the coupled-inductor buck converter is derived, which explains the benefit of strong coupling on bandwidth improvements.

Chapter 6 is the summary of this dissertation.

Chapter 2. Characteristics of PWM Converters

2.1 Introduction

As predicted by Moore's law, future computer microprocessors will consist of billions of integrated transistors. To reduce the power consumption, the operating voltages will continue to drop. The allowed variation of the output voltage will become smaller for the VRs. On the other hand, the higher speed of future processors leads to more dynamic load. Consequently, one special issue existing for the VRs is how to meet the stringent voltage regulation requirements with less output capacitors. This is a strict challenge because of cost related considerations, as well as limited space for VRs in the computer system.

To save the output capacitors, the VR inductor current slew rate must be increased. It has been studied that with linear control methods, the feedback loop's bandwidth plays a very important role in the transient response [15][16][22][23][24][25]. With a higher bandwidth, fewer output capacitors are needed to meet the required transient performance specifications. On the other hand, high-bandwidth designs normally require high switching frequency, which is not preferred from an efficiency aspect because of the frequency-related losses. Pushing the control-loop bandwidth without increasing the switching frequency is more desirable.

The relationship between the control-loop bandwidth and the switching frequency is not clear. Conventionally, the control designs of the multiphase buck VRs utilize the average model, which does not include the switching information. About the voltage loop gain of a single-phase buck converter shown in Figure 1.12, the average model fails to predict the performance around or beyond half of the switching frequency, especially with high-bandwidth designs. To explain the discrepancies between the average model and switching-model simulation, and to clarify the limitations of the control-loop bandwidth, a model that can reflect the inherent switching characteristics of the converter is essential for further studies. Once the model is obtained, it is possible to achieve guidelines for the control designs and high-bandwidth solutions.

To clearly understand the switching feature of the converter, this chapter investigates the nonlinear characteristics of the pulse-width modulator (PWM). First, the existences of sideband components are observed as a result of sampling. After that, the influence from the feedback loop is analyzed based on a single-phase voltage-mode-controlled buck converter. The sideband effect is identified, i.e. the sideband component appears at the input of the comparator and generates the perturbation-frequency component again. Then, the transfer function measurement and simulation are discussed, especially on how they deal with the sideband effect. As the basis of further research, the existing high-frequency modeling approaches are reviewed.

2.2 Characteristics of the Pulse-Width Modulator

Before a way can be found to identify the limitation of the average model and to predict the converter's high-frequency performance, it is essential to clarify the characteristics of the PWM converter.

As an example, Figure 2.1 illustrates the structure when studying the response of an open-loop single-phase buck converter with a perturbation at the control voltage, V_c. For the small-signal analysis, it is assumed that the perturbation is small enough that it does not change the operating point of the converter. When studying the performance at a certain frequency, the perturbation is assumed to be sinusoidal for simplicity.

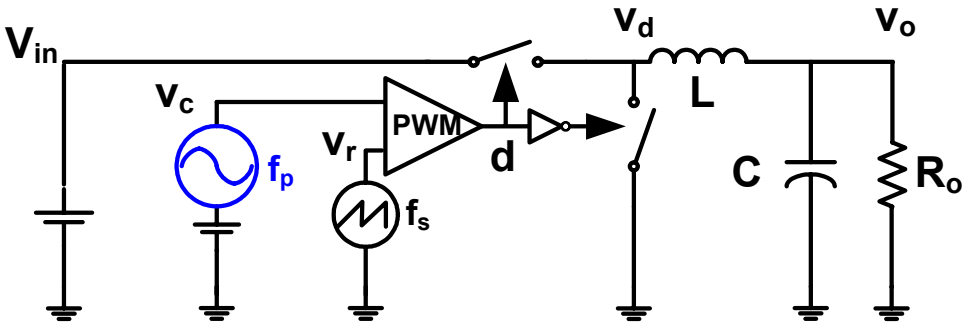

Figure 2.1. An open-loop single-phase buck converter with V_c perturbation.

For the trailing-edge PWM comparator as shown in Figure 2.2, with a sinusoidal perturbation frequency at f_p, the spectra of the comparator input, V_c, and that of the output,

d, are illustrated in Figure 2.3 [29][30][31][32][33]. Because they are periodical in the time domain, these signals have discrete spectra in the frequency domain.

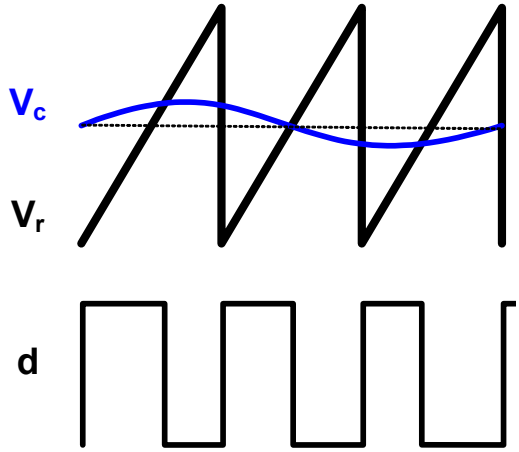

Figure 2.2. Inputs and output of the trailing-edge PWM comparator with V_c perturbation.

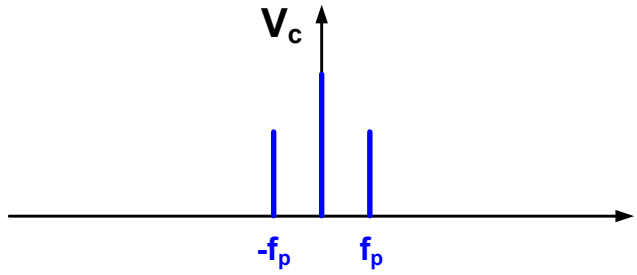

(a) Input spectrum of the PWM comparator.

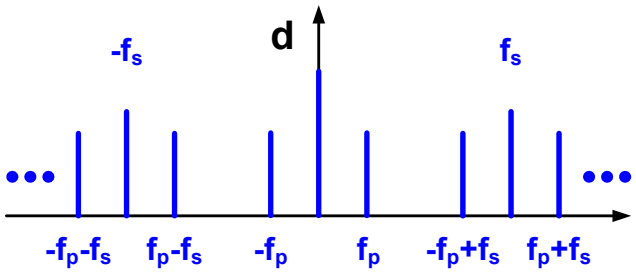

(b) Output spectrum of the PWM comparator.

Figure 2.3. Sampling result of the PWM scheme.

Clearly, the spectrum of *d* consists of the DC component, the components at the switching frequency, f_s, and its harmonic frequencies. The components at the perturbation frequency, f_p and $-f_p$, appear at the comparator output as well. Meanwhile, because the

PWM comparator works like a sample-data function, its output, d, has infinite frequency components at f_p-f_s, -f_p+f_s, f_p+f_s, -f_p-f_s, etc [29][30][31][32][33]. These frequencies are called the sideband frequencies or the beat frequencies around f_s, -f_s, etc., which do not exist at the input of the comparator. Hence, the PWM comparator is a typical nonlinear function.

For the PWM comparator, there are special cases existing when $f_p=kf_s/2$, k=1, 2, 3, … As an example, Figure 2.4 illustrates the case when the perturbation frequency is exactly at half of the switching frequency. Under this condition, the aliasing effect happens [30][31][34], which means the sideband frequency overlaps with the perturbation frequency itself, namely f_p is equal to f_s-f_p. Therefore, besides the DC and switching frequency components, the system contains components at f_p, -f_p, f_p+f_s, -f_p-f_s, etc. For example, when $f_p=f_s/2$, there is only one frequency component below the switching frequency besides DC, which is different from the perturbation at other frequencies. From this aspect, again, the PWM comparator is a nonlinear function.

In this chapter, only the perturbation at V_c is considered, as in Figure 2.1. The input voltage, V_{in}, is assumed constant. Under this condition, the buck converter's phase voltage, V_d, has a similar waveform as d, except its magnitude is V_{in} times high, as shown in Figure 2.5. Whether there is an aliasing effect or not, for the spectra in Figure 2.6, V_d has the same number of frequency components as that of d and there is no additional frequencies generated. The only difference is that the magnitudes of V_d's frequency components are V_{in} times as high as those of d. Therefore, with the constant input voltage assumption, the function of the two switches in the buck converter is to magnify the duty cycle signal, d, to be the phase voltage, V_d, which is a typical linear function.

Meanwhile, the output filter topology of buck converters does not change during the switch on-time and off-time, so it is also a linear function. Thus, all the components at V_d appear at the output voltage, V_o, through the low-pass filter formed by the output inductor and capacitor. In summary, the PWM comparator is the only nonlinearity for the open-loop buck converter with perturbations on the control voltage.

When analyzing the small-signal stability and the transient performance of a converter, it is not necessary to include the components at DC, the switching frequency,

and its harmonics. Only the consequence of the perturbation, i.e. the components at the perturbation frequency and the sideband frequencies, needs to be included in the models.

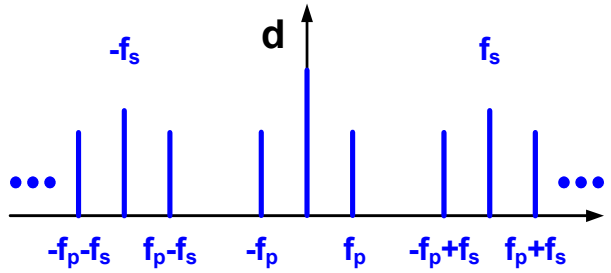

(a) $f_p<f_s/2$.

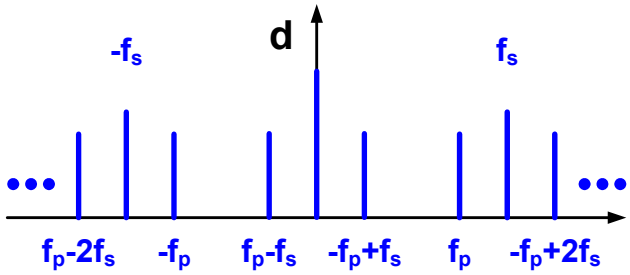

(b) $f_s/2<f_p<f_s$.

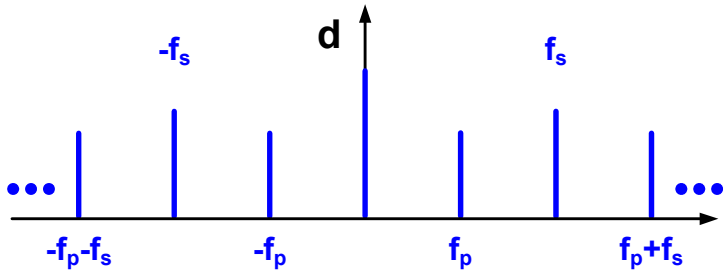

(c) $f_p=f_s/2$.

Figure 2.4. Aliasing effect happens at half of the switching frequency.

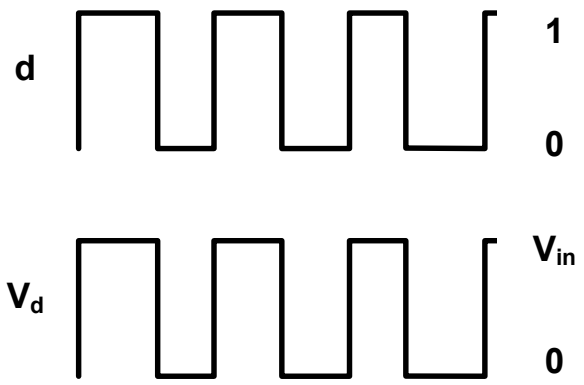

Figure 2.5. Input and output waveforms of the switches in buck converter with constant input voltage.

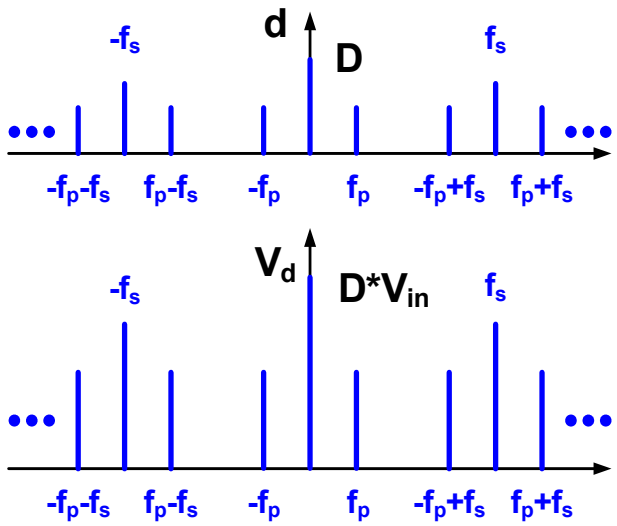

Figure 2.6. Input and output spectra of the switches in buck converter with constant input voltage.

In the conventional average model, the describing function of the PWM comparator only include the perturbation-frequency components, assuming the other frequency can be well attenuated by the low-pass filters in the converter. It is questionable whether this assumption is still valid for the high-frequency performance study. Therefore, it is essential to understand the influence from the sideband frequencies on the system with multiple frequencies.

First, the phenomena at a more general case of $f_p \neq kf_s/2$, k=1, 2, 3, …, is observed and discussed.

As an example, a 1-MHz single-phase buck converter is studied with the setup as shown in Figure 2.1. For this converter, V_{in} is 12 V, V_o is 1.2 V, L is 200 nH, C is 1 mF, R_o is 80 mΩ, the peak-to-peak value of the sawtooth ramp, V_r, is 1 V. The sinusoidal perturbation at the control voltage has the magnitude of 5 mV. With these parameters, the response of the output voltage is monitored with certain perturbation frequencies. Two cases with perturbation frequency at 10 kHz and 990 kHz are simulated.

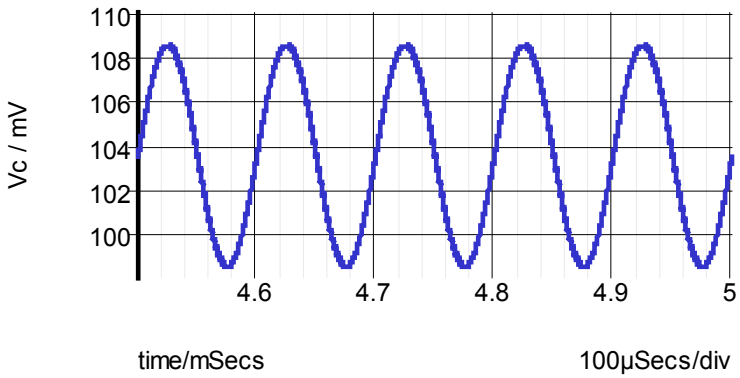

(a) V_c waveform.

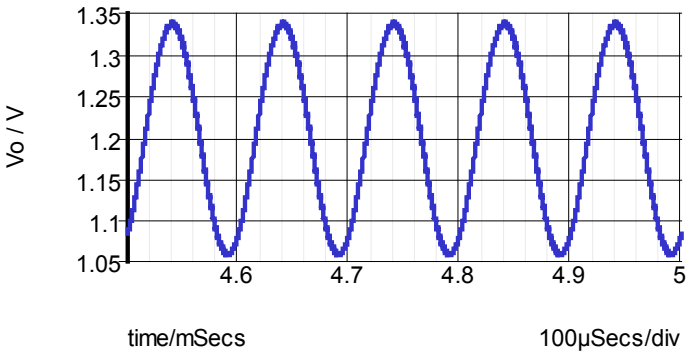

(b) V_o waveform.

Figure 2.7. Simulated waveforms with 10-kHz V_c perturbation for a 1-MHz open-loop buck converter.

With the perturbation frequency, f_p, at 10 kHz, the simulated waveforms at V_c and V_o are illustrated in Figure 2.7. According to Figure 2.6, V_d contains components at 10 kHz and the sideband frequencies of 990 kHz, 1.01 MHz, 1.99 MHz, etc. Through the output filter of the converter, these components appear at V_o as well. Since f_p is much lower than

the switching frequency, f_s, all of the sideband frequencies are much higher than f_p. Because of the low-pass feature of the output filter, the dominant component's frequency at V_o is f_p besides the DC and f_s components.

In addition, Figure 2.8 shows the waveforms when f_p is 990 kHz, which is beyond $f_s/2$. The sideband frequencies are 10 kHz, 1.01 MHz, 1.99 MHz, etc. Because f_s-f_p=10kHz is much lower than f_p, the output filter has more attenuation at f_p than at f_s-f_p. Hence, the 10-kHz sideband frequency component is larger than the perturbation-frequency component. In the simulated V_o waveforms, the sideband component at 10 kHz is the dominant one.

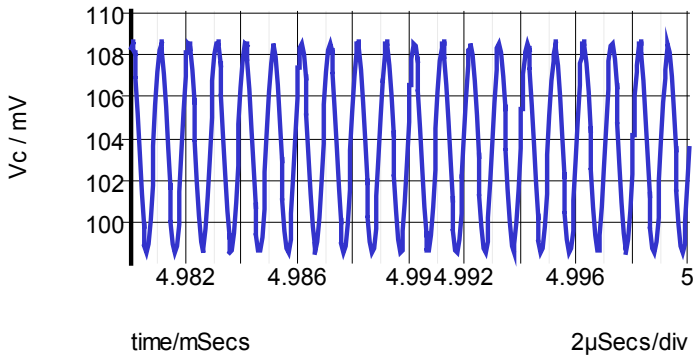

(a) V_c waveform.

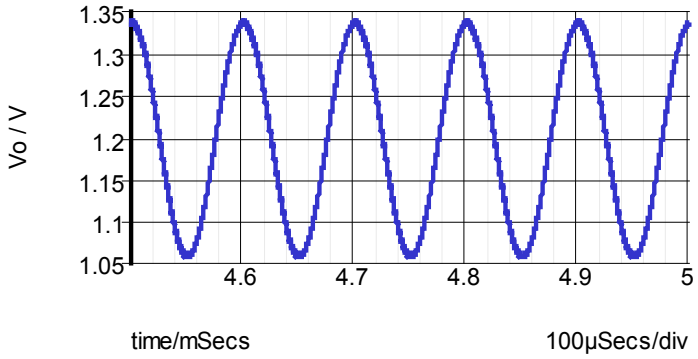

(b) V_o waveform.

Figure 2.8. Simulated waveforms with 990-kHz V_c perturbation for a 1-MHz open-loop buck converter.

In these simulation cases, significant sideband components are observed at V_o when the perturbation frequency is approaching $f_s/2$ or higher than $f_s/2$. Compared with that of the perturbation frequency, the magnitude of the sideband component cannot be ignored. Therefore, the system performance cannot be reflected by only considering the perturbation-frequency components, as shown in Figure 2.9.

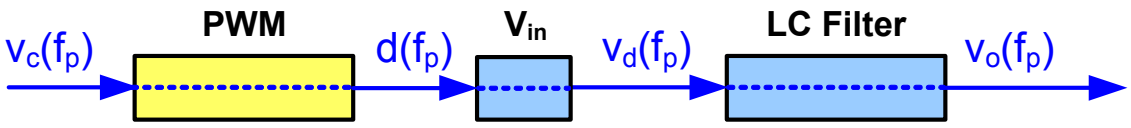

Figure 2.9. The frequency-domain representation including only the perturbation-frequency components.

Normally, the case with the perturbation frequency, f_p, below the switching frequency, f_s, is considered. Under this condition, the lowest sideband frequency is f_s-f_p. Assuming the other sideband components can be well attenuated by the low-pass filter, Figure 2.10 represents the system including the sideband components at f_s-f_p. For the high-frequency perturbation cases, the sideband components should be addressed since the low-pass filter of the power stage does not have good attenuations for them.

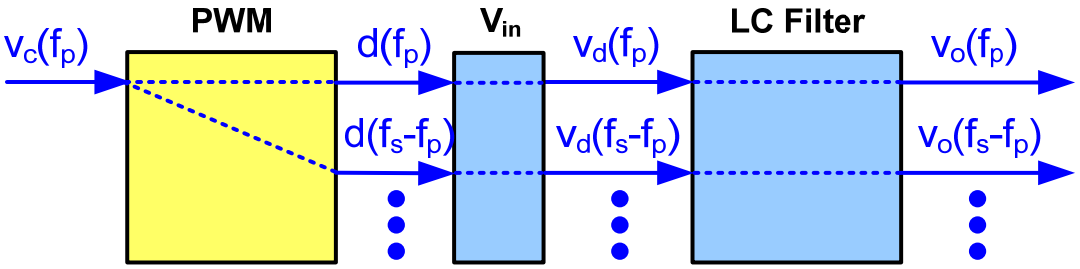

Figure 2.10. The frequency-domain representation for the open-loop buck converter with sideband components.

When the perturbation frequency is $f_s/2$, there is only the perturbation frequency appearing at the output, as shown in Figure 2.4. It has been demonstrated [34] that the relative phase, θ, between V_c and V_r, as shown in Figure 2.11, influences the magnitude and phase responses. Therefore, the system is expressed in the frequency domain as shown in Figure 2.12, where θ is included in the PWM function.

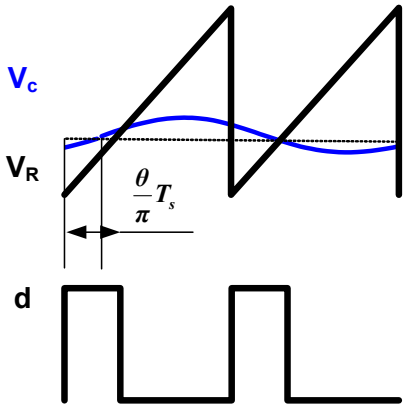

Figure 2.11. Control voltage perturbation waveforms at $f_s/2$.

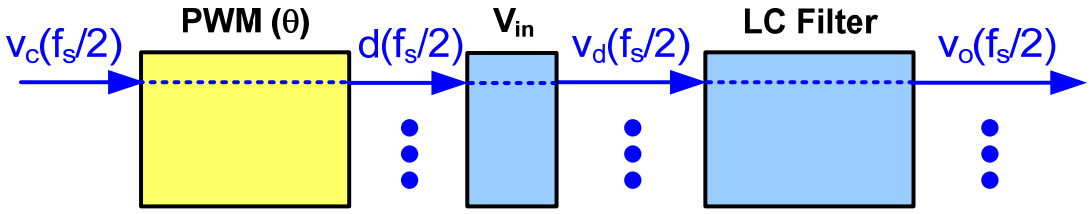

Figure 2.12. The frequency-domain representation for the open-loop buck converter when $f_p=f_s/2$.

In summary, for the open-loop buck converters, when the perturbation frequency is approaching, equal to, or higher than half of the switching frequency, the system performance cannot be represented by the conventional average model. The sideband components and the aliasing effect must be taken into consideration. The focus of this dissertation is not at half of the switching frequency; therefore, the remaining discussion addresses the sideband components only. Unless specially mentioned, it is assumed that $0<f_p<f_s$ and $f_p \neq f_s/2$.

2.3 Sideband Effect of PWM Converters with Feedback Loop

For the open-loop buck converter in Figure 2.1, although there exist sideband components at the output voltage, there is only one perturbation frequency at the PWM comparator input. If the sideband components can be calculated based on the perturbation, the system performance is predictable. However, for buck converters with closed-loop control, as in Figure 1.11, the system becomes much more complicated.

Figure 2.13 illustrates the relationship between the components of f_p and f_s-f_p. The generated sideband component, $V_o(f_s$-$f_p)$, is fed back through the voltage compensator, H_v, and added to the perturbation sources. Consequently, the control voltage, V_c, includes both the perturbation-frequency component, $V_c(f_p)$, and the sideband component, $V_c(f_s$-$f_p)$, which comes from $V_o(f_s$-$f_p)$. Again, as $V_c(f_s$-$f_p)$ is sent into the PWM comparator, it generates the perturbation-frequency component of $V_d'(f_p)$ at the output of the comparator as well. Consequently, the f_p component at V_o includes two parts, as shown in Figure 2.14. The part of $V_o(f_p)$ is from $V_c(f_p)$, and the part of $V_o'(f_p)$ comes from $V_c(f_s$-$f_p)$.

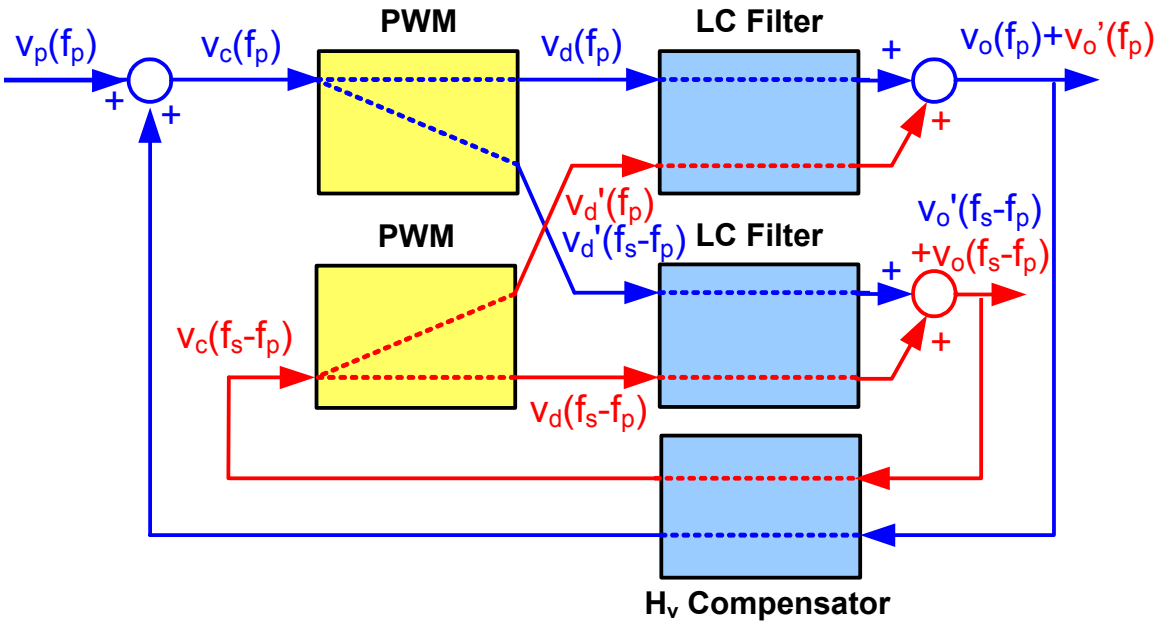

Figure 2.13. The sideband effect in a voltage-mode-controlled buck converter.

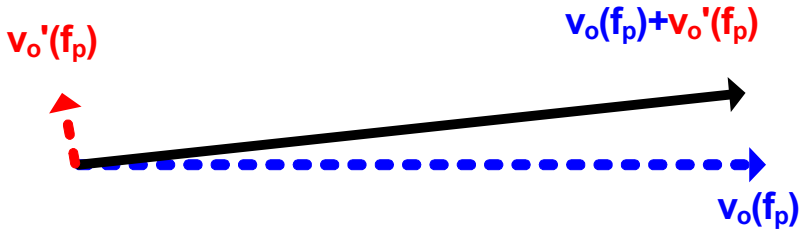

Figure 2.14. Space vector representation of output voltage components at f_p with sideband effect.

Therefore, unlike the open-loop case, the input of the PWM comparator, V_c, contains not only the perturbation-frequency components, but also the sideband components. Through the PWM comparator, the sideband components and the perturbation-frequency components are coupled. The sideband effect happens in the closed-loop converters, i.e., the perturbation-frequency components are influenced by the fed back sideband components, which are generated by the PWM comparator.

In the conventional average model, only the f_p component coming from $V_c(f_p)$ are included, as shown in Figure 2.15. If the influence from the sideband components, $V_o'(f_p)$, is so small that it can be ignored, the average model might be good enough. Otherwise, the sideband frequencies should be considered to accurately represent the system performance in the model.

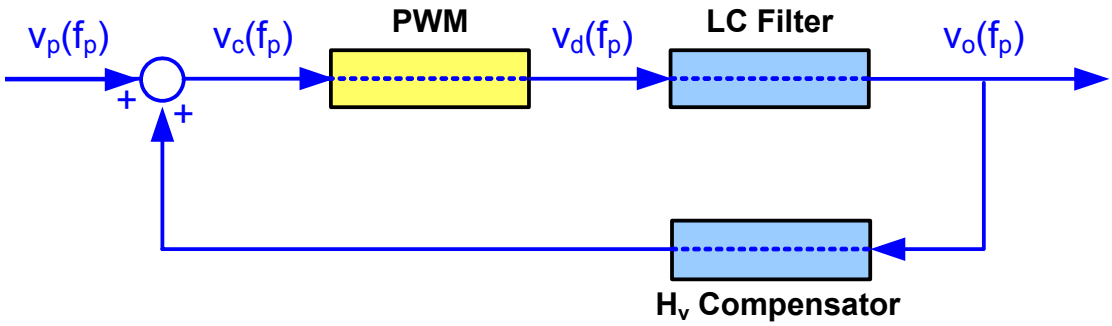

Figure 2.15. The frequency-domain representation for a voltage-mode-controlled buck converter including only the perturbation-frequency components.

To qualitatively investigate the validity of the average model for a buck converter with the voltage-mode control, the switching-model simulation is performed with different f_p. A buck converter with the same parameters as those in Section 2.2 is used as the example. The voltage-loop bandwidth is 100 kHz with a 67° phase margin.

First, it is studied of the case with a V_c perturbation of 40-mV magnitude and 10-kHz frequency, which is very low compared with the 1-MHz switching frequency. As shown in Figure 2.16, V_o is dominated by the 29-mV 10-kHz component and the switching ripples. The 2-μV 990-kHz sideband component at V_o is much smaller than the 10-kHz component. When these components go through the compensator and the inserted perturbation source,

it is observed that at V_c, there exist a 1-mV 10-kHz component and a 32-μV 990-kHz sideband component, as shown in Figure 2.17. Therefore, $V_c(f_p)$ is the dominant component at the input of the PWM comparator.

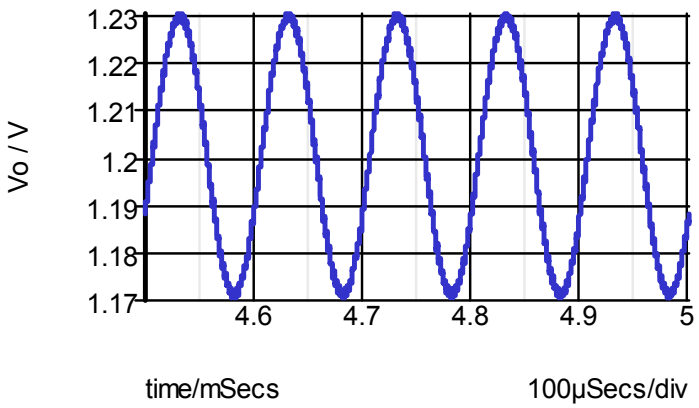

(a) Voltage waveform at V_o.

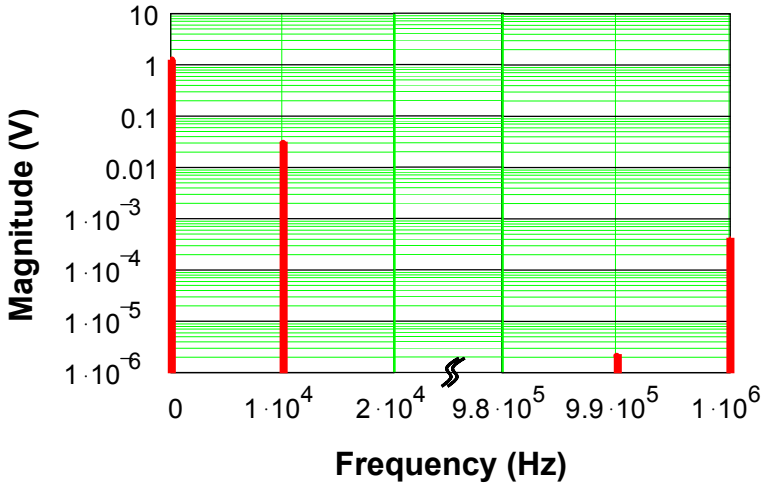

(b) Spectra at V_o.

Figure 2.16. Simulated V_o with a 10-kHz perturbation for a 1-MHz voltage-mode-controlled buck converter.

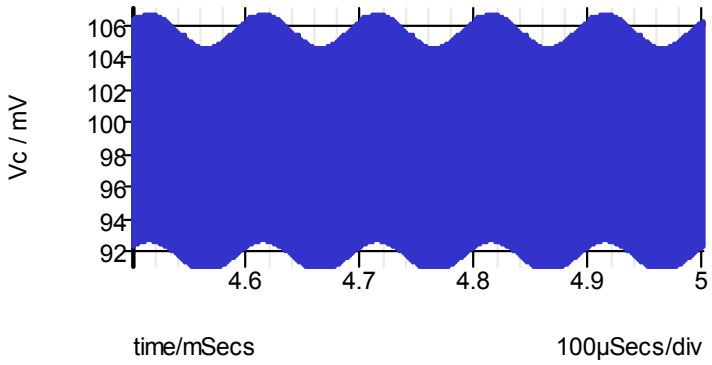

(a) Voltage waveform at V_c.

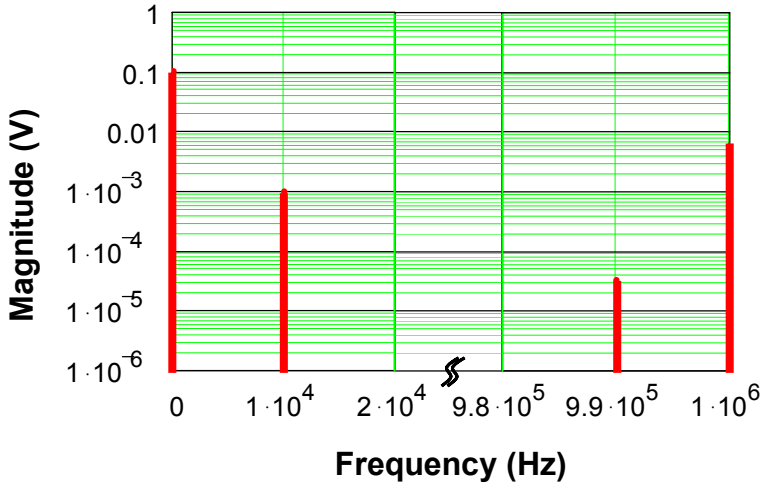

(b) Spectra at V_c.

Figure 2.17. Simulated V_c with a 10-kHz perturbation for a 1-MHz voltage-mode-controlled buck converter.

Through simulation, it is obtained the waveforms of $V_o(f_p)$ and $V_o'(f_p)$ as the results of $V_c(f_p)$ and $V_c(f_s\text{-}f_p)$, respectively. As shown in Figure 2.18, the 28-mV $V_o(f_p)$ is much larger than the 1-mV $V_o'(f_p)$, which means that the influence from the $f_s\text{-}f_p$ components on the f_p component is small. Therefore, under the condition that the perturbation is much lower than the switching frequency, the sideband effect is negligible when measuring the converter responses.

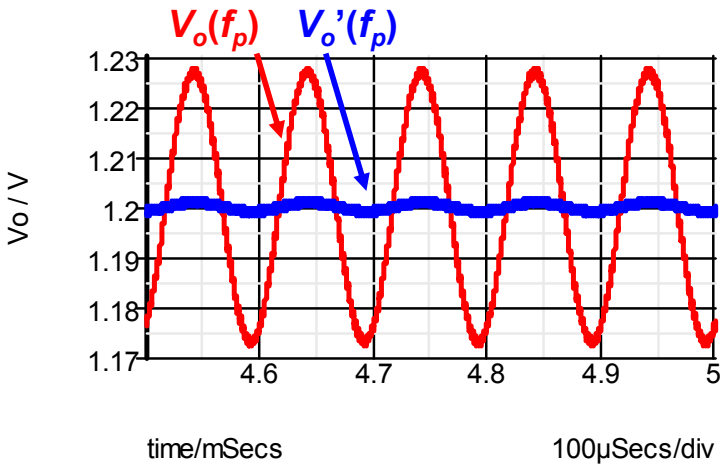

Figure 2.18. Simulated $V_o(f_p)$ and $V_o'(f_p)$ for the 1-MHz voltage-mode-controlled buck converter. (Red line: $V_o(f_p)$; Blue line: $V_o'(f_p)$.)

With a 990-kHz 40-mV perturbation, Figure 2.19 illustrates the simulated waveform at V_o. Because the 10-kHz sideband frequency is much lower than the perturbation frequency, V_o is dominated by the 29-mV 10-kHz component and the switching ripples. The 2-µV 990-kHz sideband component at V_o is much smaller than the 10-kHz component. Consequently, there is significant 10-kHz component and small 990-kHz component after the voltage compensator. However, because of the inserted 990-kHz perturbation source, V_c includes large magnitude components at both 10 kHz and 990 kHz. As shown in Figure 2.20 and Figure 2.21, the 10-kHz and 990-kHz components have similar magnitude of 39 mV and 40 mV, respectively. Therefore, the influence from $V_c(f_s\text{-}f_p)$ is significant, and the $V_o'(f_p)$ component cannot be ignored.

Through simulation, it is obtained V_o's spectra as the results of $V_c(f_p)$ and $V_c(f_s\text{-}f_p)$, respectively. As shown in Figure 2.22, the 79-µV $V_o'(f_p)$ magnitude is very close to the 81-µV $V_o(f_p)$ component, which means that there is significant influence from the $f_s\text{-}f_p$ components on the f_p component. Therefore, under the condition that the perturbation frequency is high, the sideband effect cannot be neglected when measuring the converter responses.

From these two cases, it can be told that the sideband effect becomes more significant with a higher f_p and hence lower f_s-f_p. The reason is that the feedback control loop (including the power-stage output filter and the compensator) functions as a low-pass filter. Therefore, there is sufficient attenuation for the sideband components when f_p is low. When f_p is high, the attenuation is weak for f_s-f_p and the sideband effect cannot be ignored.

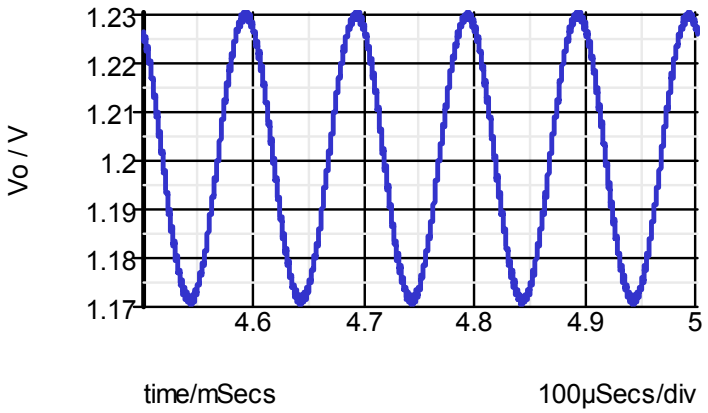

(a) Voltage waveform at V_o.

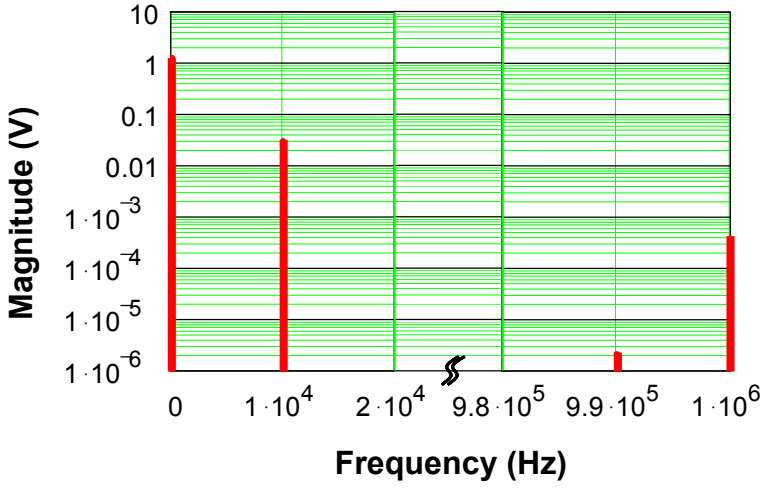

(b) Spectra at V_o.

Figure 2.19. Simulated V_o with a 990-kHz perturbation for a 1-MHz voltage-mode-controlled buck converter.

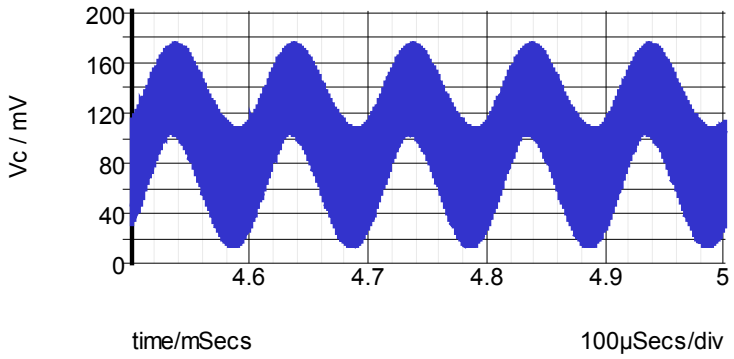

(a) Voltage waveform at V_c.

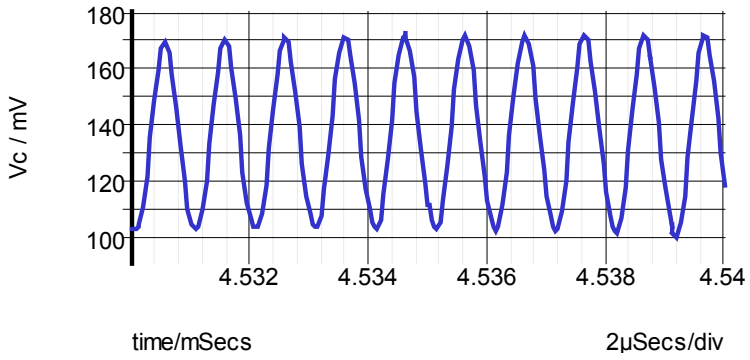

(b) Zoomed voltage waveform at V_c: 990-kHz component.

Figure 2.20. Simulated V_c waveforms with a 990-kHz perturbation for a 1-MHz voltage-mode-controlled buck converter.

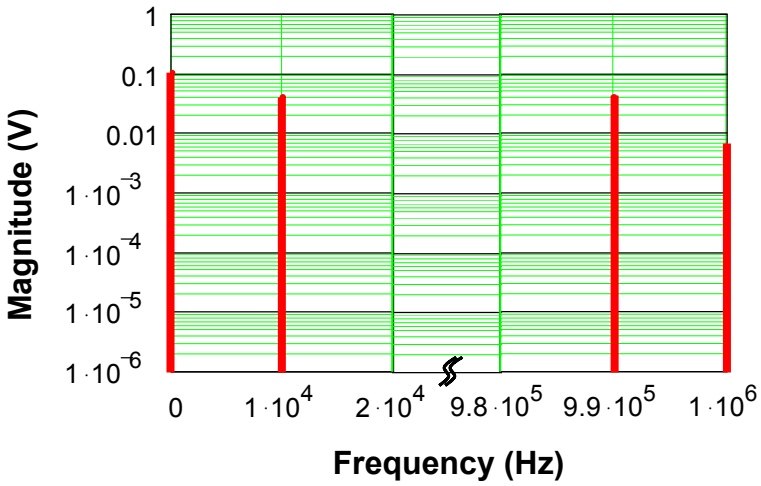

Figure 2.21. Simulated V_c spectra with a 990-kHz perturbation for a 1-MHz voltage-mode-controlled buck converter.

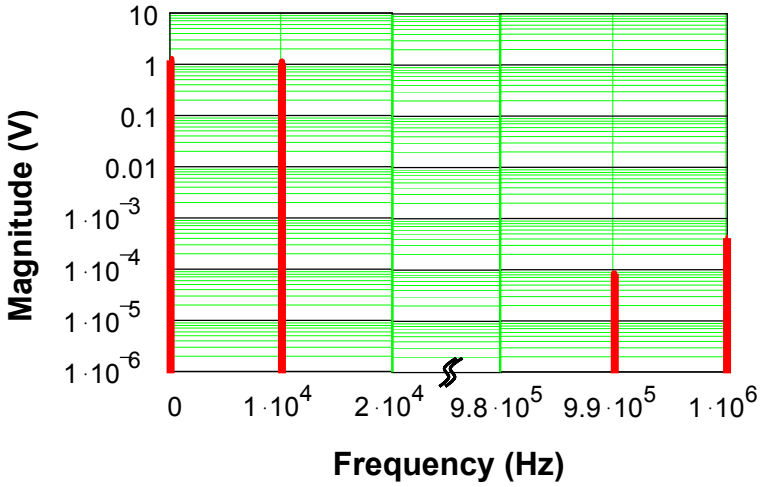

(a) V_o spectra as the result of $V_c(f_p)$.

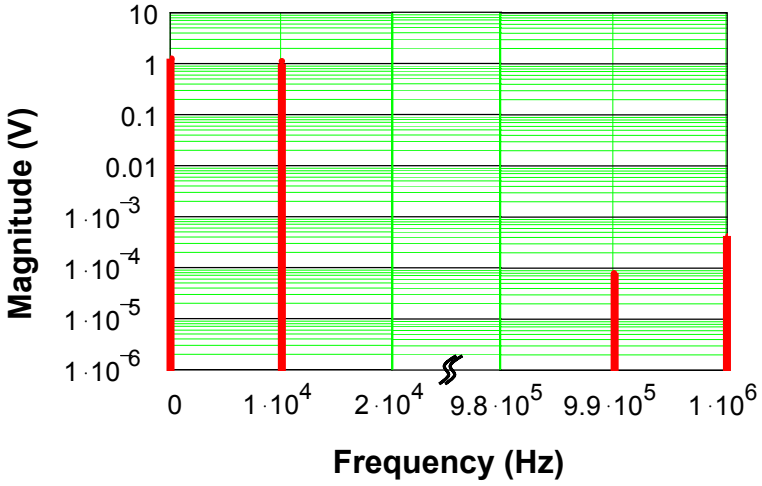

(b) V_o spectra as the result of $V_c(f_s-f_p)$.

Figure 2.22. Simulated V_o spectra as the result of $V_c(f_p)$ and $V_c(f_s-f_p)$ for a 1-MHz voltage-mode-controlled buck converter.

So far, the characteristics of the closed-loop PWM converter have been demonstrated with simulation results qualitatively. Clearly, a simple model only considering the perturbation-frequency component and ignoring the sideband component is not suitable for the high-frequency analysis.

2.4 Small-Signal Transfer Function Measurements and Simulations

A model may not be suitable for the high-frequency analysis, but the question is whether the experimental measurement of transfer functions is correct or not. In this section, it is reviewed how the sideband components are dealt with in the transfer function experimental measurement and simulations.

Figure 2.23 illustrates the network analyzer block diagram [35][36] when measuring the control-to-output transfer functions. The oscillator of the analyzer generates a sinusoidal voltage waveform at a certain perturbation frequency, f_p. When the circuit is running at the steady state, this voltage perturbation is inserted at V_c as shown in Figure 2.1. The vector voltmeter of the analyzer senses the signals at V_c and V_o through two band-pass filters, whose center frequency tracks the oscillator frequency, f_p. The bandwidth of the band-pass filter is very narrow, so that only the f_p components of sensed signals are sent to the vector voltmeter. Then, it is calculated for the magnitude and phase relationships between the two signals' f_p components. Normally, to reduce the influence from noises, the same measurement is repeated several times and then averaged for one frequency. The perturbation frequency, f_p, is swept in the range where the frequency response is desired to be obtained. After applying this process at numbers of f_p values, the transfer function from V_c to V_o is obtained.

With this measurement scheme, the converter's small-signal characteristics cannot be reflected at the switching frequency [36], because at this frequency, the small-signal perturbation is overwhelmed by the switching ripples. Usually, a spike exists in the transfer function at the switching frequency.

At half of the switching frequency, since there is the averaging algorithm, the measured response cannot reflect the characteristics with the different phases between the perturbation and the sawtooth ramp. Even when the averaging function is disabled, the measurement result only represents the performance at a certain phase value. Therefore, the measurement result is not good at half of the switching frequency.

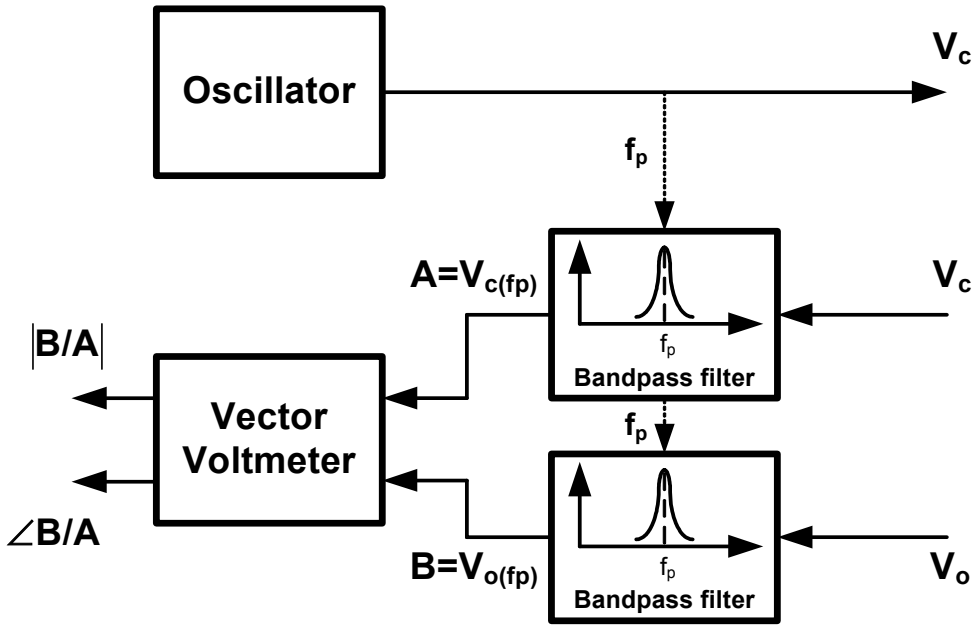

Figure 2.23. Network analyzer block diagram of measuring the control-to-output transfer function.

At other frequencies, because it is the total $V_o(f_p)$ that is measured, it does not matter whether it is the result from $V_c(f_p)$ or $V_c(f_s\text{-}f_p)$. The influences on $V_o(f_p)$ from all the frequency components at V_c are included. Therefore, the accurate response of $V_o(f_p)$ can be obtained when there is an inserted perturbation. However, it should be noted that the measurement does not reflect the response of $V_o(f_s\text{-}f_p)$. Under some condition, such as under very high frequency perturbations, the response at $f_s\text{-}f_p$ is even more important that that at f_p. It results in a limitation if the system response is reflected by using only the measured transfer function.

To obtain the transfer function by simulation accurately, the switching model should be used with the same setup as the network analyzer. Although this setup can be achieved by most kinds of the software, such as Saber, PSpice, MATLAB, etc, the calculation time are normally very long. Unlike these kinds of software, SIMPLIS can finish the simulation very fast due to its unique algorithm. Because of these merits, the SIMPLIS simulation is used as the virtual testbed to analyze the converters and to verify the models in this dissertation. However, it should be noted that there is one difference between the measurement and the SIMPLIS simulation at the switching frequency. Since SIMPLIS can tell the difference between the steady-state ripple and the response from the perturbation

[37], the simulated transfer function is different from that of the measurement at the switching frequency.

In summary, one can use the measured or simulated loop gain to analyze the high-frequency performance. And the sideband effect is able to be included. However, the limitation of using the measurement and the simulation tool is that it cannot reflect the inherent characteristic of the converter. In addition, it cannot predict the sideband components in the converter and the phenomena at half of the switching frequency. Therefore, it is an advantage to predict and explain the transfer function by the modeling approach as well.

2.5 Previous Modeling Approaches

As a basis for the high-frequency modeling to address the sideband effect, the previous modeling approaches are briefly reviewed in this section.

To predict the sub-harmonic oscillations for peak-current-control converters, several models based on the sample-data approach have been proposed [38][39][40][41]. Basically, this approach includes the influences from the sampling, so that the high-frequency performance is able to be addressed. To include the sampling characteristics, the converter is modeled in the *z*-domain first. Then, it is possible to transform the model to the *s*-domain. The instability issue with peak-current control is predicted successfully using this approach. However, with the sample-data approach, it is difficult to explain the physical sense of the system performances.

The harmonic balance approach was proposed to model the beat-frequency poles in the resonant converters [42][43][44]. As shown in Figure 2.24, a converter system normally can be divided into two subsystems: a linear subsystem, which is relatively easy to model, and a nonlinear subsystem. In the average model, it is assumed that the low-pass filters in the system sufficiently attenuate all the frequency components except for the fundamental frequency. Therefore, the describing function is used to model the nonlinear subsystem only at the fundamental frequency. However, with band-pass filter in the resonant converter, this assumption is not good any more, and the beat frequency should be modeled.

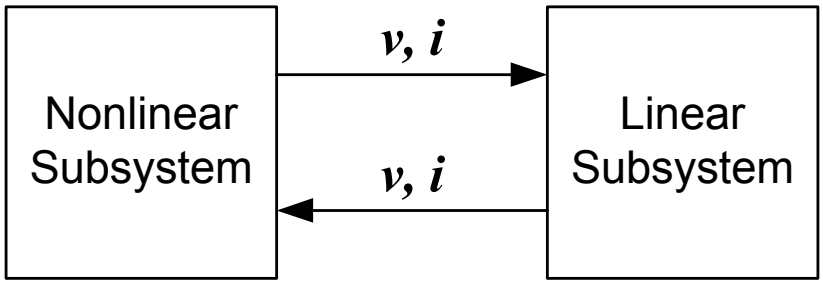

Figure 2.24. Partitioning of a converter system: linear subsystem and nonlinear subsystem.

To include the components at other frequencies, such as the beat frequency, it should be considered with multiple input and output frequency components. Therefore, the extended describing functions are used to represent the relationships between the inputs and outputs.

For example, a typical nonlinear subsystem is illustrated in Figure 2.25 [42], where x is the state vector, u is the input vector, $s(t)$ is a driving signal, and

$$y_i = \dot{x}_i = f_i(x, u, s(t)) . \tag{2.1}$$

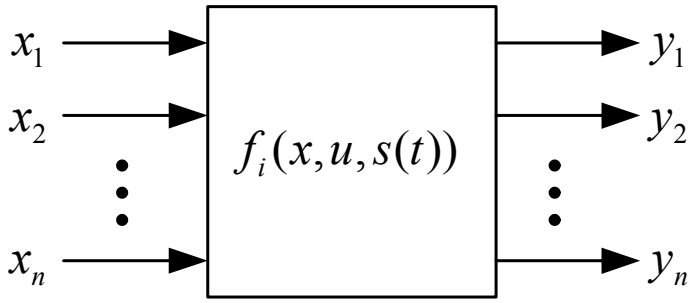

Figure 2.25. A typical nonlinear subsystem.

Containing multiple components at frequency ω_k, x_i and y_i can be represented as

$$x_i = \sum_k X_{ik} e^{j\omega_k t} . \tag{2.2}$$

and

$$y_i = \sum_k Y_{ik} e^{j\omega_k t} \ . \tag{2.3}$$

Using the extended describing functions, the nonlinear subsystem is expressed in the frequency domain as in Figure 2.26 [42]. z is the coefficient vector for x, representing both the real parts and the imaginary parts at different frequencies, and p is the control parameters for $s(t)$. Therefore, in the frequency domain, (2.1) is expressed as

$$\sum_k \left(\frac{dX_{ik}}{dt} + j\omega_k X_{ik}\right) e^{j\omega_k t} = \sum_k F_{ik}(z,u,p) e^{j\omega_k t} \ . \tag{2.4}$$

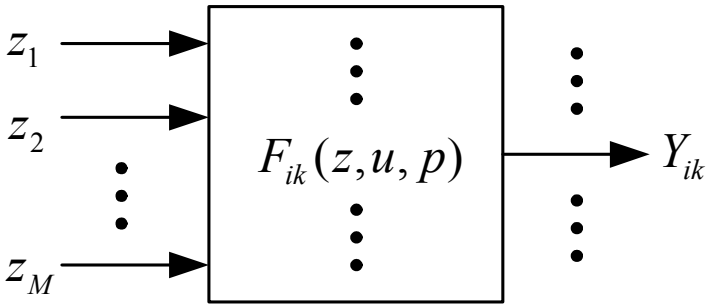

Figure 2.26. Representation by extended describing functions for a typical nonlinear subsystem.

The harmonic balance approach equates the coefficients for both sides of (2.4), so that it removes the terms of $e^{j\omega kt}$. Using this approach, different frequency components are derived and the model for the nonlinear subsystem is obtained. By including the sideband frequency components in the model, it predicts the resonant converter's transfer functions successfully.

For the PWM converters, the sideband frequency cannot be ignored when the perturbation frequency is relatively high. Under these conditions, the harmonic balance approach has also been applied [36][45]. This approach is also able to include the influences from the sampling on the transfer functions. Therefore, the high-frequency performances of converters are predicted very well.

In summary, the harmonic balance method looks promising for further study to explain the sideband effect. However, because of large amount of calculations, most research using the harmonic balance approach are based on computer programs

[42][43][44][45]. Therefore, the physical essence of the performance due to the sideband components is not yet clarified. Although it provides much more accurate high-frequency results, it is not widely utilized by the designers.

For the VR applications in this dissertation, the investigation target is the buck converter. As shown in Figure 2.27, considering ideal components and constant input voltage, the PWM comparator is the only nonlinearity in the single-phase buck converter with voltage-mode control. Therefore, if the extended describing functions for the PWM comparator are derived, it is possible to obtain a simple model including the sideband components.

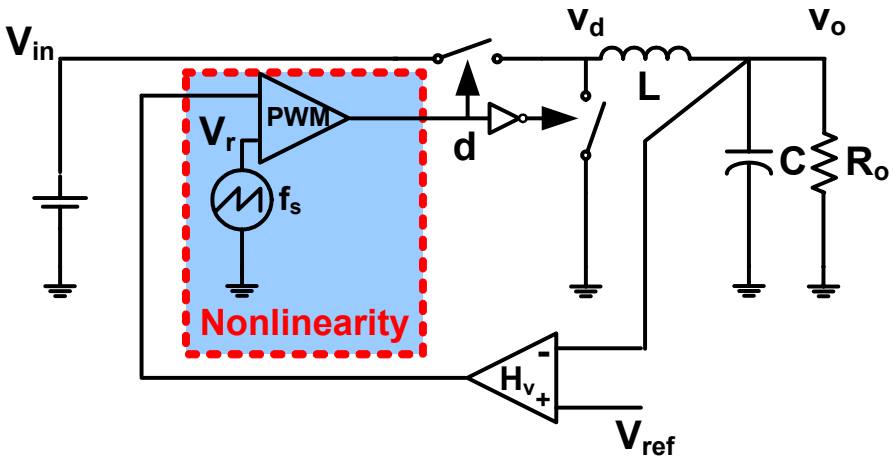

Figure 2.27. Nonlinearity in the single-phase voltage-mode-controlled buck converter with constant input voltage.

2.6 Summary

Because of the sampling characteristic of the PWM comparator, sideband components are generated in the open-loop buck converters. Due to the low-pass output filter in the power stage, the output voltage is dominated by the perturbation-frequency components when the perturbation frequency, f_p, is low. When f_p is approaching half of the switching frequency or even higher, the sideband components at the output voltage cannot be ignored anymore.

In a closed-loop buck converter, the sideband component appears at the input of the comparator and generates the perturbation-frequency component again, and the sideband

effect happens. The f_p components are partially contributed by the sideband components. However, in the average model, only the contribution from the f_p component is counted. Therefore, the average model fails to predict the response at the perturbation frequency. When the network analyzer or the simulation software analyzes the f_p components, it does not tell what the source of these components is. Both the part generated by f_p components itself and that caused by the sideband components through the coupling of the PWM comparator are counted for calculation the transfer functions. Therefore, they can well reflect the response at the perturbation frequency.

As the basis for further modeling and analysis, the existing high-frequency modeling approaches are reviewed. Both the sample-data approach and the harmonic approach have demonstrated their validity. However, these models depend on computer programs for the calculations. Therefore, it is not easy to be utilized to explain the physical meaning of the system performances. Nevertheless, the harmonic balance approach can be simplified for buck converters in the VR applications. Since the rest of the converter system is linear functions, the essence is to derive the extended describing functions for the nonlinear PWM comparator.

In summary, with closed loops, the sideband effect happens in the PWM converters. To provide an analytical insight, a complete model that includes the sideband components is needed for further analysis.

Chapter 3. Multi-Frequency Modeling for Buck Converters

Higher bandwidth is desired for less output capacitors in VR applications. However, as shown in Figure 1.12, there exist excessive phase delays at high frequency for the single-phase buck converter with high-bandwidth designs. As analyzed in Chapter 2, the sideband effect happens and results in the observed phase delays. To provide an analytical insight for the high-frequency characteristics of PWM converters, this chapter develops the multi-frequency model that includes the sideband effects.

3.1 Modeling of the PWM Comparator

In a buck converter with ideal components and a constant input voltage, the only nonlinear function is the PWM comparator. If the extended describing functions considering the sideband components can be derived, the high-frequency performance can be modeled by combining them with the transfer functions of the linear parts in the converter.

In the PWM comparator of the buck converter with output voltage feedback, its input of the control voltage, V_c, and output of the duty cycle, d, both include multiple frequency components. Considering the perturbation frequency, f_p, and the sideband frequency, f_s-f_p, the PWM block is represented as in Figure 3.1.

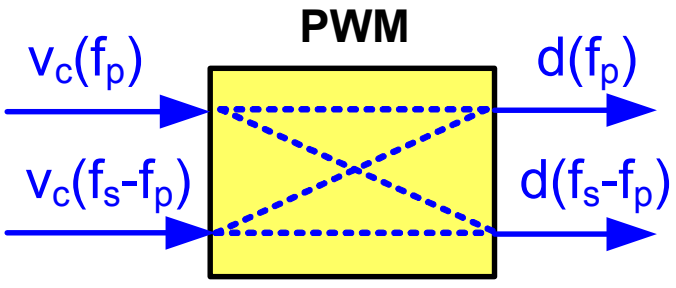

Figure 3.1. Nonlinearity of the PWM comparator.

The describing function of the PWM comparator for the same frequency input and output has been derived using the Fourier analysis [46]. For the relationship between different frequencies, a similar approach is employed in this dissertation. As an example, the trailing-edge modulation, as shown in Figure 3.2, is explored. The same method is applicable to analyze the leading-edge and double-edge modulations, as demonstrated in Appendix A.

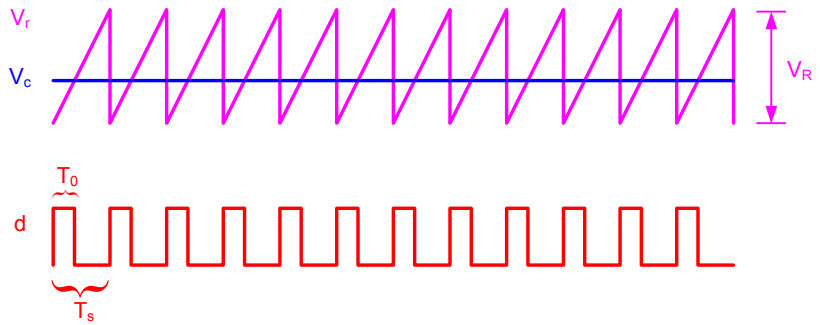

(a) Waveforms at steady state.

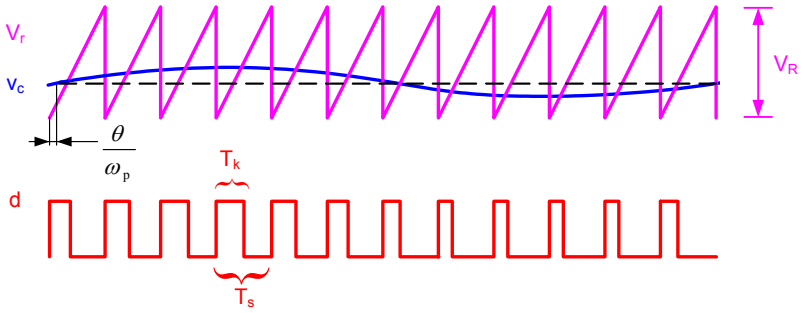

(b) Waveforms with a sinusoidal perturbation at the control voltage.

Figure 3.2. Input and output waveforms of the trailing-edge PWM comparator.

With a sinusoidal control voltage of

$$v_c(t) = V_c + \hat{v}_c \sin(\omega_p t - \theta), \tag{3.1}$$

the duty ratio in the *k*-th cycle is

$$D_k = \frac{T_k}{T_s} = D + \frac{\hat{v}_c \sin(\omega_p[(k-1)T_s + DT_s + (D_k - D)T_s] - \theta)}{V_R}, \tag{3.2}$$

where T_k is the on-time of the k-th cycle, T_s is the switching period, and V_R is the peak-to-peak voltage of the sawtooth ramp of the PWM comparator. The first term is the steady-state duty cycle,

$$D = \frac{T_0}{T_s} = \frac{V_c}{V_R}. \tag{3.3}$$

Applying the small-signal approximation, the sinusoidal wave's amplitude, $\hat{v}_c$, is much smaller than the DC value, V_c. Consequently, $\omega_p(D_k\text{-}D)T_s$ is small enough. Therefore, the instantaneous value of v_c at $(k\text{-}1)T_s+DT_s+(D_k\text{-}D)T_s$ can be represented by the value at $(k\text{-}1)T_s+DT_s$. Then it is obtained that

$$D_k = D + \frac{\hat{v}_c}{V_R} \cdot \sin(\omega_p(k-1)T_s - \phi - \theta), \tag{3.4}$$

where

$$\phi = -\omega_p DT_s. \tag{3.5}$$

With the definition, for a periodical signal, $f(t)$, with period of T, the Fourier coefficient is expressed as

$$f(\omega) = \frac{1}{T}\int_0^T f(t)\mathrm{e}^{-j\omega t}dt. \tag{3.6}$$

The Fourier coefficient of V_c at ω_p is

$$v_c(\omega_p) = \frac{\mathrm{e}^{-j\theta}\hat{v}_c}{2j}. \tag{3.7}$$

To calculate the comparator output waveform's frequency components, it is assumed in this dissertation that the perturbation frequency, ω_p, and the switching frequency, ω_s, have the relationship of

$$\frac{\omega_p}{\omega_s} = \frac{N}{M}, \tag{3.8}$$

where N and M are positive integers. It has been derived [46] that when $\omega_p \neq k\omega_s/2$, k=0, 1, 2, 3, …,

$$d(\omega_p) = \frac{\hat{v}_c e^{-j\theta}}{2jV_R}. \tag{3.9}$$

Then, the describing function of the PWM comparator is derived as a simple gain,

$$F_m = \frac{d(\omega_p)}{v_c(\omega_p)} = \frac{1}{V_R}. \tag{3.10}$$

To derive the relationship between the input and the output signals for different frequencies, the similar approach is utilized.

As shown in Figure 2.3, a sideband component contains both a positive frequency and a negative frequency. Mathematically, a real signal can be represented by either one of them. For example, when f_p is less than f_s, the lowest sideband frequency can be expressed by the positive one, f_s-f_p, or the negative one, f_p-f_s. The negative frequency, f_p-f_s, is selected for modeling, because it leads to a simpler mathematical expression of the relationship between the sideband and the perturbation-frequency components.

With the assumption in (3.8), the coefficient at the frequency of ω_p-ω_s for the comparator's output, d, is derived as

$$d(\omega_p - \omega_s) = \frac{1}{2\pi(N-M)} \int_0^{2\pi(N-M)} d(t) e^{-j(\omega_p-\omega_s)t} d[(\omega_p - \omega_s)t]. \tag{3.11}$$

Since

$$d(t) = 1,\ (k-1)T_s < t < (k-1)T_s + T_k. \tag{3.12}$$

and

$$d(t) = 0, (k-1)T_s + T_k < t < kT_s, \tag{3.13}$$

(3.11) is rewritten as

$$d(\omega_p - \omega_s) = \frac{1}{2\pi(N-M)} \sum_{k=1}^{M} \int_{(k-1)(\omega_p-\omega_s)T_s}^{(k-1)(\omega_p-\omega_s)T_s+(\omega_p-\omega_s)T_k} e^{-j(\omega_p-\omega_s)t} d[(\omega_p - \omega_s)t]. \tag{3.14}$$

After manipulations, it is obtained that

$$d(\omega_p-\omega_s)=\frac{j}{2\pi(N-M)}\sum_{k=1}^{M}\mathrm{e}^{-j(k-1)(\omega_p-\omega_s)T_s}\cdot(\mathrm{e}^{-j(\omega_p-\omega_s)T_0}-1)$$
$$+\frac{j}{2\pi(N-M)}\sum_{k=1}^{M}\mathrm{e}^{-j(k-1)(\omega_p-\omega_s)T_s}\cdot\mathrm{e}^{-j(\omega_p-\omega_s)T_0}(\mathrm{e}^{-j(\omega_p-\omega_s)T_s(D_k-D)}-1). \tag{3.15}$$

The first term,

$$T_1=\frac{j}{2\pi(N-M)}(e^{-j(\omega_p-\omega_s)T_0}-1)\sum_{k=1}^{M}e^{-j2\pi(k-1)\frac{N-M}{M}}$$
$$=0, \tag{3.16}$$

when $N/M\neq 0, 1, 2, \ldots$.

Applying the small-signal approximation on the second term,

$$T_2=\frac{j}{2\pi(N-M)}\sum_{k=1}^{M}\mathrm{e}^{-j(k-1)(\omega_p-\omega_s)T_s}\cdot\mathrm{e}^{-j(\omega_p-\omega_s)T_0}(\mathrm{e}^{-j(\omega_p-\omega_s)T_s(D_k-D)}-1)$$
$$=\frac{j\mathrm{e}^{-j(\omega_p-\omega_s)DT_s}}{2\pi(N-M)}\sum_{k=1}^{M}\mathrm{e}^{-j(k-1)(\omega_p-\omega_s)T_s}\cdot[-j(\omega_p-\omega_s)T_s(D_k-D)]. \tag{3.17}$$

With (3.4), it is obtained that

$$T_2=\frac{\mathrm{e}^{-j(\omega_p-\omega_s)DT_s}}{M}\frac{\hat{v}_c}{2jV_R}\cdot(\sum_{k=1}^{M}\mathrm{e}^{-j(\theta+\phi)}+\mathrm{e}^{j(\theta+\phi)}\sum_{k=1}^{M}\mathrm{e}^{-j(2\pi(k-1)\frac{2N-M}{M})})$$
$$=\frac{\mathrm{e}^{jD2\pi}\cdot\mathrm{e}^{-j\theta}\hat{v}_c}{2jV_R}. \tag{3.18}$$

when $N/M\neq 0, 0.5, 1, 1.5, \ldots$, i.e. $\omega_p\neq k\omega_s/2$, $k=0, 1, 2, 3, \ldots,$.

Considering the Fourier coefficient of V_c in (3.7), it is derived that

$$F_{m-}=\frac{d(\omega_p-\omega_s)}{v_c(\omega_p)}=\frac{1}{V_R}\cdot\mathrm{e}^{jD2\pi}. \tag{3.19}$$

With the same approach, it is obtained that at $\omega_p\neq k\omega_s/2$, $k=0, 1, 2, \ldots$

$$F_{m+}=\frac{d(\omega_p)}{v_c(\omega_p-\omega_s)}=\frac{1}{V_R}\cdot\mathrm{e}^{-jD2\pi}. \tag{3.20}$$

Based on (3.10), (3.19), and (3.20), the extended describing functions of the trailing-edge PWM comparator are summarized in Table 3.1 when $\omega_p \neq k\omega_s/2$, k=0, 1, 2, … Because of the small-signal assumption, the sideband component and the perturbation-frequency component have the same magnitude.

Table 3.1. Extended describing functions of the trailing-edge PWM comparator.

		Output components	
		$d(\omega_p)$	$d(\omega_p - \omega_s)$
Input components	$v_c(\omega_p)$	$F_m = \frac{1}{V_R}$	$F_{m-} = \frac{1}{V_R} \cdot e^{jD2\pi}$
	$v_c(\omega_p - \omega_s)$	$F_{m+} = \frac{1}{V_R} \cdot e^{-jD2\pi}$	$F_m = \frac{1}{V_R}$

Next, it should be investigated how to establish the relationship when there is multiple input components at V_c.

If the control voltage contains two frequency components,

$$v_c(t) = V_c + \hat{v}_{c1} \sin(\omega_1 t - \theta_1) + \hat{v}_{c2} \sin(\omega_2 t - \theta_2), \tag{3.21}$$

with small-signal approximation,

$$D_k = D + \frac{\hat{v}_c}{V_R} \cdot \sin(\omega_1 (k-1)T_s - \omega_1 DT_s - \theta_1) + \frac{\hat{v}_c}{V_R} \cdot \sin(\omega_2 (k-1)T_s - \omega_2 DT_s - \theta_2) \cdot \tag{3.22}$$

Based on the characteristic of the Fourier analysis, super-positioning can be used to deal with the cases with multiple input frequency components. Therefore, with the derived relationships in Table 3.1, Figure 3.3 illustrates the model of the trailing-edge PWM comparator.

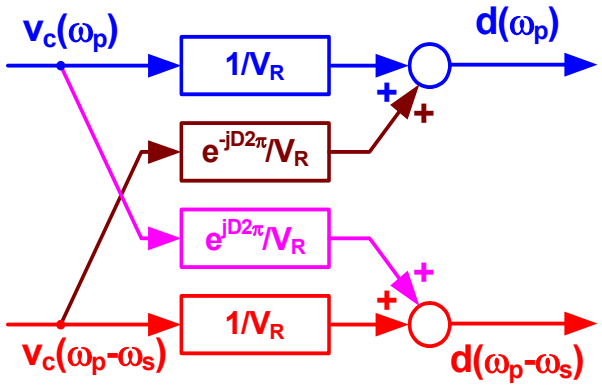

Figure 3.3. The model of the trailing-edge PWM comparator.

Compared with the traditional average model, the cross-coupling effect is included additionally. Combining the model for the comparator with the model of the rest of the converter, a high-frequency model can be obtained.

3.2 The Multi-Frequency Model of Buck Converters

To obtain the model for the closed-loop buck converter, the relationship from the duty cycle to the phase voltage is also necessary. For simplicity, the input voltage for the buck converter is assumed constant. The cases with input perturbations are discussed in Appendix B. With constant input voltage, the shape of the phase voltage, V_d, is the same as that the duty cycle, d, as shown in Figure 2.5. There is only a difference of the magnitude with the relationship of a simple gain.

In the time domain,

$$v_d(t) = d(t) \cdot V_{in}, \tag{3.23}$$

which leads to the relationship in the frequency domain as

$$v_d(\omega) = d(\omega) \cdot V_{in}. \tag{3.24}$$

Therefore, the function of the switches with a constant input voltage can be expressed by Figure 3.4. Since the power stage's output LC filter and the feedback compensator are simple linear stages, based on Figure 3.3 and Figure 3.4, the model considering the sideband effect can be obtained.

Figure 3.4. Frequency-domain relationship between the phase voltage and the duty cycle assuming constant input voltage.

For a single-phase voltage-mode-controlled buck converter with load current perturbations as in Figure 3.5, the model is illustrated in Figure 3.6. In this proposed model, there are two feedback loops, which represent the perturbation frequency and the sideband frequency respectively. Therefore, it is named as the multi-frequency model.

Although each feedback loop represents a certain frequency, these two loops are coupled with each other through the PWM comparator. For the loop representing a certain frequency ω, the loop gain is

$$T_{av}(\omega) = V_{in} / V_R \cdot H_v(\omega) \cdot G_{LC}(\omega), \tag{3.25}$$

where $H_v(\omega)$ is the transfer function of the compensator, and $G_{LC}(\omega)$ is the phase-voltage-to-output transfer function of the LC filter,

$$G_{LC}(\omega) = \frac{C(\omega) // R_o}{L(\omega) + C(\omega) // R_o}, \tag{3.26}$$

where R_o is the load resistance, and $L(\omega)$, $C(\omega)$ are the impedance of the inductor and capacitor, respectively.

Clearly, the loop gain T_{av} at the perturbation frequency, ω_p, is exactly the loop gain in the traditional average model in Figure 3.7. The multi-frequency model adds the influence from sideband effect. Simplifying this influence to a single block, the model is redrawn as in Figure 3.8. The closed-loop impedance is calculated as

$$Z_{o\_cl}(\omega_p) = -\frac{v_o(\omega_p)}{i_o(\omega_p)} = \frac{Z_o(\omega_p)}{1 + T_v(\omega_p)}, \tag{3.27}$$

where

$$T_v(\omega_p) = \frac{T_{av}(\omega_p)}{1 + T_{av}(\omega_p - \omega_s)}, \tag{3.28}$$

is the loop gain that determines the stability and transient performance. Compared with the average model shown in Figure 3.7, the influence of the sideband component is shown in the denominator.

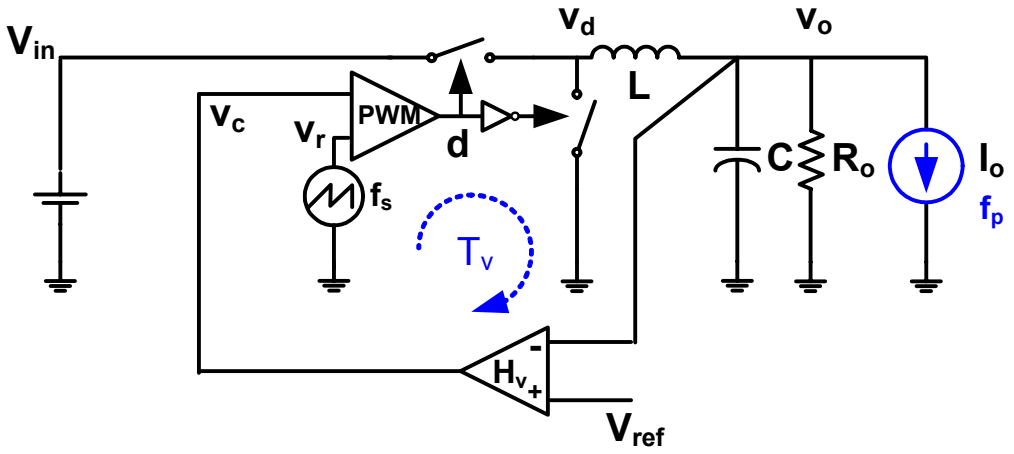

Figure 3.5. A voltage-mode-control buck converter with load-current perturbations.

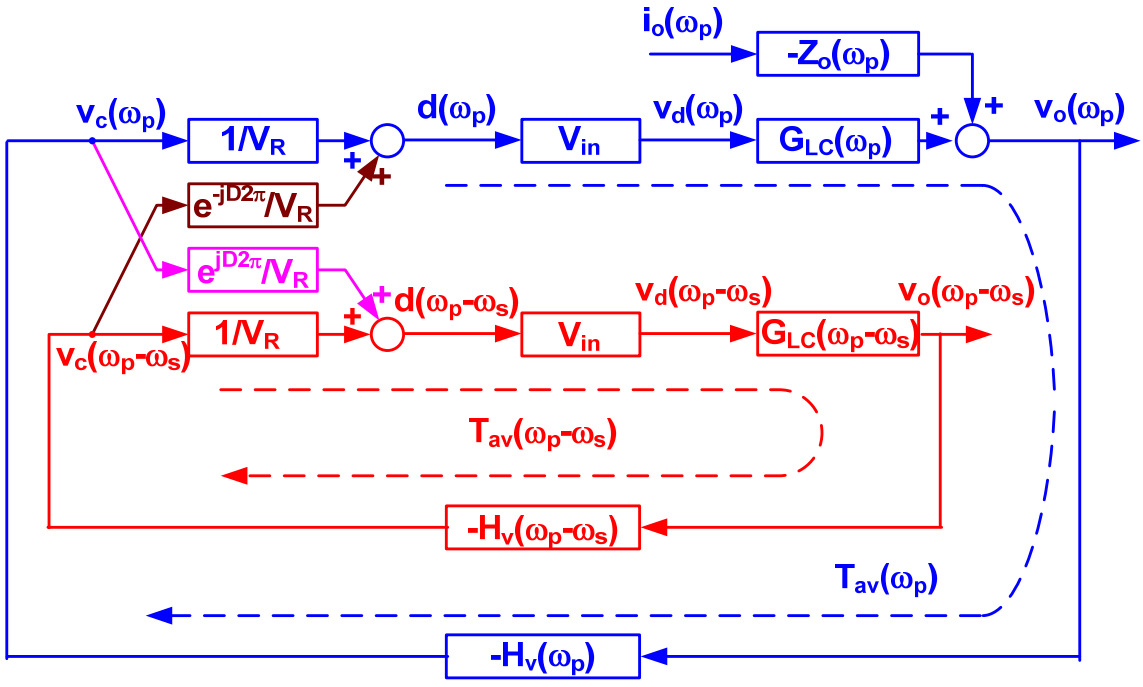

Figure 3.6. The multi-frequency model of a single-phase voltage-mode-controlled buck converter.

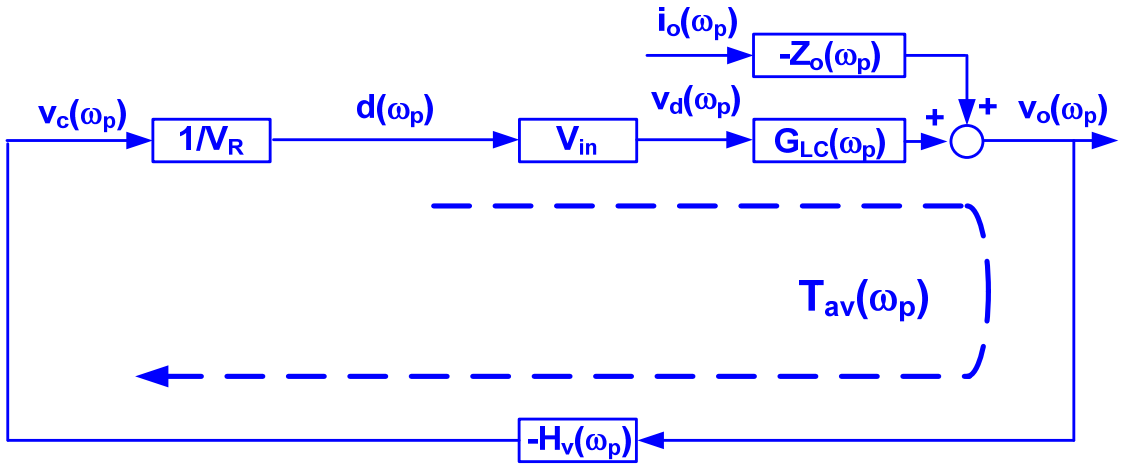

Figure 3.7. The average model of a single-phase voltage-mode-controlled buck converter.

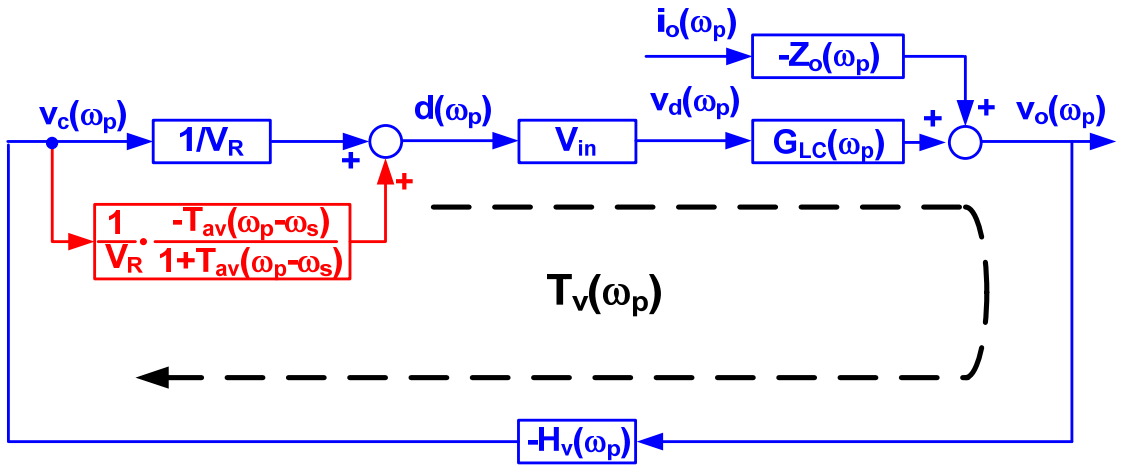

Figure 3.8. Simplified multi-frequency model of a single-phase voltage-mode-controlled buck converter.

To verify the derived model, based on a voltage-mode-controlled 1-MHz single-phase buck converter, Figure 3.9 compares the loop gain in the SIMPLIS simulation, in the average model, and in the multi-frequency model. Figure 3.10 shows the measurement result. For both the magnitude and phase responses, there are significant reductions around the switching frequency. Clearly, while the average model fails to predict the high-frequency performance, the multi-frequency model is accurate.

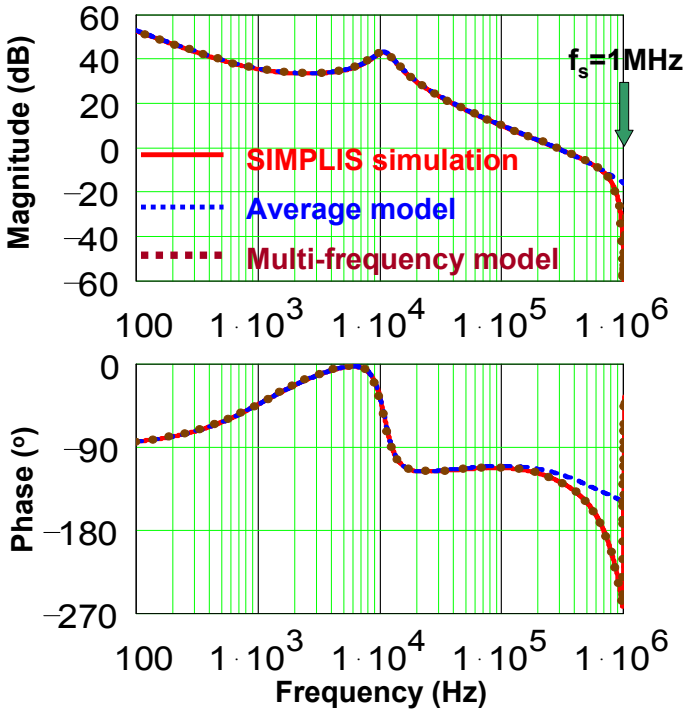

Figure 3.9. Loop gain of a 1-MHz buck converter with voltage-mode control.
(Red solid line: SIMPLIS simulation result; Blue dashed line: average-model result;
Brown dotted line: multi-frequency model result)

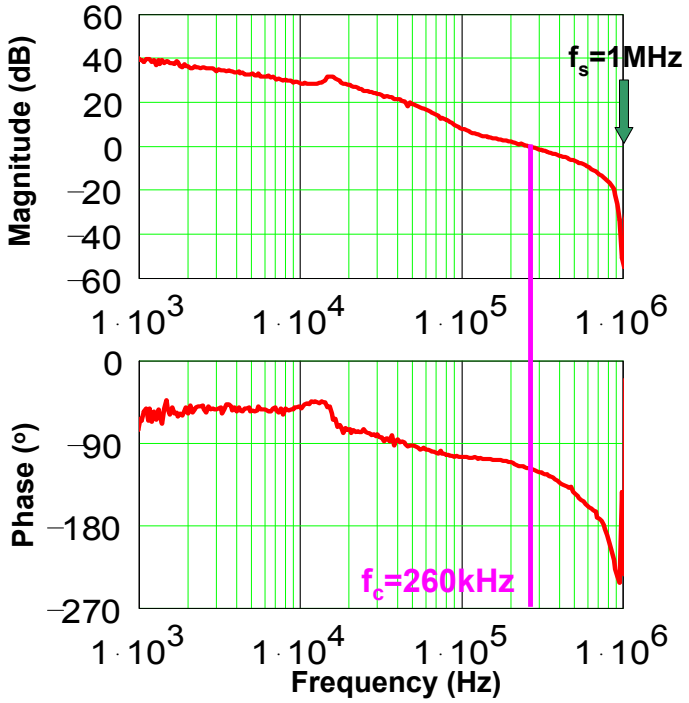

Figure 3.10. Measured loop gain of a 1-MHz single-phase buck converter with voltage-mode control.

With the proposed model, it is then possible to explore the sideband effect analytically. In (3.28), f_p-f_s is a negative frequency when f_p is lower than f_s. It has been derived that for a transfer function $g(\omega)$, the relationships for the magnitude and the phase between a negative frequency and its corresponding positive frequency are expressed by

$$|g(-\omega)|=|g(\omega)|, \tag{3.29}$$

and

$$\arg[g(-\omega)]=-\arg[g(\omega)]. \tag{3.30}$$

With (3.29) and (3.30), the proposed model is capable of explaining the frequency-domain performance. (3.28) indicates that when f_p is located in the low-frequency region, f_p-f_s is out of the bandwidth of T_{av}. Thus, the denominator is approximately equal to one, which means that the sideband effect is very small. Therefore, the loop gain calculated in the average model matches well with that from the simulation.

When f_p becomes higher and f_p-f_s is around the crossover frequency of T_{av}, the denominator of (3.28) begins to be influenced by the loop gain at f_p-f_s. The sideband effect cannot be ignored any more. When f_p approaches the switching frequency, f_p-f_s is at very low frequency and the magnitude of $T_{av}(f_p$-$f_s)$ is much higher than one and thus dominates the denominator. There is significant discrepancy between the loop gains from average model and from simulation result.

Because of the high gain of $T_{av}(f_p$-$f_s)$, there is a lower magnitude of T_v at f_p. In addition, the lower the f_p-f_s, normally the higher gain of $T_{av}(f_p$-$f_s)$, hence the lower magnitude of $T_v(f_p)$. Consequently, a dip around the switching frequency exists in the magnitude of the loop gain, T_v.

The phase information of T_v can also be obtained from (3.28). Typically, the phase of T_{av} is negative for a positive frequency. From (3.30), it is positive for a negative frequency. Existing in the denominator of (3.28), $T_{av}(f_p$-$f_s)$ leads to additional phase delays.

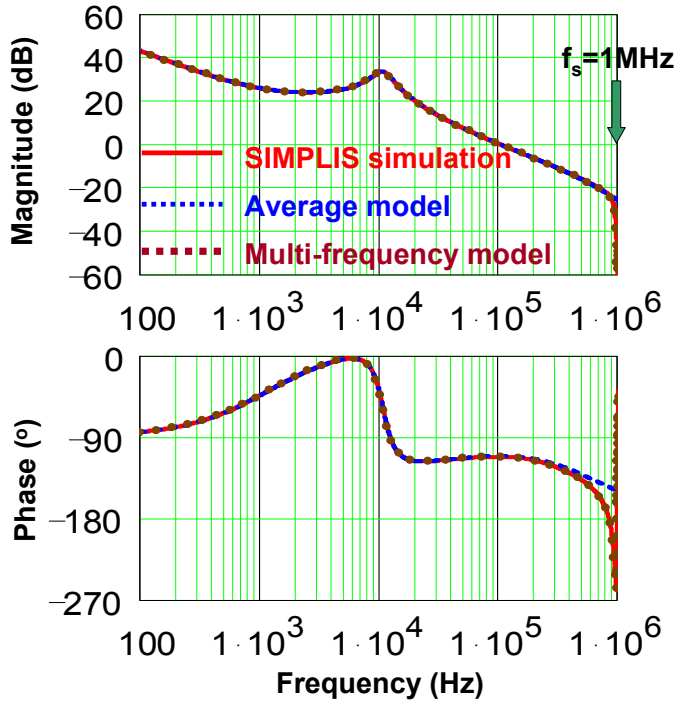

(a) The 100-kHz bandwidth design.

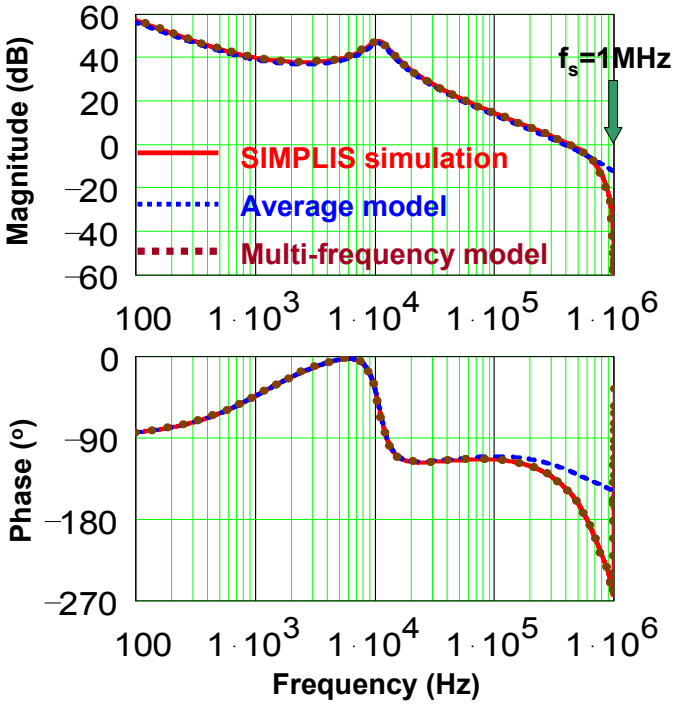

(b) The 400-kHz bandwidth design.

Figure 3.11. Loop gains of a 1-MHz buck converter with voltage-mode control. (Red solid line: SIMPLIS simulation result; Blue dashed line: average-model result; Brown dotted line: multi-frequency model result)

According to (3.28) and the previous analysis, the significance of the sideband effect is determined by the bandwidth of T_{av}. When the bandwidth of T_{av} is higher, there is wider frequency range where the influence from the sideband components is significant. Meanwhile, because higher bandwidth normally means higher magnitude for a certain frequency, there is more significant sideband effect.

For example, Figure 3.11 shows the loop gains in the SIMPLIS simulation, in the average model, and in the multi-frequency model with different bandwidths. The discrepancy between the average model and the multi-frequency model reflect the sideband effect. With a bandwidth of 100 kHz, the sideband effect has almost no influence inside the bandwidth. At half of the switching frequency, there is only a difference of 5^o. While for the case of 400-kHz bandwidth, there is about 25^o phase delay at the crossover frequency because of the sideband effect. At half of the switching frequency, the additional phase delay increases to 33^o.

In summary, phase delays are expected at the crossover frequency as the result of the sideband effect. Generally, the higher the control bandwidth, the larger impact on the phase margin from the sideband effect. Therefore, the sideband effect limits the possibility of high-bandwidth designs. For the stability analysis at these cases, it is necessary to use the proposed multi-frequency model instead of the conventional average model.

With (3.27), it is also possible to analyze V_o's response when there is output current perturbation. However, it is not enough to include only the component of $V_o(f_p)$. As discussed in Chapter 2, the sideband component should also be considered since it may be stronger than the perturbation-frequency component. Figure 3.6 also provides an approach to analyze the relationship between different frequency components of V_o's response.

3.3 Summary

For single-phase buck converters with voltage-mode control, the average model fails to predict the loop gain's excessive phase delay. To predict the performance at high frequency, a valid model should include the sideband effect.

In this chapter, the extended describing functions for the PWM comparators are first derived. With the Fourier analysis, the relationship between the sideband components and the perturbation-frequency components are obtained for the comparator's input and output. Based on the derived extended describing functions, the multi-frequency model is proposed. The system stability and transient performance depend on the loop gain that is affected by the sideband components.

By applying the derived results on the buck converters, the influence from the sideband effect is clarified. From the multi-frequency model, it is explained that the result from the sideband effect is the reduction of magnitude and phase response of the loop gain. The significance of the sideband effect is determined by the bandwidth of the loop gain of T_{av}. With a higher bandwidth, there are more magnitude and phase reductions. Therefore, the sideband effect poses limitations to push the bandwidth.

In summary, the sideband effect in the single-phase buck converter poses bandwidth limitations. With the models proposed in this chapter, the converter's performance can be predicted analytically.

Chapter 4. Analyses for Multiphase Buck Converters

4.1 Introduction

In the single-phase buck converters, the sideband component around the switching frequency generates the components at the perturbation frequency again at the PWM comparator's output. The result of this influence is that there is excessive phase delay in the loop gain when the frequency is approaching the switching frequency. Therefore, the feedback loop's bandwidth is limited with a certain switching frequency. It is necessary to push the switching frequency to achieve a higher bandwidth for better transient response.

In the VR applications, the multiphase buck converter proposed by VPEC/CPES, as shown in Figure 1.5, is the most widely used design [10][11][12][13]. From the output voltage point of view, the ripple frequency is effectively increased with the multiphase buck converter. It has been argued that the equivalent switching frequency for an *n*-phase buck converter is *n*-times that of each phase, so the control loop bandwidth can be increased with the multiphase buck converters. It has been demonstrated by the switching-model simulation results that the dip around the switching frequency in the loop gain of single-phase buck converters is increased to four times switching frequency with a 4-phase buck converter [23].

By far, most of the previous analysis is based on intuitions or simulation results. The influence from multiphase has not been investigated theoretically. In this chapter, the analysis for the single-phase buck converter is extended to analyze the multiphase case. First, the multi-frequency model is developed for the multiphase buck converters. The sideband effect in the voltage-mode-controlled multiphase buck converter is investigated using this model. The influence on the bandwidth limitation from the interleaving technique is discussed. After that, the practical concerns about unsymmetrical phases are analyzed. A design considering the output inductor tolerance is used as an example to elaborate the importance of the symmetry of the multiphase to the control-loop bandwidth.

4.2 The Multi-Frequency Model of Multiphase Buck Converters

Considering the control perturbation as in Figure 4.1, the extended describing function of the PWM comparators for the *m*-th phase of the *n*-phase converter can be derived using the same method as in Chapter 3. Figure 4.2 illustrates the waveforms of the trailing-edge modulators for a 2-phase buck converter with a control voltage perturbation.

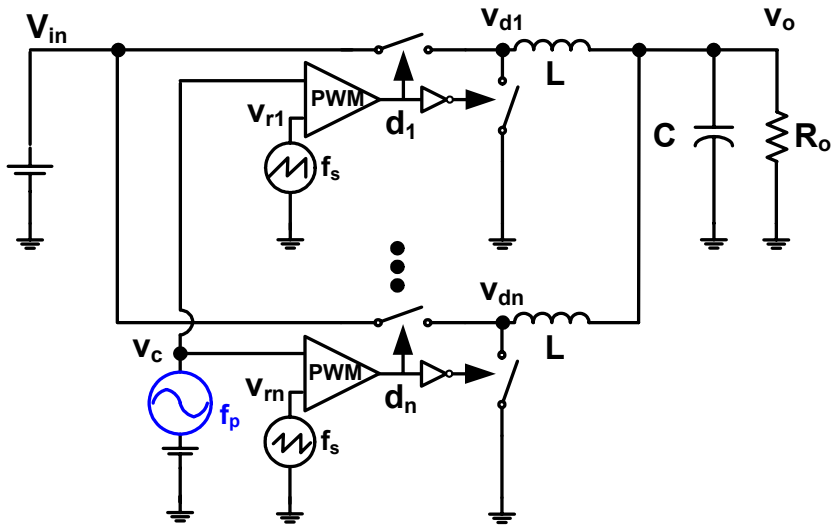

Figure 4.1. A multiphase buck converter with V_c perturbations.

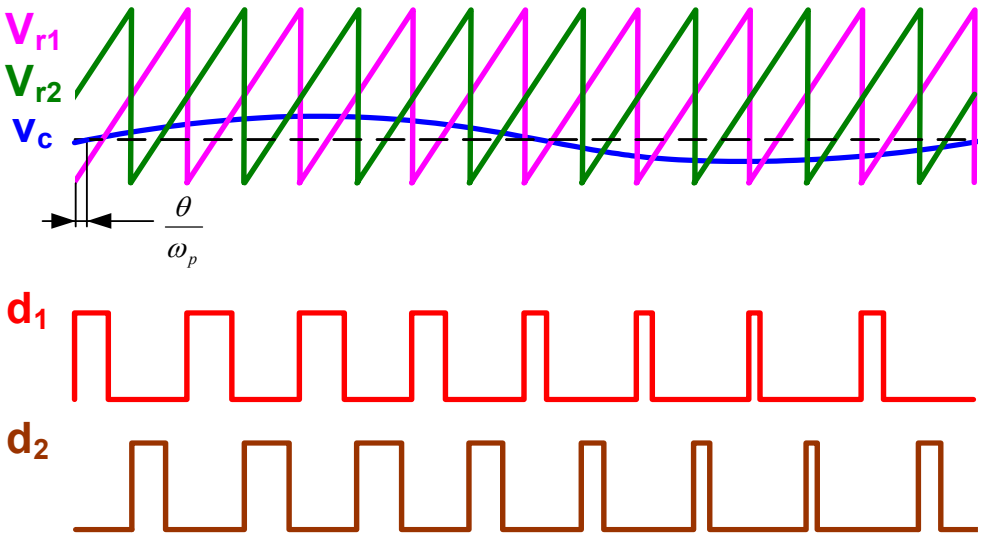

Figure 4.2. Trailing-edge modulator waveforms of a 2-phase buck converter with V_c perturbations.

With this modulation scheme, assuming $f_p/f_s=N/M$, and the sinusoidal control voltage of

$$v_c(t) = V_c + \hat{v}_c \sin(\omega_p t - \theta), \tag{4.1}$$

in a n-phase converter, the duty ratio of the m-th phase in the k-th cycle is

$$D_{k\_m} = \frac{V_c}{V_R} + \frac{\hat{v}_c \sin(\omega_p[(k-1)T_s + (m-1)T_s/n + DT_s + (D_{k\_m} - D)T_s] - \theta)}{V_R}. \tag{4.2}$$

Applying the small-signal approximation, it is simplified that

$$D_{k\_m} = D + \frac{\hat{v}_c}{V_R} \cdot \sin(\omega_p(k-1)T_s - \phi_m - \theta), \tag{4.3}$$

where

$$\phi_m = -\omega_p(D + (m-1)/n)T_s. \tag{4.4}$$

With the definition of the Fourier coefficient,

$$d_m(\omega_p) = \frac{1}{2\pi N} \sum_{k=1}^{M} \int_{(k-1)\omega_p T_s + \omega_p T_k + \frac{(m-1)T_s}{n}}^{(k-1)\omega_p T_s + \omega_p T_k + \frac{(m-1)T_s}{n}} e^{-j\omega_p t} d(\omega_p t). \tag{4.5}$$

It is obtained that when $\omega_p \neq k\omega_s/2$, k=1, 2, 3, …,

$$d_m(\omega_p) = \frac{\hat{v}_c e^{-j\theta}}{2jV_R}. \tag{4.6}$$

The describing function of the PWM comparator for the m-th phase is

$$F_{m\_m} = \frac{d_m(\omega_p)}{v_c(\omega_p)} = \frac{1}{V_R}. \tag{4.7}$$

Clearly, it does not change with the phase number,

Similarly, the coefficient at the frequency of ω_p-ω_s for the comparator's output can be derived that at $\omega_p \neq k\omega_s/2$, k=0, 1, 2, …

$$F_{m-\_m} = \frac{d_m(\omega_p - \omega_s)}{v_c(\omega_p)} = \frac{1}{V_R} \cdot \mathrm{e}^{jD2\pi} \cdot \mathrm{e}^{j(m-1)2\pi/n}, \tag{4.8}$$

and

$$F_{m+\_m} = \frac{d_m(\omega_p)}{v_c(\omega_p - \omega_s)} = \frac{1}{V_R} \cdot \mathrm{e}^{-jD2\pi} \cdot \mathrm{e}^{-j(m-1)2\pi/n}. \tag{4.9}$$

The derived extended describing functions for the trailing-edge PWM comparator of the *m*-th phase in an *n*-phase buck converter is summarized as in Table 4.1, when $\omega_p \neq k\omega_s/2$. Based on the derived equations, the multi-frequency model for the comparators is illustrated in Figure 4.3. For the same frequency components of the PWM comparator's input and output, their relationships are the same for the interleaved phases. However, for the relationship between the sideband components and the perturbation-frequency components, it includes additional information of number of phase.

Assuming a constant input voltage, the model for the open-loop *n*-phase buck with perturbation at the control voltage is shown in Figure 4.4, where G_{LC_m} is the transfer function from the *m*-th phase voltage to the output voltage. Therefore, the sideband component at the output voltage is

$$v_o(\omega_p - \omega_s) = \sum_{m=1}^{n} d_m(\omega_p - \omega_s) \cdot V_{in} \cdot G_{LC\_m}(\omega_p - \omega_s). \tag{4.10}$$

Table 4.1. Extended describing functions of the trailing-edge PWM comparator for the *m*-th phase in an *n*-phase buck converter.

		Output components	
		$d_m(\omega_p)$	$d_m(\omega_p - \omega_s)$
Input components	$v_{c\_m}(\omega_p)$	$F_{m\_m} = \frac{1}{V_R}$	$F_{m-\_m} = \frac{1}{V_R} \cdot \mathrm{e}^{jD2\pi}$
	$v_{c\_m}(\omega_p - \omega_s)$	$F_{m+\_m} = \frac{1}{V_R} \cdot \mathrm{e}^{-jD2\pi}$	$F_{m\_m} = \frac{1}{V_R}$

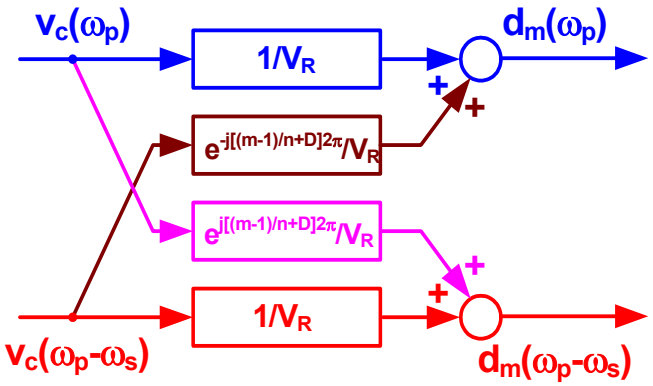

Figure 4.3. The multi-frequency model of the *m*-th phase in an *n*-phase PWM comparators.

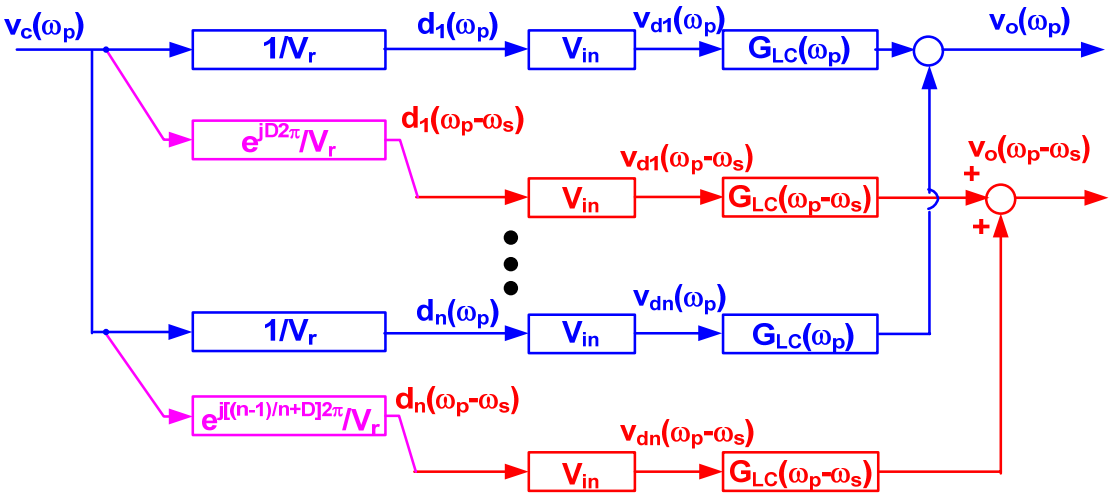

Figure 4.4. The multi-frequency model of the *n*-phase buck converter.

In the ideal cases, the transfer functions of the output filter for different phases are identical,

$$G_{LC\_1}(\omega) = G_{LC\_2}(\omega) = \cdots = G_{LC\_n}(\omega). \tag{4.11}$$

Assuming L_{eq} is the equivalent single-phase inductor,

$$L_{eq} = L_1 / n = L_2 / n = \ldots = L_n / n, \tag{4.12}$$

The transfer function for the output filter with L_{eq} and C is

$$G_{LC}(\omega) = G_{LC\_1}(\omega)/n = G_{LC\_2}(\omega)/n = \cdots = G_{LC\_n}(\omega)/n. \tag{4.13}$$

Combining (4.8), (4.10) and (4.13), it is obtained that when $\omega_p \neq k\omega_s/2$, k=0, 1, 2, …,

$$v_o(\omega_p - \omega_s) = \frac{G_{LC}(\omega_p - \omega_s)\cdot e^{jD2\pi}\cdot v_c(\omega_p)\cdot V_{in}}{n\cdot V_R}\cdot\sum_{m=1}^{n} e^{j(m-1)2\pi/n}. \quad (4.14)$$

If $n \neq 1$, it leads to

$$v_o(\omega_p - \omega_s) = 0, \quad (4.15)$$

which means that the sideband component at the output voltage is cancelled with the interleaved phases.

This phenomenon can be explained by the space-vector illustration of the duty cycles. For example, Figure 4.5 shows the case with a 3-phase buck converter. The perturbation-frequency components of the duty cycles are in phase, while their sideband component at ω_p-ω_s are evenly distributed in the space. Therefore, there exists the cancellation effect for the sideband components in the multiphase buck converters.

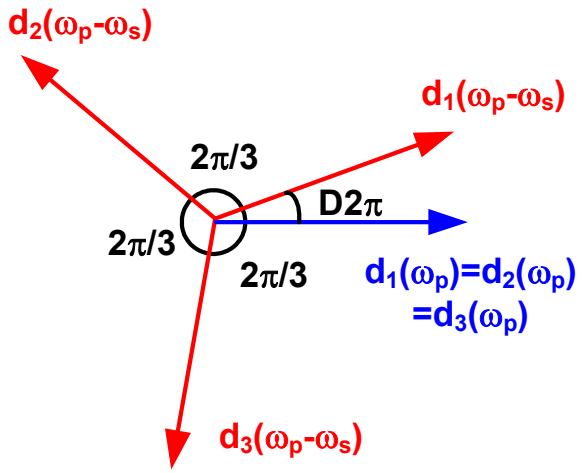

Figure 4.5. Space vectors of the duty cycles for the multiphase buck converters.

As proof, Figure 4.6 compares the output voltages between the single-phase and 2-phase open-loop buck converters with the same 5-mV sinusoidal control-voltage perturbation at 990-kHz with 1-MHz switching frequencies. In these two circuits, V_{in} is 12 V, V_o is 1.2 V, C is 1 mF, R_o is 80 mΩ, the peak-to-peak value of V_R is 1 V. The single-

phase converter's inductor value is 200 nH. The 2-phase converter's phase inductor value is 400 nH, which results in 200 nH equivalent inductance of the converter.

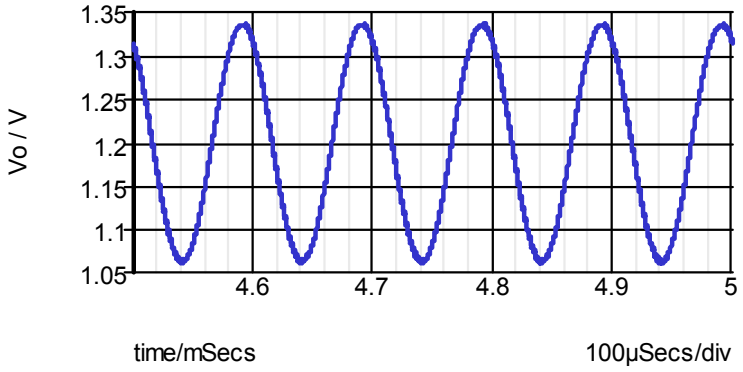

(a) V_o waveform in a single-phase buck.

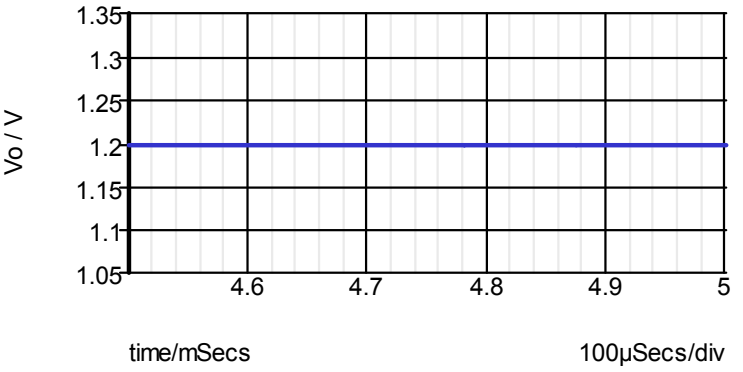

(b) V_o waveform in a 2-phase buck.

Figure 4.6. Simulated waveforms with 990-kHz V_c perturbation for 1-MHz open-loop buck converters.

In the single-phase case, there is a 136-mV 10-kHz sideband component at the output voltage. While in the 2-phase buck converter, the 10-kHz sideband component cannot be observed.

For a voltage-mode-controlled n-phase buck converter with load current perturbation as in Figure 4.7, the multi-frequency model is illustrated in Figure 4.8. For the same reason as in the open-loop case, if the phases are symmetrical, the interleaving among the phases cancels the f_p-f_s sideband component at V_o. Therefore, there is no f_p-f_s component at V_c. Consequently, there is no f_p component in the converter generated by the f_p-f_s component at

V_c. Ideally, the sideband effect existing in the single-phase buck is cancelled by the interleaving technique.

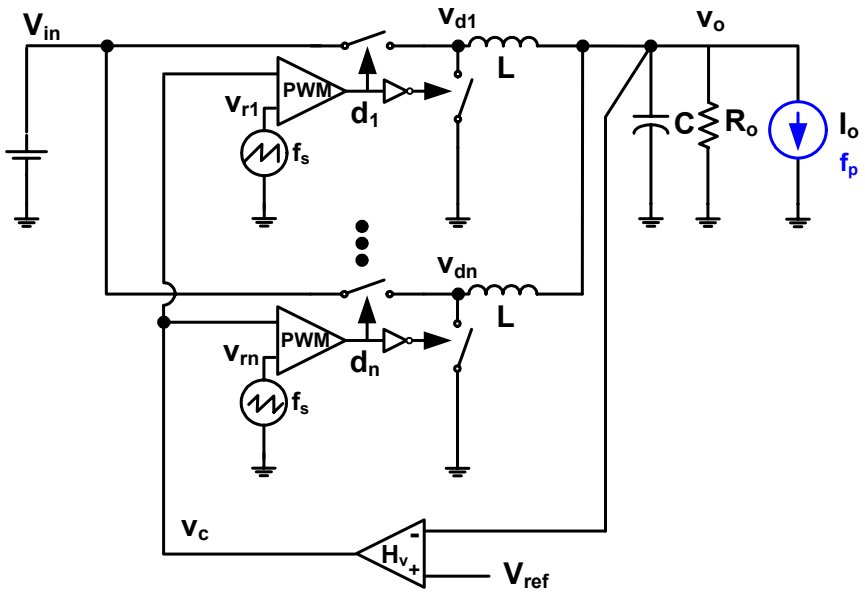

Figure 4.7. An *n*-phase buck converter with a load current perturbation.

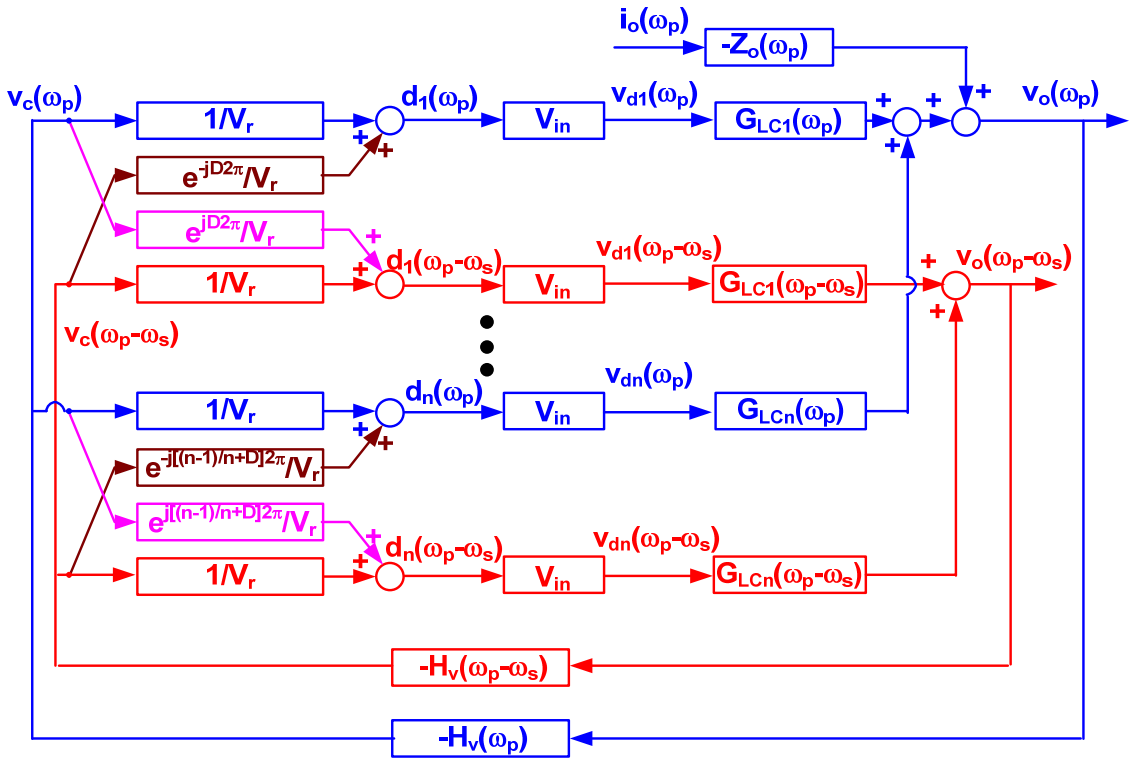

Figure 4.8. The multi-frequency model of the *n*-phase buck converter.

With Figure 4.8, the closed-loop impedance is derived as

$$Z_{o\_cl}(\omega_p) = -\frac{v_o(\omega_p)}{i_o(\omega_p)} = \frac{Z_o(\omega_p)}{1+T_v(\omega_p)}. \tag{4.16}$$

The loop gain

$$T_v(\omega_p) = T_{av}(\omega_p) = V_{in}/V_R \cdot H_v(\omega_p) \cdot G_{LC}(\omega_p) \tag{4.17}$$

is not influenced by the sideband components. This is because all the phases share the same control voltage f_p component.

Therefore, for the 2-phase simulated loop gain in Figure 4.9, the average model predicts much better than that in the single-phase case in Figure 3.9. There is no such excessive magnitude decrease and phase delays around the switching frequency as in the single-phase case.

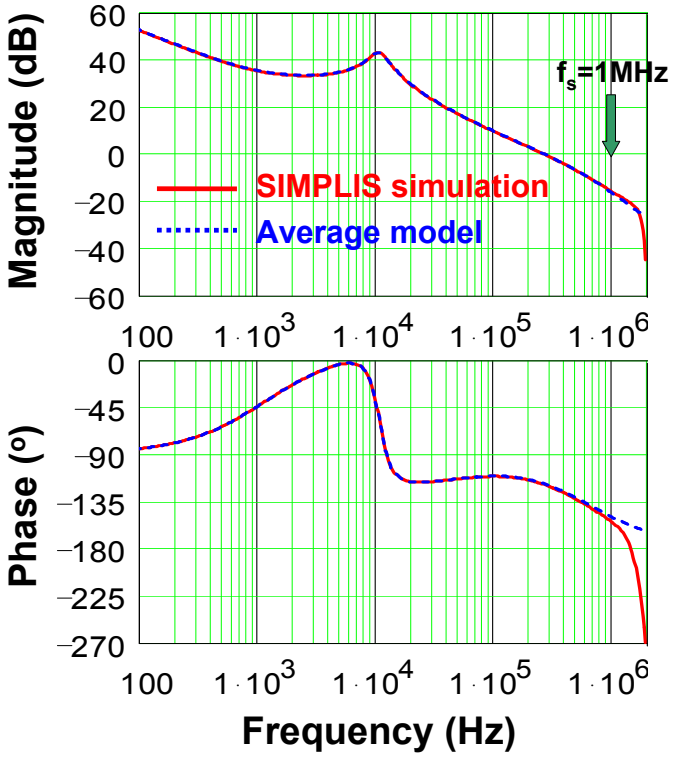

Figure 4.9. Loop gain of a 1-MHz 2-phase buck converter with voltage-mode control. (Red solid line: SIMPLIS simulation result; Blue dotted line: average-model result.)

However, there is similar phenomenon happening around twice of the switching frequency. The reason why there are still dips of magnitude and phase reductions can also be explained by the sampling feature of the PWM comparator, as shown in Figure 4.10. When the perturbation frequency f_p is higher than the switching frequency f_s, the component at $2f_s$-f_p, which is the sideband of $2f_s$, becomes lower than f_s. Therefore, it is no longer valid for the previous assumption that the sideband components around $2f_s$ can be ignored because of the low-pass filters in the circuit. This sideband component's influence cannot be neglected any more.

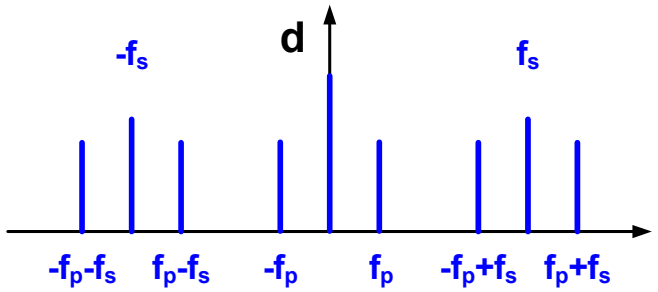

(a) f_p<f_s.

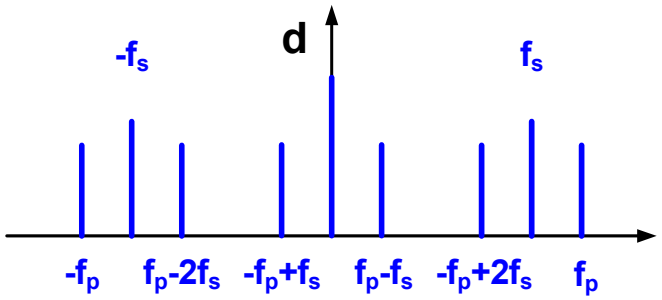

(b) f_s<f_p<$2f_s$.

Figure 4.10. Sideband components at the output of the PWM comparator.

As proof, Figure 4.11 shows the simulated output voltage with a 1.99-MHz perturbation with a 1-MHz open-loop 2-phase buck. With the setup in Figure 4.1 and a 5-mV perturbation, clearly, the 10-kHz component, which is at the sideband frequency of $2f_s$-f_p, is dominant.

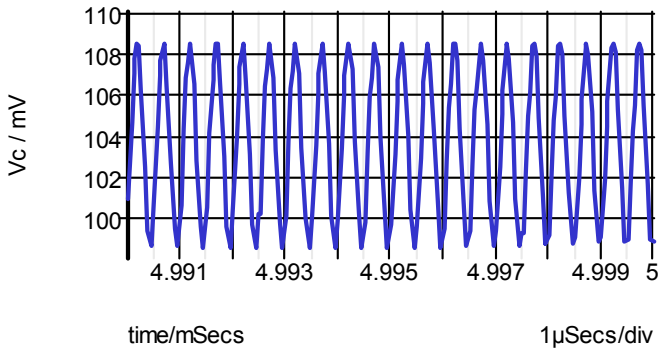

(a) V_c waveform.

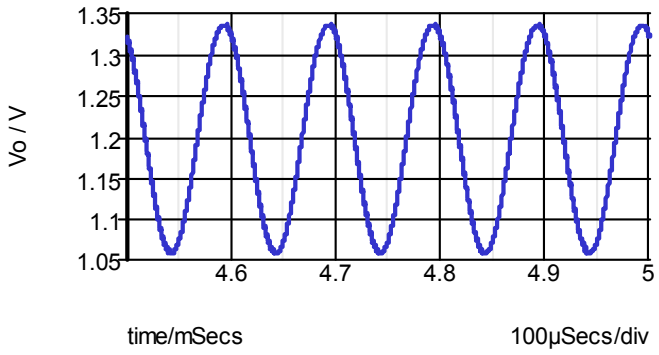

(b) V_o waveform.

Figure 4.11. Simulated waveforms with a 1.99-MHz V_c perturbation for a 1-MHz 2-phase open-loop buck converter.

For the higher-frequency analysis, the extended describing functions for the PWM comparator needs to include the higher-order sideband components. Similar approaches using the multi-frequency model can be applied. It is possible to extend the concept develop in the dissertation beyond the switching frequency.

Because of the cancellation of the sideband components at the output voltage in the interleaving buck converter, it is possible to push the bandwidth higher than the single-phase case. For example, with voltage-mode control, the bandwidth of the 2-phase buck converter can be pushed to 400 kHz with a 60^o phase margin, as shown in Figure 4.12. As the validation, Figure 4.13 shows the experimental loop gain.

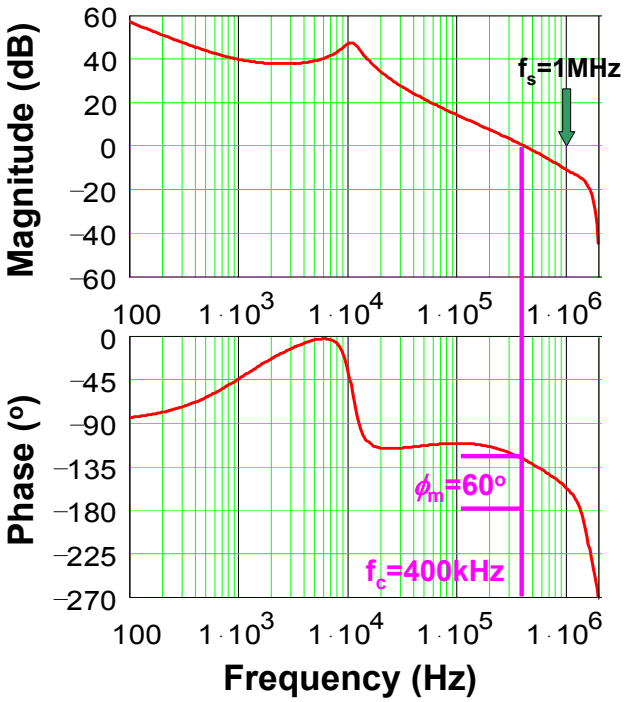

Figure 4.12. Simulated loop gain of a high-bandwidth 1-MHz 2-phase buck converter with voltage-mode control.

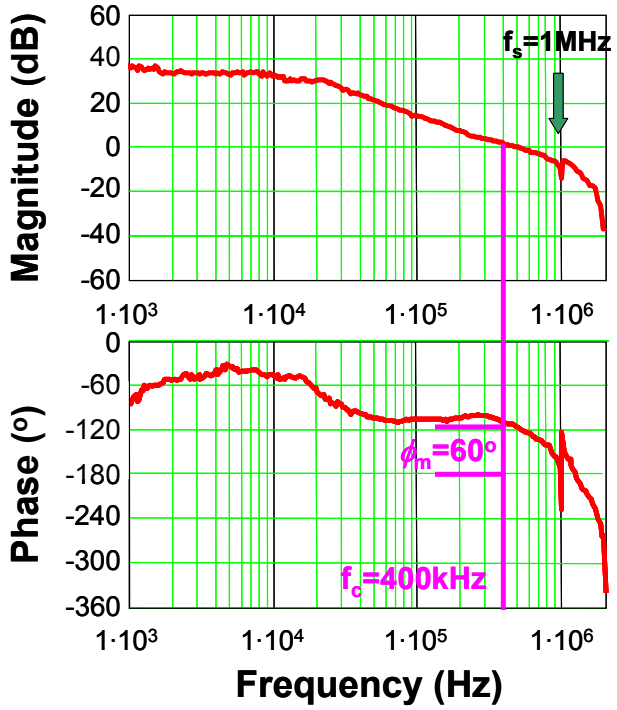

Figure 4.13. Experimental loop gain of a high-bandwidth 1-MHz 2-phase buck converter with voltage-mode control.

Although the simulation results shows there is no magnitude and phase reductions around the switching frequency, it appears in the measurement result, which means the bandwidth is still limited. The practical concern should be answered.

4.3 Study for the Multiphase Buck Converter with Unsymmetrical Phases

The previous analysis of the multiphase buck converters is based on ideal cases with symmetrical phases. However, in the measured loop gain as shown in Figure 4.13, there is still a dip of magnitude and phase reductions, which means that the sideband effect cannot be fully cancelled in practice. Since the cancellation determines how high the bandwidth can be pushed, it is necessary to investigate the influences from the asymmetry of the interleaved phases in the practical cases.

In the interleaving buck converters, the asymmetry of the phases might be a result of tolerances of inductor value, switch R_{dson} value, sawtooth ramp voltage value, phase shifting of the sawtooth ramp, driving delays, etc. In this section, an example is analyzed considering the inductor tolerance for the 2-phase case.

In the VR applications, the output inductors have tolerances as high as ±20% [47][48]. In Figure 4.7, the case of L_1=320nH and L_2=480nH is studied considering the rated value for the inductors is 400 nH. With open loop and a 5-mV 990-kHz control-voltage perturbation, the simulated output voltage waveform is shown in Figure 4.14.

Because of the unsymmetrical phases, there is 28-mV 10-kHz sideband component at V_o. Compare the case with interleaved symmetrical phases, the sideband components cannot be fully cancelled. On the other hand, it is smaller than the 136-mV 10-kHz V_o component in the single-phase case, therefore, there is partial cancellation of the sideband component with unsymmetrical phases.

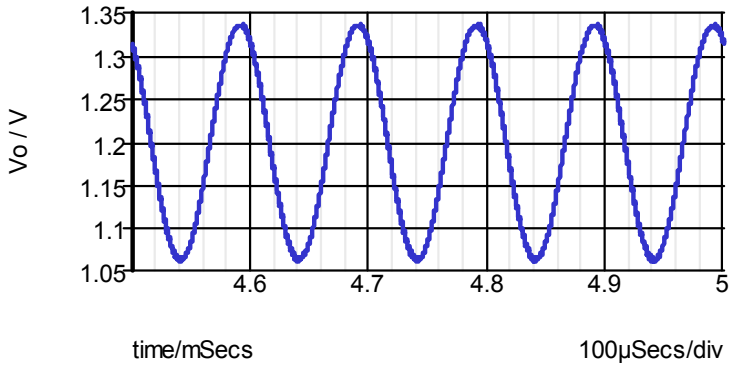

(a) Single-phase buck converter.

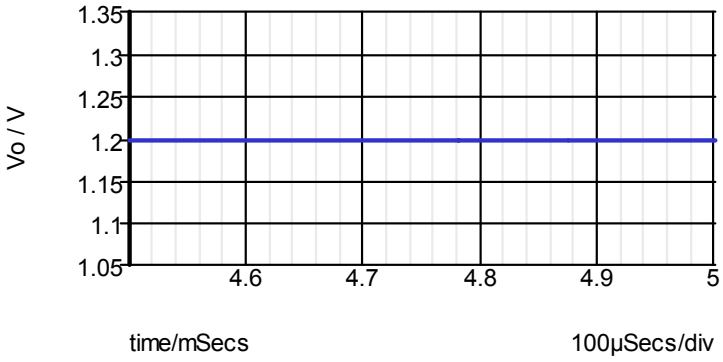

(b) 2-phase buck converter with symmetrical phases.

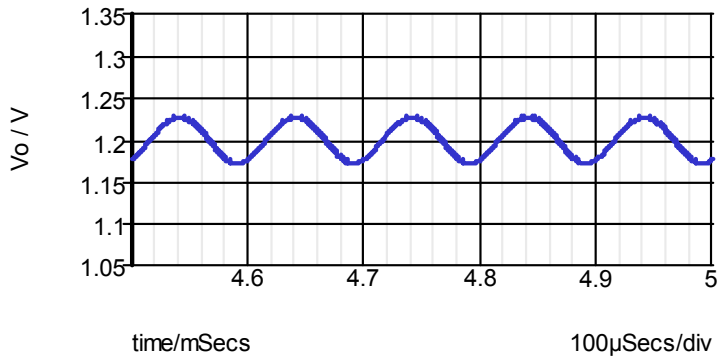

(c) 2-phase buck converter with ±20% inductor tolerance.

Figure 4.14. Simulated V_o waveforms with 990-kHz V_c perturbation for 1-MHz open-loop buck converters.

To analyze the phenomena quantitatively, the multi-frequency model shown in Figure 4.4 is applied. Since only the inductor tolerance is considered here, the describing functions of the PWM comparators are still valid with perfect phase shifting of the sawtooth ramp between the phases. Therefore, the ω_p-ω_s components at V_{d1} and V_{d2} have the same magnitude but opposite phases. However, the transfer functions of the power stage output filters are different for the two phases, which leads to certain ω_p-ω_s component at V_o.

For the first phase, the transfer function from the phase voltage to the output is

$$G_{LC1}(\omega) = \frac{C(\omega)//L_2(\omega)//R_o}{L_1(\omega) + C(\omega)//L_2(\omega)//R_o}, \tag{4.18}$$

where R_o is the load resistance, $C(\omega)$ is the impedance of the output capacitor, and $L_1(\omega)$ and $L_2(\omega)$ are the impedances for the first and second phase, respectively.

Similarly, for the second phase,

$$G_{LC2}(\omega) = \frac{C(\omega)//L_1(\omega)//R_o}{L_2(\omega) + C(\omega)//L_1(\omega)//R_o}. \tag{4.19}$$

With equivalent inductance of

$$L_{\text{eq}} = L_1 // L_2, \tag{4.20}$$

the effective transfer function for the two phases is

$$G_{LC}(\omega) = \frac{C(\omega)//R_o}{L_{eq}(\omega) + C(\omega)//R_o}. \tag{4.21}$$

It is obtained that

$$G_{LC1}(\omega) = \frac{L_2}{L_1 + L_2} \cdot G_{LC}(\omega), \tag{4.22}$$

and

$$G_{LC2}(\omega) = \frac{L_1}{L_1 + L_2} \cdot G_{LC}(\omega). \tag{4.23}$$

Because

$$\frac{v_o(\omega_p-\omega_s)}{v_c(\omega_p)} = e^{jD2\pi}\cdot\frac{V_{in}}{V_R}\cdot(G_{LC1}(\omega_p-\omega_s)-G_{LC2}(\omega_p-\omega_s)). \quad (4.24)$$

Considering (4.22), (4.23) and (4.24),

$$\frac{v_o(\omega_p-\omega_s)}{v_c(\omega_p)} = e^{jD2\pi}\cdot\frac{V_{in}}{V_R}\cdot\frac{L_2-L_1}{L_1+L_2}\cdot G_{LC}(\omega_p-\omega_s), \quad (4.25)$$

which means that the magnitude of the sideband component at output voltage is determined by the relative difference of the inductors. There is less cancellation of the sideband component at output when the tolerance for the inductors is larger.

The remaining sideband component at V_o can also be explained by the space vector representation as shown in Figure 4.15. Because of the difference at the LC filter of the power stage, the sideband components at V_o cannot be fully cancelled.

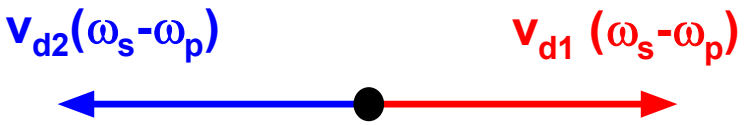

(a) Sideband components at phase voltage.

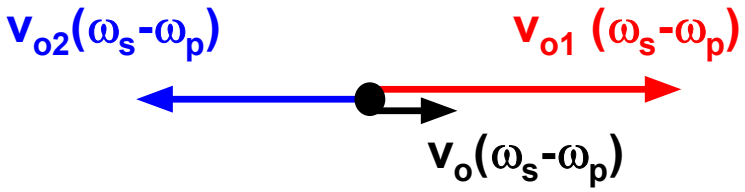

(b) Contributions from the unsymmetrical phases to the sideband components at output.

Figure 4.15. Space vector representations in the 2-phase buck converter with inductor tolerances.

Considering (4.25), the cancellation for the sideband effect is limited in the practical case with unsymmetrical inductors for the open-loop cases. For the closed-loop case, applying the model as in Figure 4.8, the loop gain is

$$T_v(\omega_p) = \frac{T_{av}(\omega_p)}{1+\frac{L_2-L_1}{L_2+L_1}\cdot T_{av}(\omega_p-\omega_s)} = \frac{V_{in}/V_R \cdot H_v(\omega_p)\cdot G_{LC}(\omega_p)}{1+\frac{L_2-L_1}{L_2+L_1}\cdot V_{in}/V_R \cdot H_v(\omega_p-\omega_s)\cdot G_{LC}(\omega_p-\omega_s)}. \quad (4.26)$$

Clearly, the sideband effect is not fully cancelled.

To investigate the influence from the remaining sideband effect, Figure 4.16 compares the loop gains with symmetrical phases and unsymmetrical phases with inductor tolerances.

In the 400-kHz bandwidth case with ±20% inductor tolerance, because the sideband cannot be fully canceled at f_p-f_s, it results in additional 8° phase delay at the crossover frequency compared with symmetrical phases. Besides, the phase response decreases rapidly after the crossover frequency. From this aspect, the remaining sideband effect's influence cannot be ignored in high-bandwidth designs.

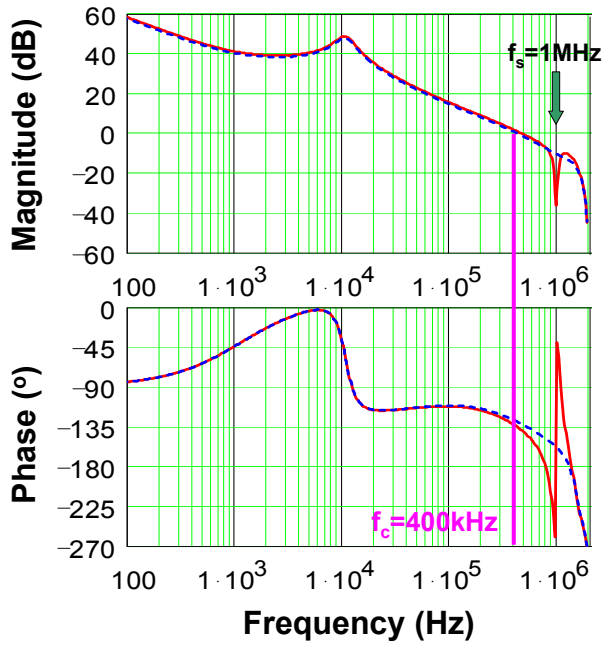

Figure 4.16. Simulated loop gain of 1-MHz 2-phase voltage-mode-controlled buck converters. (Red solid line: with identical inductors; Blue dashed line: with ±20% inductor tolerance.)

In this section, only the influence on the sideband effect from the tolerance of the phase inductors is discussed. If more components tolerances are considered, the same analyzing methodology can be used. When depending on the interleaving to cancel the sideband effect and to push the bandwidth, one should be extremely careful.

4.4 Summary

In this chapter, the extended describing functions for the PWM comparators are derived for the multiphase buck converters. By applying the obtained results, the sideband effect is possible to be cancelled with interleaved symmetrical phases. For unsymmetrical phases, a 2-phase converter with inductor tolerance is discussed as an example.

Intuitively, the multiphase buck converter increases the equivalent switching frequency. In this chapter, the influence from interleaving on the sideband effect is investigated. As the fundament of the multi-frequency mode, the extended describing functions for the PWM comparator for each phase are derived using the Fourier analysis. Based on ideal cases with symmetrical phases, the interleaving technique is possible to cancel the sideband components at the output voltage for the open-loop converter. Considering the perturbation frequency, f_p, is lower than the switching frequency, there is no lowest-frequency sideband component at f_s-f_p at output voltage. Consequently, with the voltage-mode control, there is no f_s-f_p sideband component at the input of the PWM comparator. In the effective loop gain, there is no influence from f_s-f_p component. Therefore, theoretically, there is no excessive phase delay in the loop gain as the result of sideband effect from f_s-f_p.

However, the above analysis assumes symmetrical phase with identical components and perfect interleaving. In practical designs, there is still magnitude and phase reductions around the switching frequency in the measured loop gain. To investigate this phenomenon, the components tolerances have to be considered. In this chapter, the example of a 2-phase buck converter with phase inductor tolerance of ±20% is studied. Using the multi-frequency model, it is clearly explained that the sideband effect cannot be fully cancelled in this case, which results in additional reduction of the phase margin. Therefore, one

should be extremely careful to push the bandwidth when depending on the interleaving to cancel the sideband effect.

In summary, the sideband effect is possible to be cancelled in the ideal multiphase buck converter with voltage-mode control. However, this cancellation is greatly depended on the components tolerances in the circuit. Therefore, the performance is still limited by the switching frequency.

Chapter 5. High-Bandwidth Designs of Multiphase Buck VRs with Current-Mode Control

5.1 Introduction

In the previous analysis, the buck and multiphase buck converter with voltage-mode control are investigated. The sideband effect that is a result of the feedback loop is also discussed. With symmetrical phases, the multiphase technique has the potential to cancel the sideband effect in the voltage loop, while the component tolerances in practical designs impact the cancellation.

To ensure the current sharing among the parallel phases, the current-mode control is widely used for the multiphase buck converters. By sharing the same reference for the peak value among phase currents, the peak-current mode control, as shown in Figure 5.1, can achieve current sharing without extra efforts. Therefore, it is one of the most widely used control methods in VR applications [49][50][51][52].

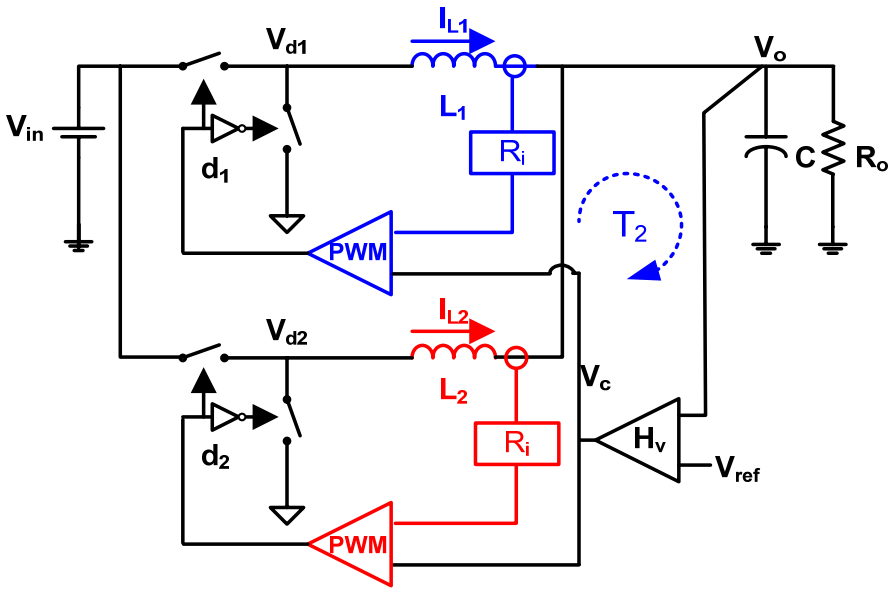

Figure 5.1. A 2-phase buck converter with peak-current control.

As discussed in Chapter 2, the sideband effect happens with voltage loop closed. If there is an additional current feedback loop in the converter, the sideband components of the inductor current influence the performance as well. In this chapter, the high-frequency performance with the current loop is studied.

For a 2-phase buck converter with peak-current control, the inductor current response is simulated with a switching model when the voltage-loop is open, as in Figure 5.2. Each phase's switching frequency is 1 MHz and the perturbation frequency is 990 kHz. As the waveforms shown in Figure 5.3, although the output voltage's sideband component at 10-kHz is cancelled, each phase's inductor current contains significant 10-kHz components.

With peak-current control, each phase's inductor current is fed back as the ramp of the PWM comparator. Consequently, there are significant sideband components at the input of each PWM comparator when the perturbation frequency is high.

When designing the voltage-loop compensator, the control-to-output-voltage transfer function, $G_{vc}(\omega)=v_o(\omega)/v_c(\omega)$, is critical to investigate the current loop's influence. As a result of the sideband effect in the current loop, there is a quick decrease of both the magnitude and the phase after half of the switching frequency, $f_s/2$, in the simulated transfer function, as shown in Figure 5.4. Compared with the transfer function of the single-phase buck converter, it has identical magnitude and phase responses.

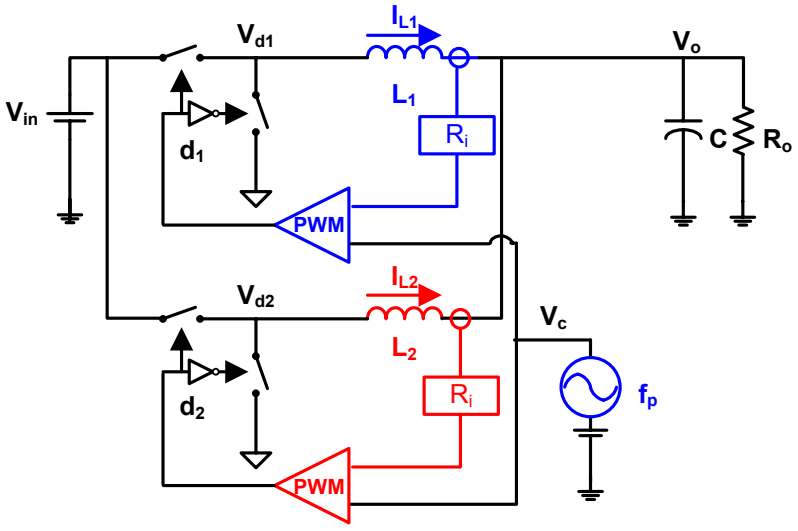

Figure 5.2. A peak-current-controlled 2-phase buck converter with V_c perturbations.

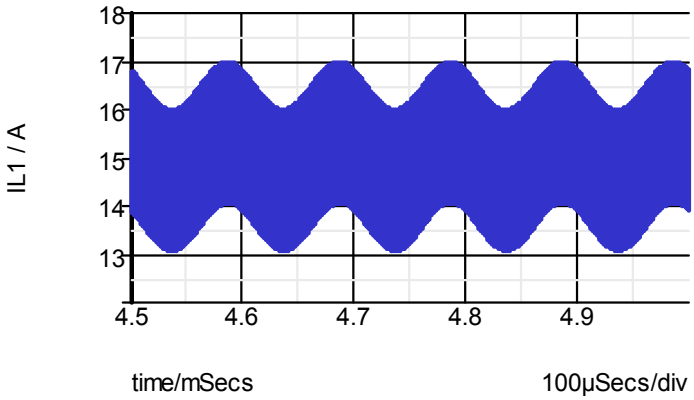

(a) First phase's inductor current, I_{L1}.

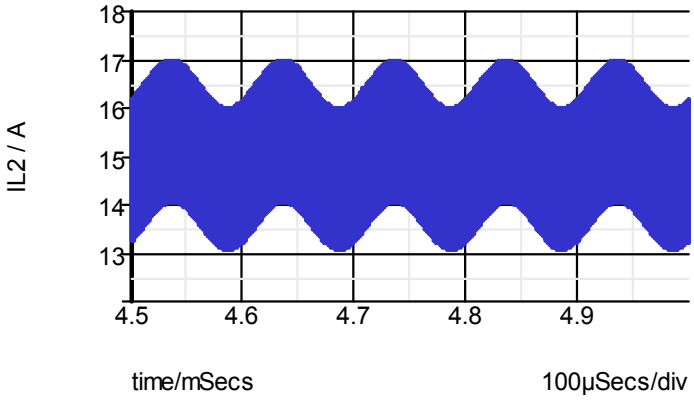

(b) Second phase's inductor current, I_{L2}.

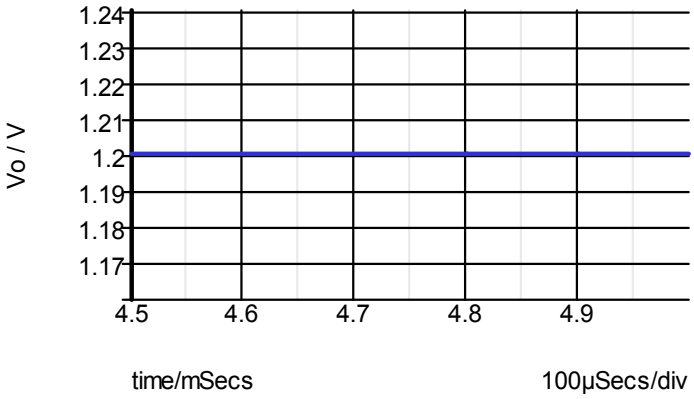

(c) Output voltage, V_o.

Figure 5.3. Simulated waveforms for the 1-MHz peak-current-controlled 2-phase buck converter with 990-kHz V_c perturbation.

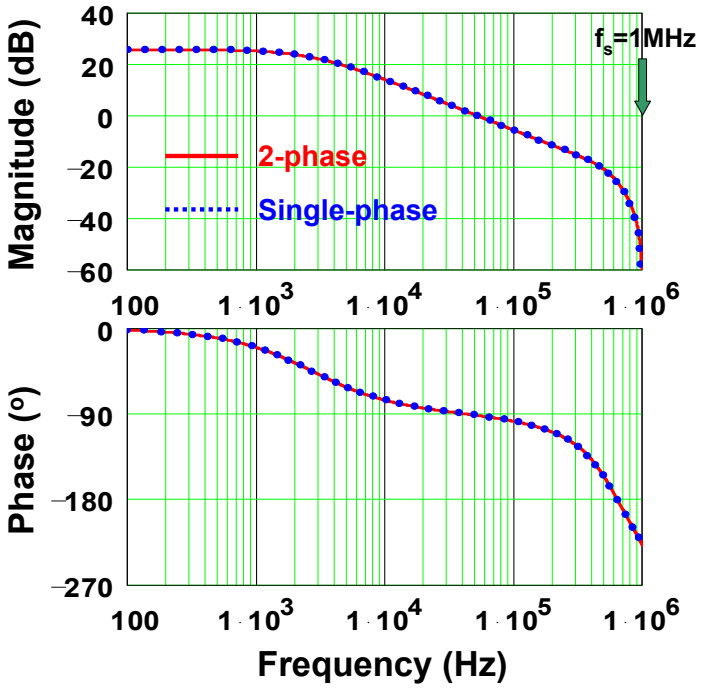

Figure 5.4. Simulated G_{vc} of 1-MHz buck converters with peak-current control.
(Red solid line: 2-phase buck; Blue dotted line: single-phase buck.)

Therefore, unlike the voltage-mode control, because the input of the PWM comparator contains sideband components even with interleaved phases, there are still dips of magnitude and phase reductions in the transfer function. Excessive phase delay is observed in the loop gain around the crossover frequency. As shown in Figure 5.5, there is only a 25° phase margin with the 350-kHz-bandwidth design for the 1-MHz 2-phase buck converter. While in the case of voltage-mode control as shown in Figure 5.6, a phase margin of 64° is obtained. Therefore, the sideband effect in the current loop results in worse designs with the current feedback.

To obtain an analytical explanation of the influence from the sideband components, it is expected to extend the multi-frequency model to the case of peak-current control. However, with additional input of the inductor current information, the model of the PWM comparator is much more complicated than that of the voltage-model control. Unlike the voltage-mode control, where there is a fixed PWM ramp, the peak-current control utilizes a variable ramp of the inductor current. Hence, the Fourier analysis based on the output waveforms should be improved, which is not a simple mission to accomplish. In this chapter, the analysis is mostly based on simulations and observations.

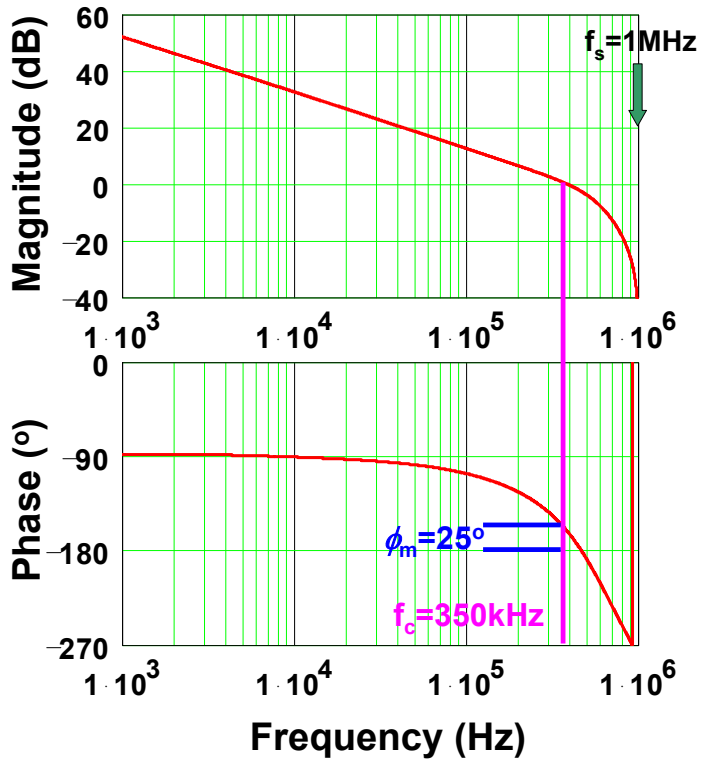

Figure 5.5. Loop gain, T_2, of the 1-MHz 2-phase buck converter with peak-current control.

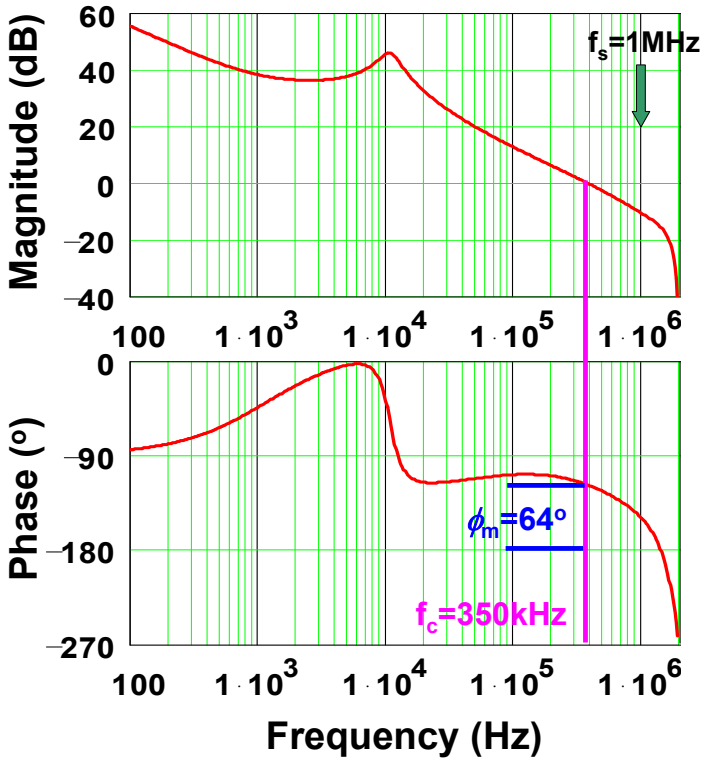

Figure 5.6. Loop gain, T_v, of the 1-MHz 2-phase buck converter with voltage-mode control.

In the next sections, several approaches are proposed to reduce the sideband effect in the current loop. Simulations and experiments are performed to verify the improvement.

5.2 Bandwidth Improvement with External Ramps

Figure 5.7 compares the PWM comparators in the voltage-mode control and the current-mode control. When there is a sinusoidal perturbation in the control voltage, there are different characteristics for the two modulators. The ramp in the voltage-mode PWM comparator is fixed, while the ramp in the peak-current control, which utilizes the sensed inductor current, I_L*R_i, is variable as a result of the current feedback loop.

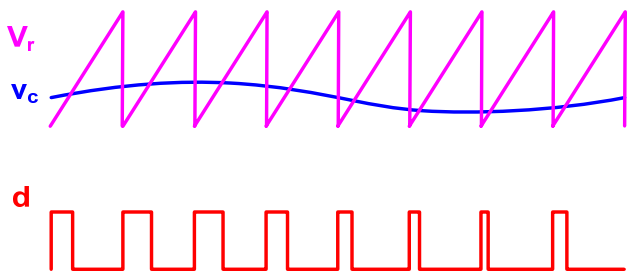

(a) Modulator in the voltage-model control.

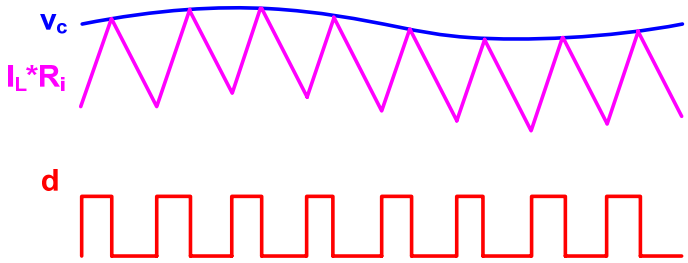

(b) Modulator in the current-model control.

Figure 5.7. Modulators in the voltage-mode control and current-mode control.

Because of the nonlinearity of the PWM comparator as shown in Figure 5.3, there are resulted sideband components in the inductor current. With peak-current control, and even with the voltage-loop open, there is sideband component at the input of the comparator, which leads to the magnitude and phase reduction around the switching frequency in the transfer functions. Hence, the loop gain is much worse in the peak-current control than in the voltage-mode control.

To improve the bandwidth for better voltage regulation, the sideband effect from the current loop should be attenuated. One solution is to introduce the fixed ramp, which actually involves adding the external ramp to the comparator, as shown in Figure 5.8.

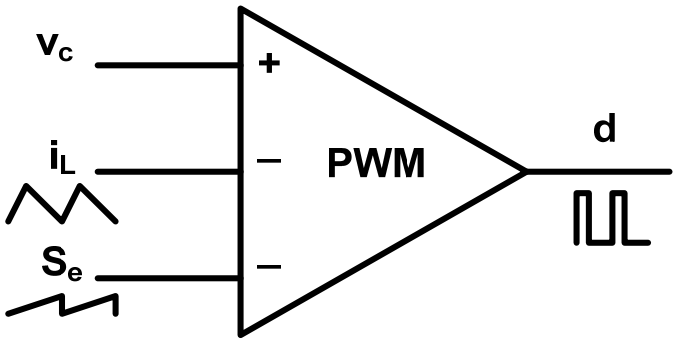

Figure 5.8. Modulator in peak-current control with external ramp.

With an external ramp, the characteristic of the PWM comparator is a compromise between the peak-current control and the voltage-mode control. By adjusting the relationship between the slope of the external ramp, S_e, and the slope of the sensed inductor current ramp, S_n, tradeoffs can be made among the two control approaches. With a larger external ramp, the system functions more like voltage-mode control, so that the bandwidth of T_2 can be increased higher.

As an example, Figure 5.9 demonstrates that a 350-kHz bandwidth and 60^o phase margin are achieved with S_e/S_n=5. Compare the design without any external ramp in Figure 5.5, the phase margin is improved significantly with the external ramps. Compared with the case with voltage-mode control in Figure 5.6, there is only minor difference between the phase margins, which verifies that adding external ramp is able to push the bandwidth.

It should be noted that the purpose of adding external ramp in this application is different from conventional designs using peak-current control, where the objective is to increase the system stability by reducing the possible sub-harmonic oscillation. Mathematically, the external ramp is selected to obtain a proper quality factor, Q, of G_{vc}'s double pole at $f_s/2$.

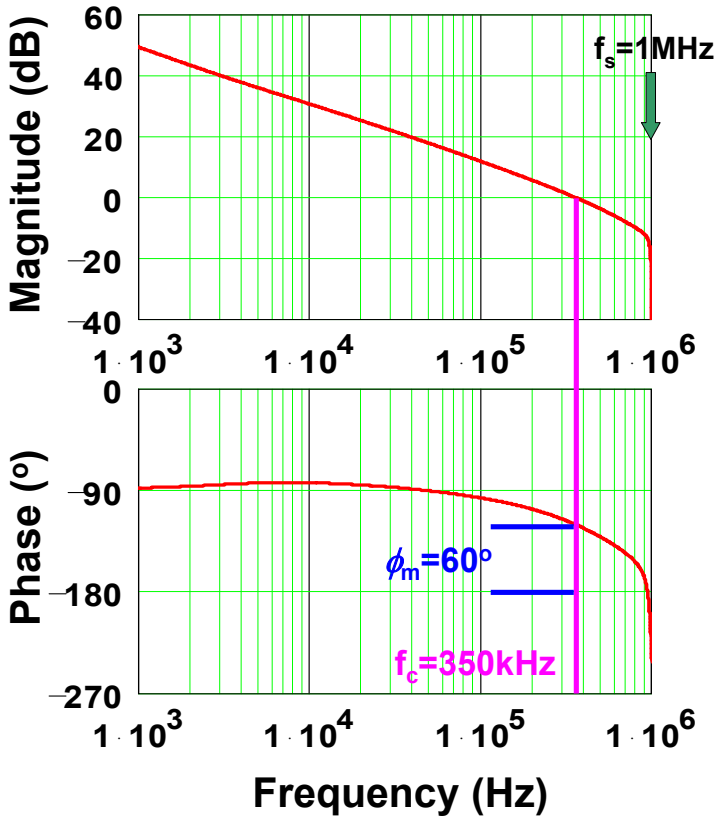

Figure 5.9. Loop gain, T_2, of the 1-MHz 2-phase buck converter with peak-current control, S_e/S_n=5.

In a typical design where the sub-harmonic oscillation is a concern, the external ramp is added so that the Q value is around one as a tradeoff between the stability and dynamic performance. Because

$$Q = \frac{1}{\pi(\frac{S_e + S_n}{S_n} \cdot (1-D) - 0.5)}, \tag{5.1}$$

with small duty cycles in the VR application, Q value is very low even without an external ramp. For example, a buck converter with 12-V input and 1.2-V output has Q of 0.8 when S_e=0. With a large external ramp, there is a very small Q. Figure 5.10 illustrates Q as a function of S_e/S_n. To achieve more benefit of reducing the influence of the sideband effect in the current loop, it is desired to add external ramps as more as possible. Hence, Q=1 is no longer a good practice for this application.

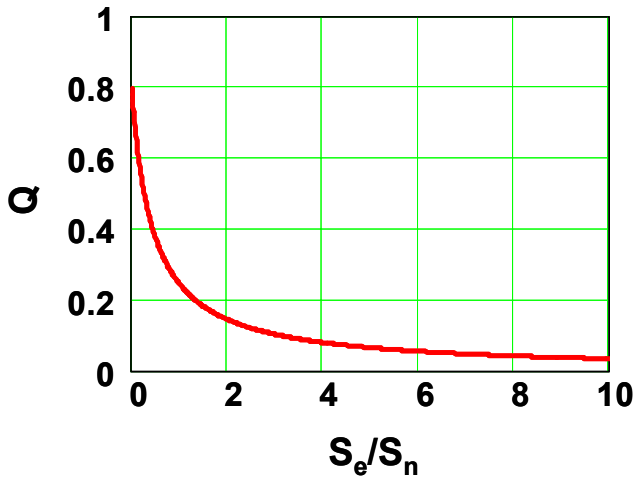

Figure 5.10. Q value of the $f_s/2$ double pole as a function of S_e/S_n for a 12-V-to-1.2-V buck converter.

However, if the external ramp overwhelms the inductor current information, the peak-current control becomes similar to the voltage-mode control. Under this circumstance, there is insignificant function on current sharing control among the phases. Therefore, one has to make the tradeoff between the current sharing performance and voltage regulation. This is related to another research topic being carried on in the VRM group in CPES and is not discussed here.

5.3 Bandwidth Improvement with Inductor Current Coupling

As shown in Figure 5.3, with interleaving technique, the sideband effect of f_p-f_s at V_o is cancelled because it includes the switching information for all the paralleled phases. In the current loop, the paralleled phases cannot use the total current information, because otherwise the current sharing cannot be achieved. Therefore, the sideband components appear in the current loop.

However, it is noticed that the inductor current sideband component is out of phase in Figure 5.3. Therefore, if part of other phases' current information is utilized in the current loop of one phase, certain cancellation of the sideband component in the current loop can be achieved, while current sharing is still maintained.

One possible implementation is coupling the phase currents through the feedback control, as show in Figure 5.11, where k is the coefficient reflecting the coupling between

the two phases. The other implementation is through the power stage by using the coupled-inductor structure, as in Figure 5.12 [53]. For symmetrical phases, the mutual inductance is

$$M = \alpha L_1 = \alpha L_2 . \tag{5.2}$$

where α is the coupling coefficient.

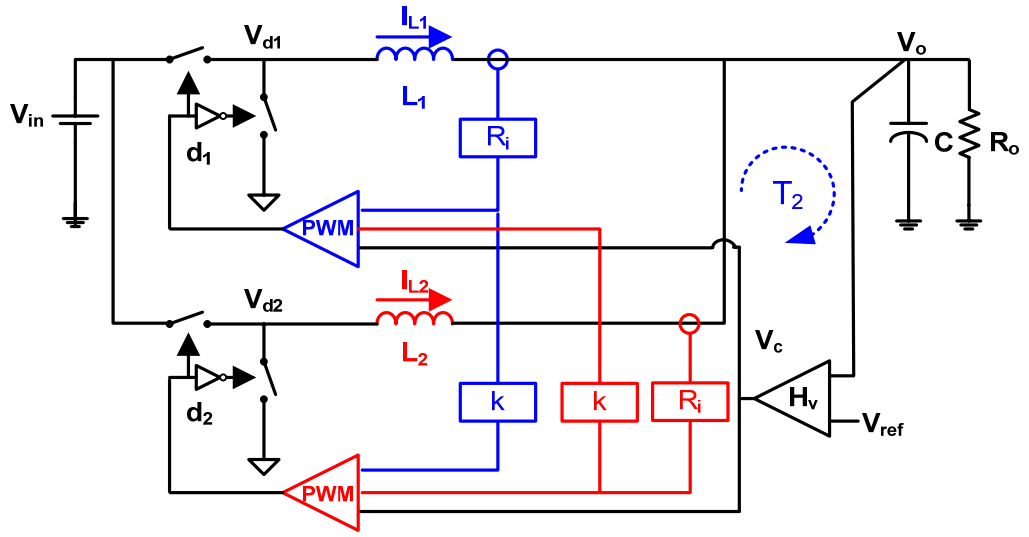

Figure 5.11. Phase-current-coupling control for a 2-phase buck converter.

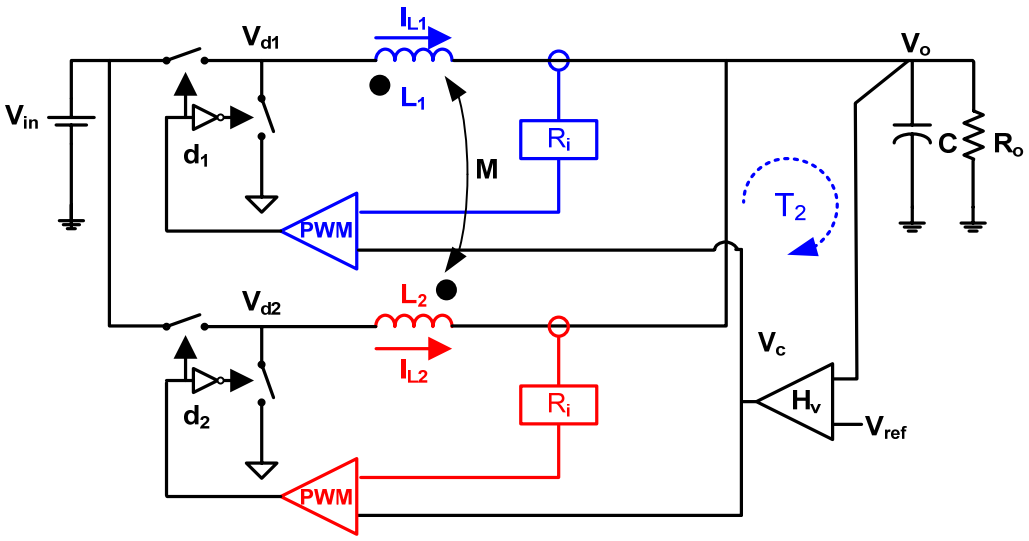

Figure 5.12. A 2-phase coupled-inductor buck converter.

With these two methods, the PWM ramp waveforms contain the components at twice the switching frequency. As an example, Figure 5.13 illustrates the inputs of the PWM

comparator for the two methods for $k=\alpha=0.5$ with the voltage-loop open. Clearly, the $2f_s$ information is introduced and the f_s information is reduced in each phase's current loop. The relationships between the f_s ripple and $2f_s$ ripple are identical for the two cases. The only difference is the magnitude of the ripples. Consequently, for the transfer function of G_{vc}, the two cases have identical phase response, as shown in Figure 5.14, and there is only a gain difference between their magnitude responses. Furthermore, with a stronger coupling, i.e. larger values of k or α, there is less phase delay at the high-frequency region.

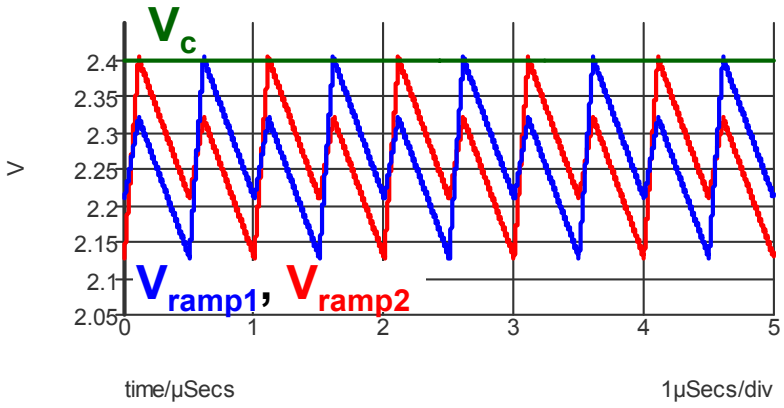

(a) Using phase-current-coupling control, k=0.5.

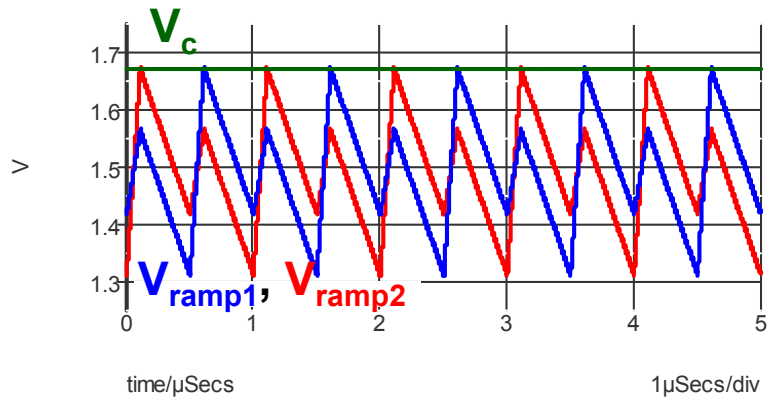

(b) Using coupled-inductor structure, α=0.5.

Figure 5.13. Waveforms of the PWM comparator inputs with inductor current information coupling for 2-phase buck converters.

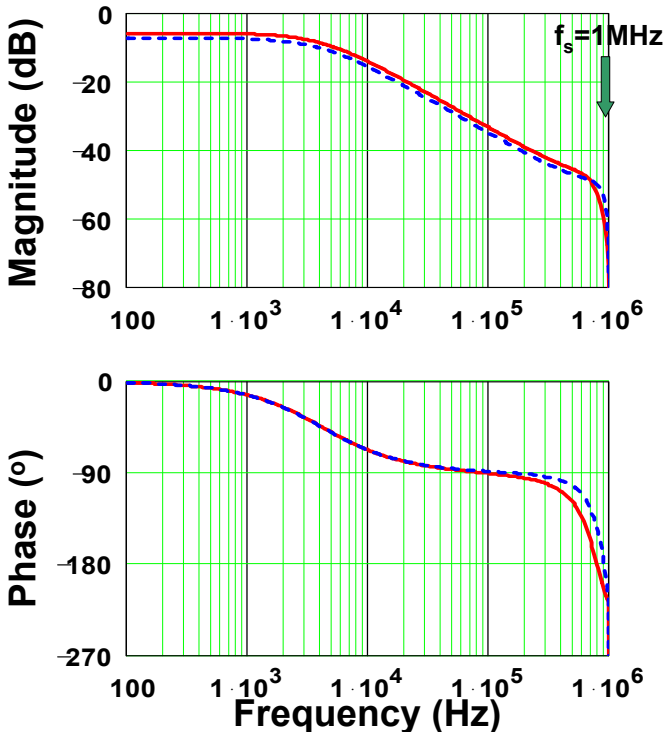

(a) Using phase-current-coupling control. (Red solid line: k=0.5; Blue dotted line: k=0.8).

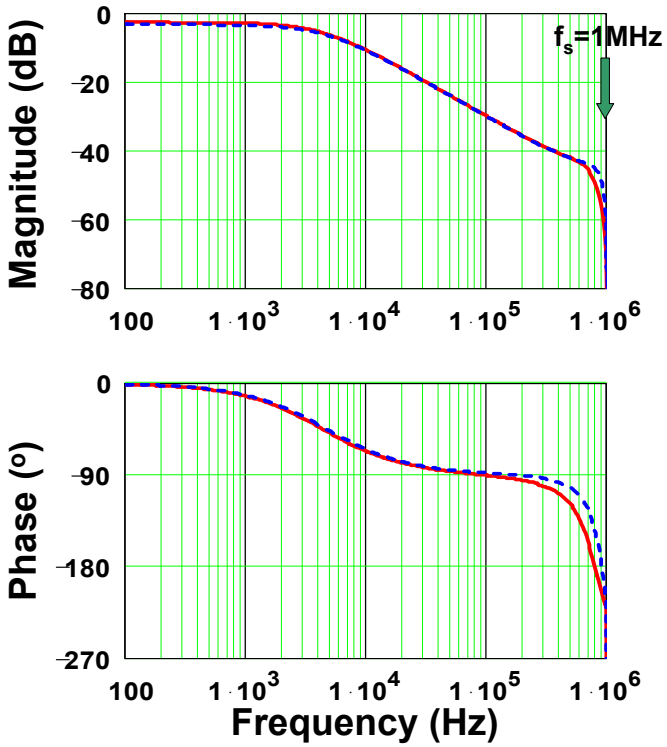

(b) Using coupled-inductor structure. (Red solid line: α=0.5; Blue dotted line: α=0.8).

Figure 5.14. Simulated G_{vc} with inductor current information coupling for 2-phase buck converters.

Comparing the two methods of coupling schemes, they have similar frequency-domain responses. From the power-stage aspect, the coupled-inductor design has additional advantages such as the smaller inductor current ripples [53], which leads to less switching loss and conduction loss in the converter. Therefore, the following discussion is based on coupled-inductor buck converters.

To investigate the influence from the coupling effect and thus to develop design guidelines for the phase-current-coupling control and the coupled-inductor structures, a small-signal model should be derived. Because the benefit of reducing phase delay is from cancelling the sideband components around the switching frequency, the model should be valid at high frequency. However, as mentioned above, it is not simple to extend the multi-frequency model to the peak-current control. From an equivalent circuit using center-tapped transformers, an approach similar to the sample-data model has been derived for the coupled inductor buck converter [54][55]. However, this model is not derived directly from the original topology, which makes it hard to understand the insight with coupled inductors. In addition, it is difficult to extend to cases with a phase number larger than two. In this section, the modeling for the coupled-inductor buck converter is improved.

For simplicity, a 2-phase case is studied first, which is shown in Figure 5.12. The self inductances of the two inductors' are L, and their mutual inductance is M. With current sensing gains of R_i, the input waveforms of the modulator is illustrated in Figure 5.15.

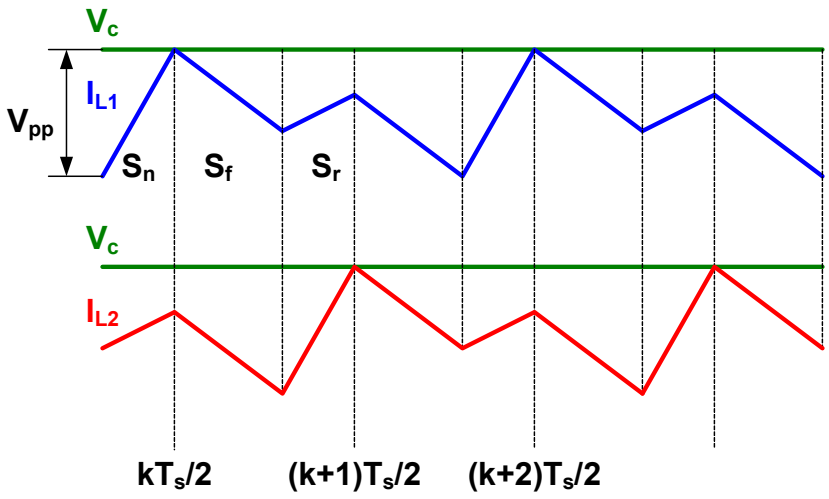

Figure 5.15. Input waveforms of the PWM comparators in a 2-phase coupled-inductor buck converter.

The slew rates of the sensed currents are

$$S_n = R_i \cdot \frac{V_{in} - V_o}{L_{eq1}}, \tag{5.3}$$

$$S_f = R_i \cdot \frac{V_o}{L_{eq2}}, \tag{5.4}$$

$$S_r = R_i \cdot \frac{-V_o}{L_{eq3}}, \tag{5.5}$$

where [53]

$$L_{eq1} = \frac{(1-\alpha^2)}{1-\alpha D/D'} \cdot L, \tag{5.6}$$

$$L_{eq2} = (1-\alpha) \cdot L, \tag{5.7}$$

$$L_{eq3} = \frac{(1-\alpha^2)}{1-\alpha D'/D} \cdot L. \tag{5.8}$$

D is the duty cycle and

$$D' = 1 - D. \tag{5.9}$$

In the derivation, it is assumed that with modifications of the sample-hold effect, H_e, and the PWM gain, F_m, the equivalent single-phase block diagram for the non-coupled buck converter, as shown in Figure 5.16, is still suitable for the coupling cases, while in the current loop, the coupling effect is included.

It is derived based on the PWM comparator's input waveforms in Figure 5.15, the gain of the comparator is

$$F_m = \frac{1}{S_n T_s}, \tag{5.10}$$

Same as the non-coupled case, the equivalent sensing gain

$$R_{ie} = R_i / 2. \tag{5.11}$$

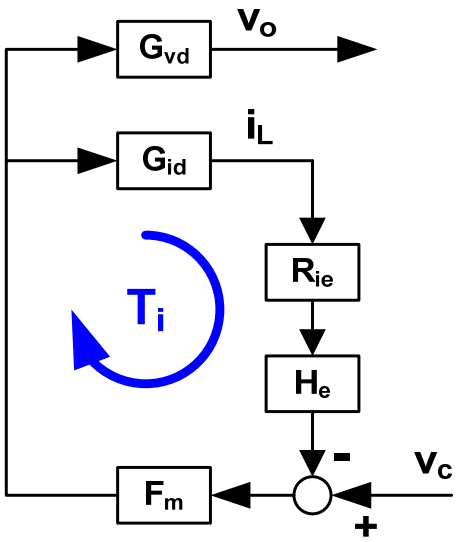

Figure 5.16. System block diagram of the coupled-inductor buck converter with voltage-loop open.

To calculate H_e, the natural response of one phase's current, the forced response from the other phases' currents perturbations and the control-voltage perturbation need to be derived and are derived.

The first phase's current, I_{L1}, with a small-signal variation at $kT_s/2$ is shown in Figure 5.17. The natural response for the next sampling instant at $(k+2)T_s/2$ is calculated as

$$\hat{i}_{L1}(k+2) = -\frac{S_f}{S_n} \cdot \hat{i}_{L1}(k). \tag{5.12}$$

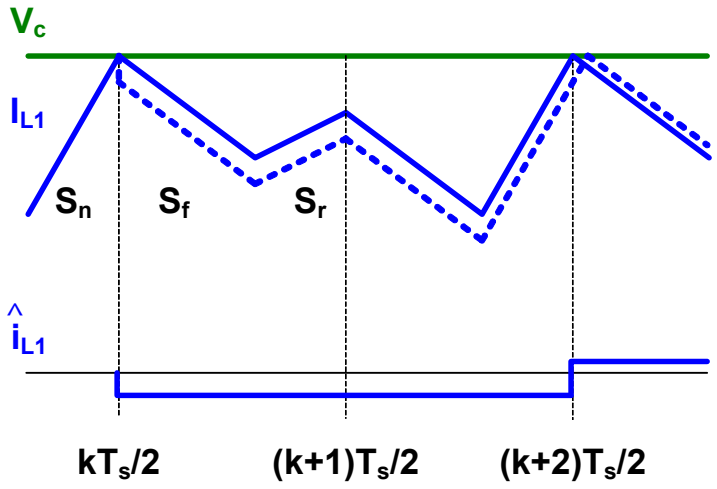

Figure 5.17. Natural response of the phase current, I_{L1}.

Meanwhile, because I_{L1}'s variation is a result of the duty cycle change, it leads to I_{L2}'s variation as well. From Figure 5.18, it can be derived that

$$\hat{i}_{L2}(k+1) = -\frac{S_r + S_f}{S_n} \cdot \hat{i}_{L1}(k) . \tag{5.13}$$

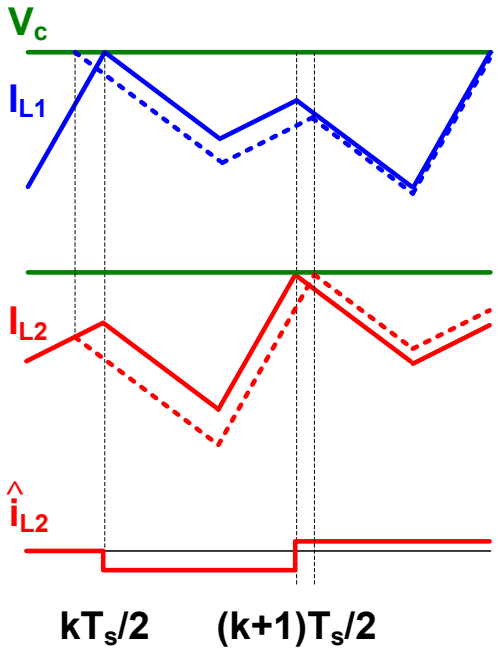

Figure 5.18. Forced response of I_{L2} as a result of I_{L1} variation.

Similarly,

$$\hat{i}_{L2}(k+3) = -\frac{S_f}{S_n} \cdot \hat{i}_{L2}(k+1) . \tag{5.14}$$

and

$$\hat{i}_{L1}(k+2) = -\frac{S_r + S_f}{S_n} \cdot \hat{i}_{L2}(k+1) . \tag{5.15}$$

Figure 5.19 illustrates the currents' response when there is the control-voltage perturbation.

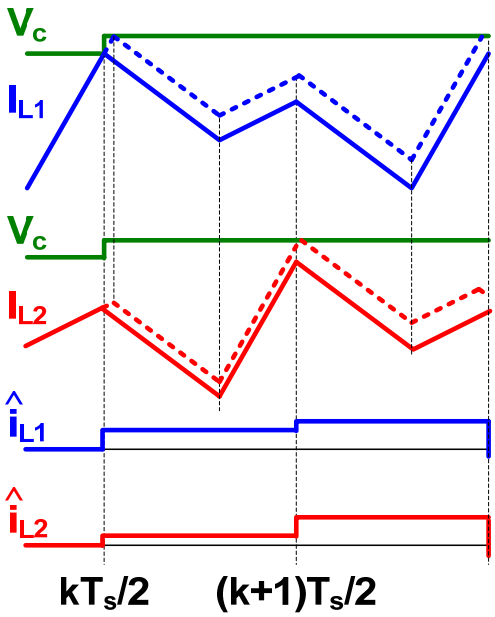

Figure 5.19. Forced responses of I_{L1} and I_{L2} as results of V_c variation.

It is derived that

$$\hat{i}_{L1}(k) = \frac{S_n + S_f}{S_n} \cdot \frac{1}{R_i} \cdot \hat{v}_c(k), \tag{5.16}$$

and

$$\hat{i}_{L2}(k) = \frac{S_r + S_f}{S_n} \cdot \frac{1}{R_i} \cdot \hat{v}_c(k), \tag{5.17}$$

Similarly, it is obtained that

$$\hat{i}_{L2}(k+1) = \frac{S_n + S_f}{S_n} \cdot \frac{1}{R_i} \cdot \hat{v}_c(k+1), \tag{5.18}$$

$$\hat{i}_{L1}(k+1) = \frac{S_r + S_f}{S_n} \cdot \frac{1}{R_i} \cdot \hat{v}_c(k+1), \tag{5.19}$$

Based on (5.3)~(5.8), the relationship between S_n, S_r, and S_f is expressed as

$$S_r + S_f = \alpha \cdot (S_n + S_f). \tag{5.20}$$

Therefore,

$$\hat{i}_{L1}(k+2) = \frac{1+\alpha}{2}\cdot\frac{S_n+S_f}{S_n}\cdot\frac{1}{R_i}\cdot\hat{v}_c(k+2)-\alpha\cdot\frac{S_n+S_f}{S_n}\cdot\hat{i}_{L2}(k+1)-\frac{S_f}{S_n}\cdot\hat{i}_{L1}(k). \tag{5.21}$$

The *z*-transform of (5.21) is given by

$$\hat{i}_{L1}(z) = \frac{1+\alpha}{2}\cdot\frac{S_n+S_f}{S_n}\cdot\frac{1}{R_i}\cdot\hat{v}_c(z)-z^{-1}\cdot\alpha\cdot\frac{S_n+S_f}{S_n}\cdot\hat{i}_{L2}(z)-z^{-2}\cdot\frac{S_f}{S_n}\cdot\hat{i}_{L1}(z). \tag{5.22}$$

For symmetrical phases,

$$\hat{i}_{L1}(z)=\hat{i}_{L2}(z) \tag{5.23}$$

Therefore,

$$H(z)=\frac{\hat{i}_{L1}(z)}{\hat{v}_c(z)}=\frac{\hat{i}_{L2}(z)}{\hat{v}_c(z)}=\frac{\frac{1+\alpha}{2}\cdot\frac{S_n+S_f}{S_n}\cdot\frac{1}{R_i}}{1+z^{-1}\cdot\alpha\cdot\frac{S_n+S_f}{S_n}+z^{-2}\cdot\frac{S_f}{S_n}} \tag{5.24}$$

Transform to the *s*-domain, it is

$$\frac{\hat{i}_{L1}(s)}{\hat{v}_c(s)}=\frac{\frac{1+\alpha}{2}\cdot\frac{S_n+S_f}{S_n}}{e^{sT_s}+\alpha\cdot\frac{S_n+S_f}{S_n}\cdot e^{sT_s/2}+\frac{S_f}{S_n}}\cdot\frac{1}{R_i}\cdot\frac{e^{sT_s}-1}{sT_s} \tag{5.25}$$

On the other hand, from Figure 5.16, the transfer function is derived as

$$\frac{\hat{i}_{L1}(s)}{\hat{v}_c(s)}=\frac{F_m F_i}{1+F_m F_i R_{ie} H_e}. \tag{5.26}$$

Since an equivalent single-phase buck converter model is used, the transfer functions in Figure 5.16 are using the equivalent inductor, whose value is equal to the paralleled two phases' transient inductance,

$$L_{eq} = \frac{L_{eq2}}{2} = \frac{(1-\alpha)L}{2}. \tag{5.27}$$

Assuming constant input and output voltage,

$$F_i = \frac{\hat{i}_{L1}(s) + \hat{i}_{L2}(s)}{\hat{d}(s)} = 2 \cdot \frac{V_{in}}{sL_{eq2}} = 2 \cdot \frac{1+\alpha}{sR_i}(S_n + S_f). \tag{5.28}$$

Combining (5.10), (5.20), (5.25), (5.26), and (5.28), it is obtained that

$$H_e(s) = \frac{(1-\alpha) \cdot \frac{sT_s}{e^{sT_s}-1} + 2\alpha \cdot \frac{sT_s/2}{e^{sT_s/2}-1}}{1+\alpha}. \tag{5.29}$$

To prove the derived model, Figure 5.20 compares the simulated and calculated G_{vc} transfer functions for a 2-phase coupled-inductor buck converter. For both the coupling coefficients of 0.5 and 0.8, the model predicts the performance very well up to the switching frequency.

Extending to an *n*-phase coupled-inductor buck converter, it is obtained using the same approach that

$$H_e(s) = \frac{(1-(n-1)\alpha) \cdot \frac{sT_s}{e^{sT_s}-1} + n\alpha \cdot \frac{sT_s/n}{e^{sT_s/n}-1}}{1+\alpha}, \tag{5.30}$$

where α is the coupling coefficient between either two phases.

Mathematically, the sample-hold effect, H_e, can be used to represent the influence from the switching frequency. The reason for phase response improvement with coupled inductors can be clearly indicated in (5.29) and (5.30). With the 2-phase coupled-inductor structure, the sample-hold effect at f_s is reduced when the $2f_s$ sampling is introduced. When there is no coupling, i.e. α=0, it is exactly the same as conventional buck converters. With a higher coupling coefficient, there is smaller sample-hold effect at f_s, while larger sample-hold effect at $f_s/2$.

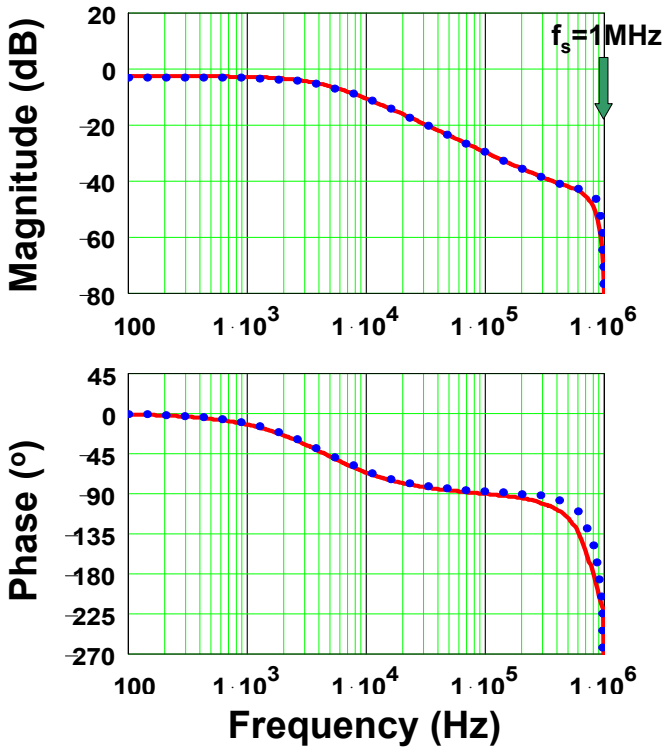

(a) SIMPLIS simulation result. (Red solid line: α=0.5; Blue dotted line: α=0.8)

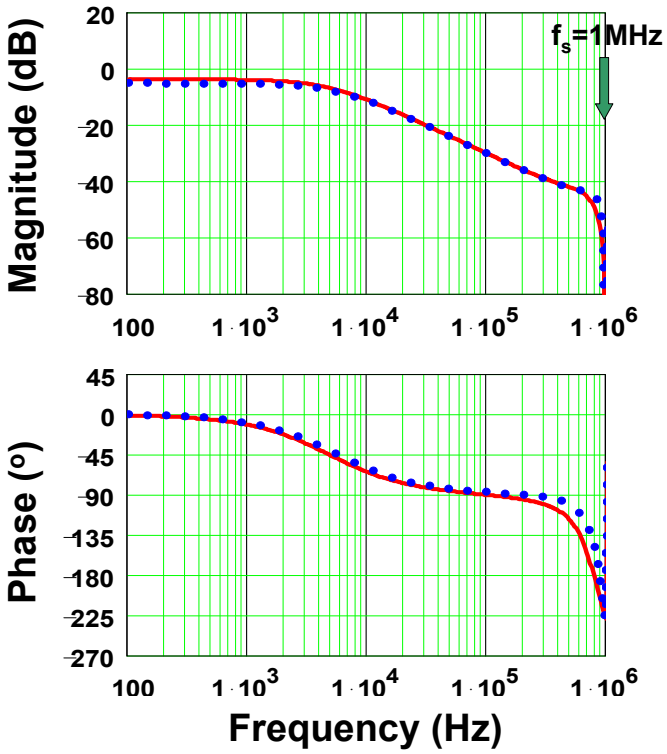

(b) Modeling result. (Red solid line: α=0.5; Blue dotted line: α=0.8)

Figure 5.20. G_{vc} transfer functions of a 2-phase coupled-inductor buck converter.

Figure 5.21 illustrates the influence of H_e with different coupling coefficient. For non-couple cases, the influence from H_e can be explained as a pair of right-half-plane (RHP) zeroes, which leads to magnitude increase and phase delays. With coupling introduced, there are less magnitude and phase delays near the switching frequency, which means the sample-hold effect at f_s is attenuated. Therefore, when the coupling coefficient is high enough, it is possible to push the bandwidth higher.

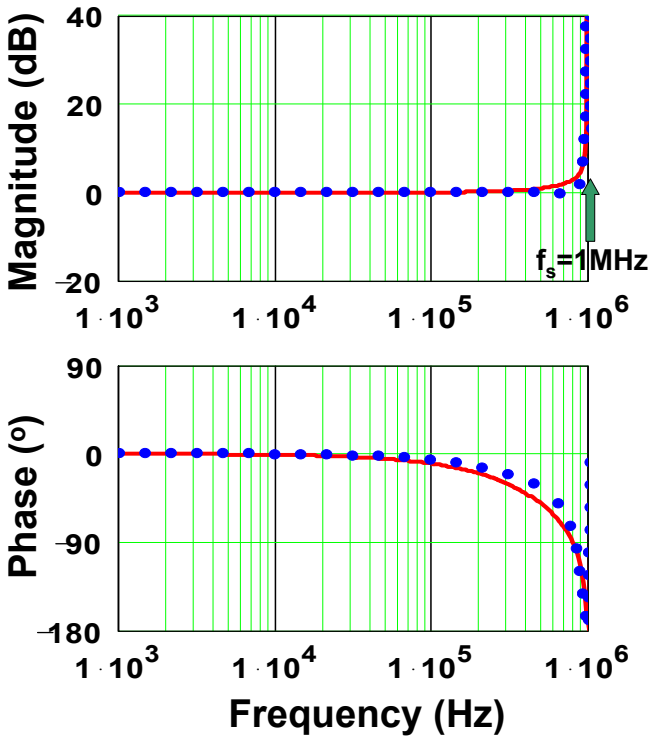

Figure 5.21. Sample-hold effect in the coupled-inductor buck converters.
(Red solid line: α=0; Blue dashed line: α=0.5; Brown dotted line: α=0.8)

As a design example, for a 1-MHz 2-phase coupled-buck converter with α=0.8, its T_2 loop gain achieves 350-kHz with 60° phase margin, as shown in Figure 5.22. To verify the analysis, a prototype of a 1-MHz 4-phase buck converter is built with coupled inductors. Because of the simple structure of coupling two phases, the circuit in Figure 5.23 is used, where the first and second phases have 180° phase shift with the 2-phase inductor coupling. The coupling coefficient is 0.8. The third and fourth phases are also coupled. Meanwhile, they have 90° phase shift from the first two phases. With this prototype, Figure 5.24 compares T_2 loop gain of the non-coupled case with the coupled case.

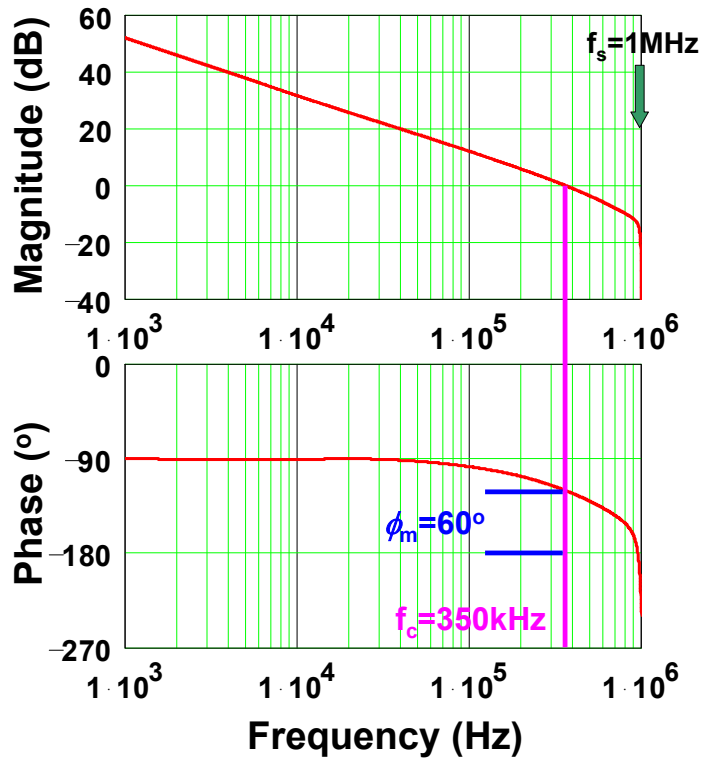

Figure 5.22. Simulated T_2 loop gain of a 2-phase coupled-inductor buck converter with α=0.8.

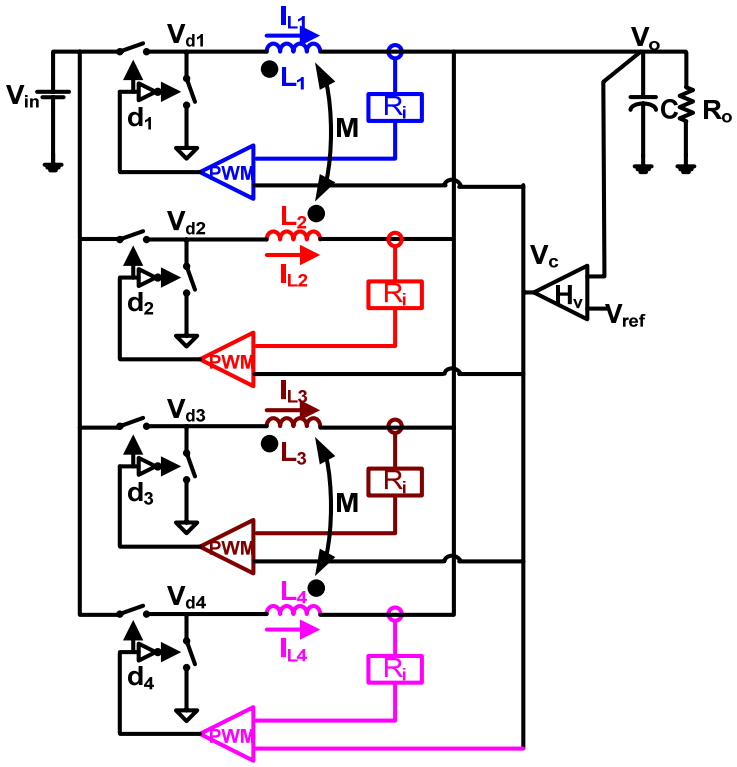

Figure 5.23. A 4-phase buck converter with 2-phase coupled-inductor design.

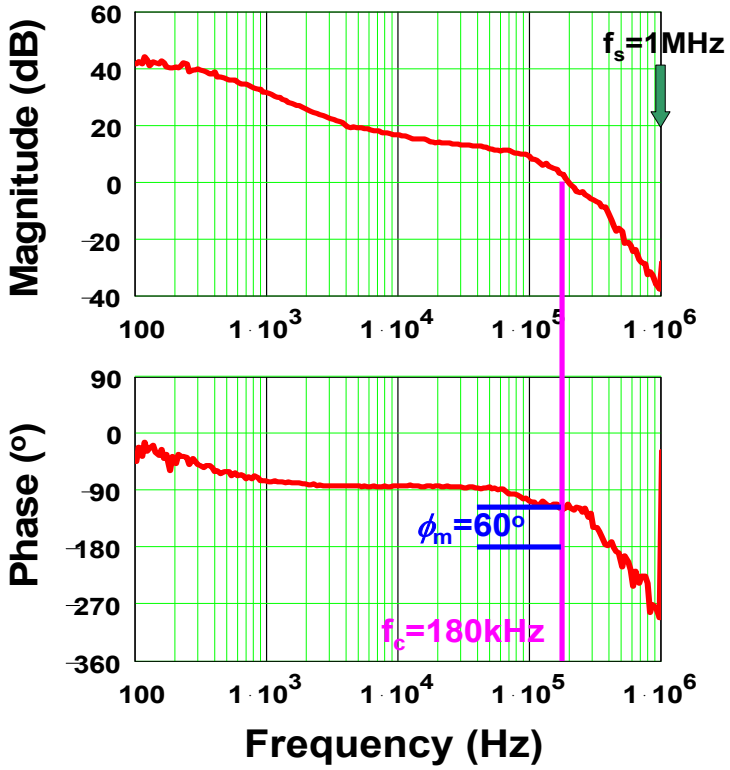

(a) Without coupling (α=0), f_c=180kHz.

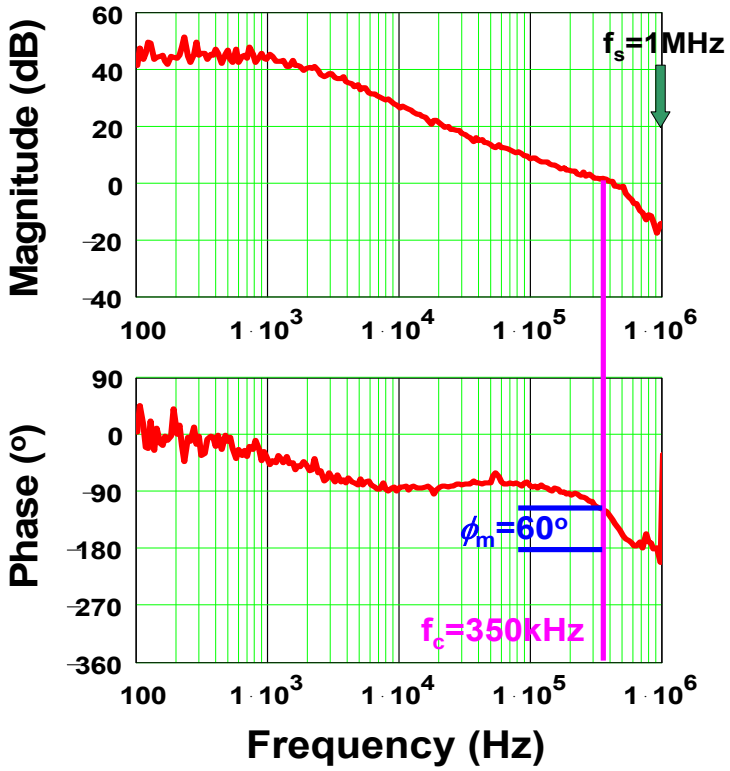

(b) With coupling (α=0.8), f_c=350kHz.

Figure 5.24. T_2's loop gain of a 1-MHz 4-phase buck converter with 2-phase coupling.

With coupled inductors, the bandwidth is pushed from 180 kHz, i.e. $f_s/6$, to 350 kHz, which is around $f_s/3$ with the same phase margin of 60^o. According to the previous analysis, the phase drop at f_s still exists in the coupled case because the sample-hold function at f_s cannot be totally eliminated.

5.4 Summary

In this chapter, the influence on the voltage regulation loop bandwidth from the peak-current control loop is studied. Because the inductor current is fed back for each phase, the sideband effect cannot be cancelled in the multiphase buck converters. Excessive magnitude and phase delays are observed in the loop gain.

To increase the bandwidth, the sideband effect in the current loop needs to be reduced. One solution is to weaken the current loop's influence with external ramps to the modulator. With a weak current loop, a faster voltage regulation loop can be achieved.

This chapter also studies another method of increasing the bandwidth by increasing the effective switching frequency with coupling the inductor current information, which can be realized either by coupling the phase current through feedback or using the coupled-inductor structure in the power stage. The derived sample-data model indicates that the f_s information is reduced with coupling. Consequently, the phase delay is decreased and the high-bandwidth design is obtained. To verify the analysis, a 1-MHz prototype is built and a bandwidth of 350 kHz is achieved with a 60^o phase margin.

Chapter 6. Conclusions

6.1 Summary

Future microprocessor poses many challenges to the VRs, such as the low voltage, high current, fast load transient, etc. In VR designs using multiphase buck converters, one of the results from these stringent challenges is a large amount of output capacitors, which is undesired from both the cost and the motherboard real estate aspects. In order to save the output capacitors, the control-loop bandwidth must be increased. However, the bandwidth is limited in the practical design. The influence from the switching frequency on the control-loop bandwidth has not been identified, and the influence from multiphase is not clear, either. Since the widely-used average model eliminates the inherent switching functions, it is not able to predict the converter's high-frequency performance. In this dissertation, the primary objectives are to develop the methodology of high-frequency modeling for the buck and multiphase buck converters, and to analyze their high-frequency characteristics.

First, the nonlinearity of the PWM scheme is identified. Because of the sampling characteristic, the sideband components are generated at the output of the PWM comparator. With the assumption that the low-pass filters in the converter well attenuate the sideband components, the conventional average model only includes the perturbation-frequency components. When studying the high-frequency performance, the lowest sideband frequency is not high enough as compared with the perturbation one; therefore, the assumption for the average model is not good any more. Under this condition, the converter response cannot be reflected by the average model. Furthermore, with a closed loop, the generated sideband components at the output voltage appear at the input of the PWM comparator, and then generate the perturbation frequency at the output, too. This causes the sideband effect to happen. The perturbation-frequency components and the sideband components are coupled through the comparator. To be able to predict the converter's high-frequency performance, it is necessary to have a model that reflects the sampling characteristic of the PWM comparator. As the basis of further research, the

existing high-frequency modeling approaches are reviewed. Among them, the harmonic balance approach predicts the high-frequency performance but it is too complicated to utilize. However, it is promising when simplified in the applications with buck and multiphase buck converters. Once the nonlinearity of the PWM comparator is identified, a simple model can be obtained because the rest of the converter system is a linear function.

With the Fourier analysis, the relationship between the sideband components and the perturbation-frequency components are derived for the trailing-edge PWM comparator. The concept of multi-frequency modeling is developed based on a single-phase voltage-mode-controlled buck converter. The system stability and transient performance depend on the loop gain that is affected by the sideband component. From the multi-frequency model, it is mathematically indicated that the result from the sideband effect is the reduction of magnitude and phase characteristics of the loop gain. With a higher bandwidth, there are more magnitude and phase reductions, which cause the sideband effect to pose limitations when pushing the bandwidth.

The proposed model is then applied to the multiphase buck converter. For voltage-mode control, the multiphase technique has the potential to cancel the sideband effect around the switching frequency. Therefore, theoretically the control-loop bandwidth can be pushed higher than the single-phase design. However, in practical designs, there is still magnitude and phase reductions around the switching frequency in the measured loop gain. Using the multi-frequency model, it is clearly pointed out that the sideband effect cannot be fully cancelled with unsymmetrical phases, which results additional reduction of the phase margin. Therefore, one should be extremely careful to push the bandwidth when depending on the interleaving to cancel the sideband effect.

The multiphase buck converter with peak-current control is also investigated. Because of the current loop in each individual phase, there is the sideband effect that cannot be canceled with the interleaving technique. For higher bandwidths and better transient performances, two schemes are presented to reduce the influence from the current loop: the external ramps are inserted in the modulators, and the inductor currents are coupled, either through feedback control or by the coupled-inductor structure. A bandwidth

around one-third of the switching frequency is achieved with the coupled-inductor buck converter, which makes it a promising circuit for the VR applications.

As a conclusion, the feedback loop results in the sideband effect, which limits the bandwidth and is not included in the average model. With the proposed multi-frequency model, the high-frequency performance for the buck and multiphase buck converters can be accurately predicted.

6.2 Future Works

Most of the research in this dissertation is based on voltage-mode control. The multi-frequency model, which clearly describes the influences from the sideband components, has not yet been derived for cases with current loops. The relationship between the multi-frequency model and the sample-data model has not been clarified. It could be interesting to extend the modeling work to current-mode control. Meanwhile, it has been proposed to reduce the influence from the current loop to increase the bandwidth, therefore, there is tradeoff between the current sharing and voltage regulation. This design tradeoff can be identified only when the model with current loop is obtained. This exploration could be another interesting research topic.

Appendix A. Analyses with Different PWM Schemes

For the discussions and analysis in this dissertation, the example of trailing-edge type of PWM comparator is used. The PWM comparator model has not been generalized for other kinds of modulation schemes, such as the leading-edge and double-edge modulations, as shown in Figure A.1. There has been interest in how the modulation schemes influences the control-loop bandwidth, especially for the double-edge modulation [56]. In this appendix, the extended describing functions for the PWM comparator with different modulation schemes are derived using the Fourier analysis. The modulation schemes' influences on the sideband effect and the control-loop bandwidth are compared. The high-frequency performances are explained using the multi-frequency model.

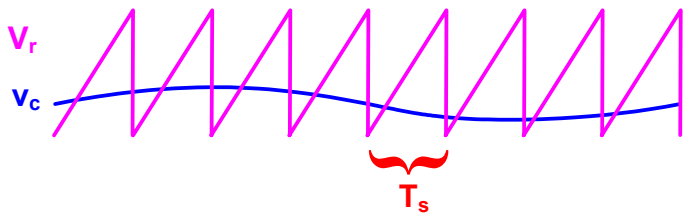

(a) Trailing-edge modulation.

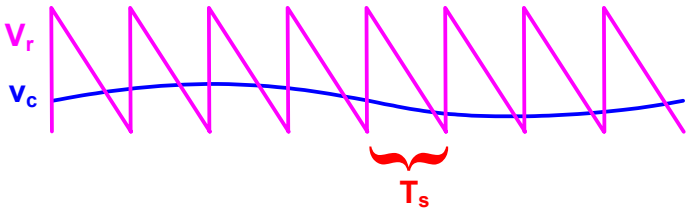

(b) Leading-edge modulation.

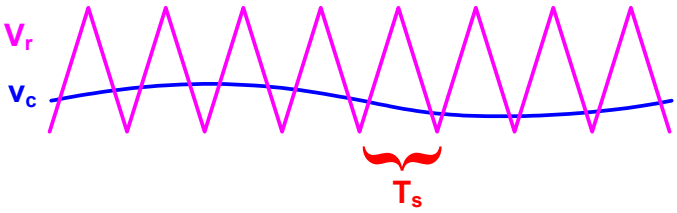

(c) Double-edge modulation.

Figure A.1. Input and output waveform of the PWM comparator with different modulation schemes.

The essence to include the sampling information in the high-frequency model is to model the PWM comparator. Generally, for constant-frequency controls, the input and output waveforms of the modulator are shown in Figure A.2. With different ratios between the rising time, T_r, and the falling time, T_f, the trailing-edge, leading-edge and double-edge modulations are realized.

In Figure A.2, with given perturbations, the Fourier analysis is performed on the waveforms of v_c and d, using the same approach as in Chapter 3. With calculated Fourier coefficients of the input and output waveforms, the function of the comparator can be obtained by comparing their coefficients at different frequencies.

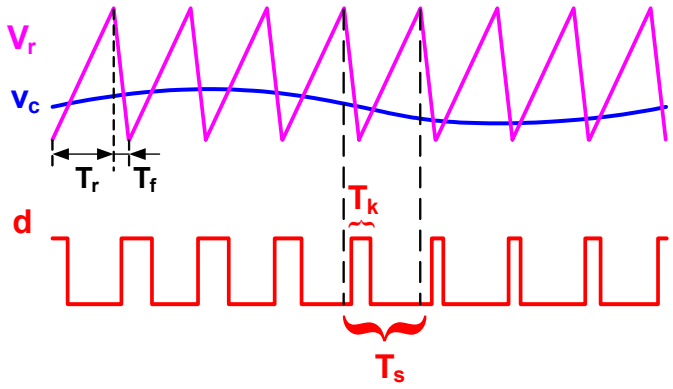

Figure A.2. Input and output waveforms of the PWM comparator of constant-frequency control.

With a ramp waveform as in Figure A.2 and the peak-to-peak value of V_R, for a control voltage of

$$v_c(t) = V_c + \hat{v}_c \sin(\omega_p t - \theta), \tag{A.1}$$

with small-signal approximations, the duty ratio for the k-th cycle is

$$\begin{aligned} \frac{T_k}{T_s} = D &+ \frac{T_f \cdot \hat{v}_c \sin(\omega_p[(k-1)T_s + T_f - DT_f] - \theta)}{T_s \cdot V_R} \\ &+ \frac{T_r \cdot \hat{v}_c \sin(\omega_p[(k-1)T_s + T_f + DT_r] - \theta)}{T_s \cdot V_R}, \end{aligned} \tag{A.2}$$

where $D=V_c/V_R$, is the DC duty cycle. After going through the similar process as in Chapter 3, the results listed in Table A.1 are obtained for $\omega_p \neq k\omega_s/2$, k=1, 2, 3, …

Table A.1. Extended describing functions of the PWM comparator with different modulations.

Describing Functions	Trailing-Edge PWM (T_f=0)	Leading-Edge PWM (T_r=0)	Double-Edge PWM (T_r=T_f)
$F_m = \frac{d(\omega)}{v_c(\omega)}$	$\frac{1}{V_R}$	$\frac{1}{V_R}$	$\frac{1}{V_R}$
$F_{m-} = \frac{d(\omega_p - \omega_s)}{v_c(\omega_p)}$	$\frac{e^{jD2\pi}}{V_R}$	$\frac{e^{-jD2\pi}}{V_R}$	$\frac{-\cos(D\pi)}{V_R}$
$F_{m+} = \frac{d(\omega_p)}{v_c(\omega_p - \omega_s)}$	$\frac{e^{-jD2\pi}}{V_R}$	$\frac{e^{jD2\pi}}{V_R}$	$\frac{-\cos(D\pi)}{V_R}$

Clearly, the describing function of the PWM comparator for the same frequency input and output is a constant gain for all the three cases. It is not a function of T_r or T_f. Therefore, for the same input and output frequency, the modulation types do not change the function of the PWM comparator.

For the extended describing functions between different frequencies, when the duty cycle changes, the phases change accordingly, while the magnitudes are constant for trailing-edge and leading-edge modulations. However, for the double-edge modulation, the magnitude is a function of the duty cycle. Assuming the triangle ramp peak-to-peak voltage, V_R, is 1 V, Figure A.3 illustrates the magnitude of F_{m+} and F_{m-}.

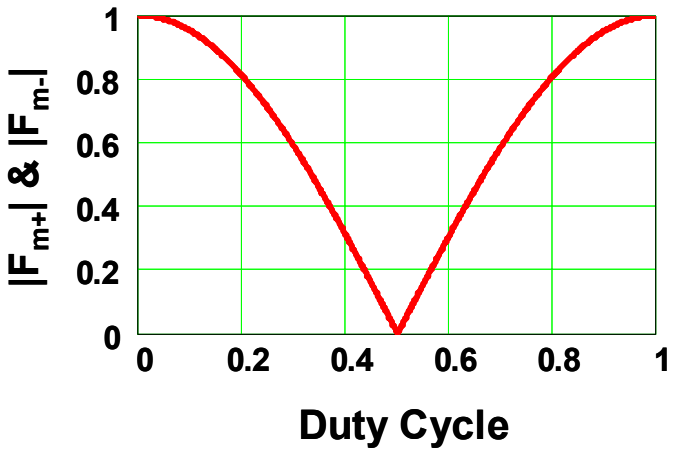

Figure A.3. Magnitude of F_{m+} and F_{m-} as a function of the duty cycle for the double-edge modulation.

Applying the derived result in Table 3.1 on the open-loop single-phase buck converter with control-voltage perturbation, the generalized multi-frequency model is shown in Figure A.4. The sideband component at output voltage is derived as

$$V_o(\omega_p - \omega_s) = F_{m-} V_{in} G_{LC}(\omega_p - \omega_s) \tag{A.3}$$

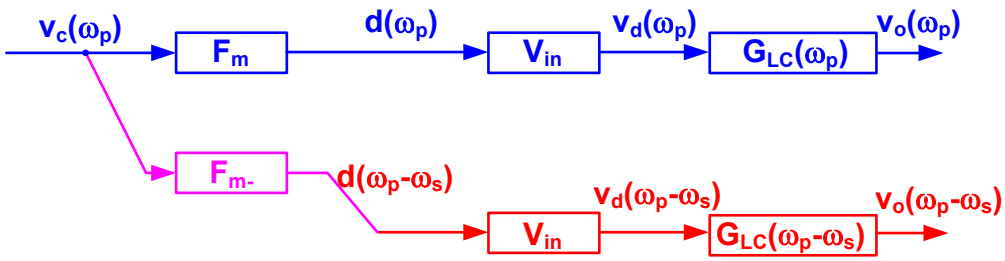

Figure A.4. The generalized multi-frequency model of a single-phase open-loop buck converter.

Because F_{m-} varies with the duty cycle for the double-edge modulator, the resulted $V_o(f_p\text{-}f_s)$ component is different for the three modulation schemes with the same control-voltage perturbations. Figure A.5 shows the simulation results of the 1-MHz open-loop single-phase converter running with a 20% duty cycle and 5-mV 990-kHz control voltage perturbation. In cases where the trailing-edge and leading-edge modulations have the same 136-mV magnitude of 10-kHz components at V_o, there is smaller 10-kHz component of 113 mV with the double-edge modulation.

Furthermore, according to Figure A.3, the sideband component can be fully cancelled when the duty cycle is exactly equal to 50% with double-edge modulation. As verified by the simulation results shown in Figure A.6, the closer the duty cycle is to 50%, the smaller magnitude of the output voltage sideband component at 10 kHz.

For the buck converter with voltage-mode control, the modulation schemes also influence the performance. With the generalized multi-frequency model as in Figure A.7, the effective loop gain is calculated as

$$T_v(\omega_p) = T_{av}(\omega_p)\left(1 - \frac{F_{m+}F_{m-}}{F_m^{\,2}} \cdot \frac{T_{av}(\omega_p - \omega_s)}{1 + T_{av}(\omega_p - \omega_s)}\right). \tag{A.4}$$

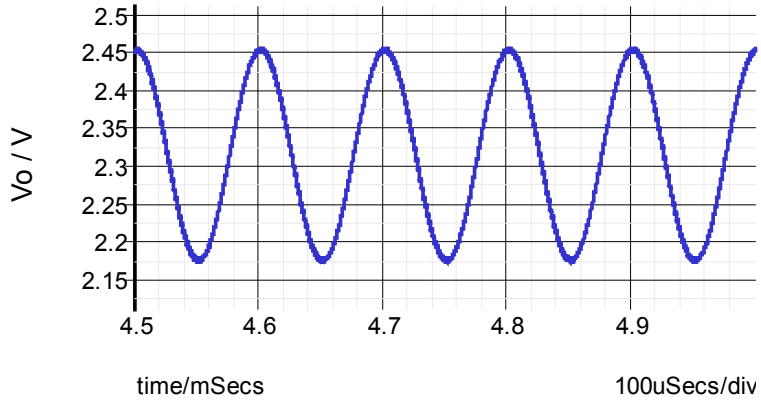

(a) Trailing-edge modulation.

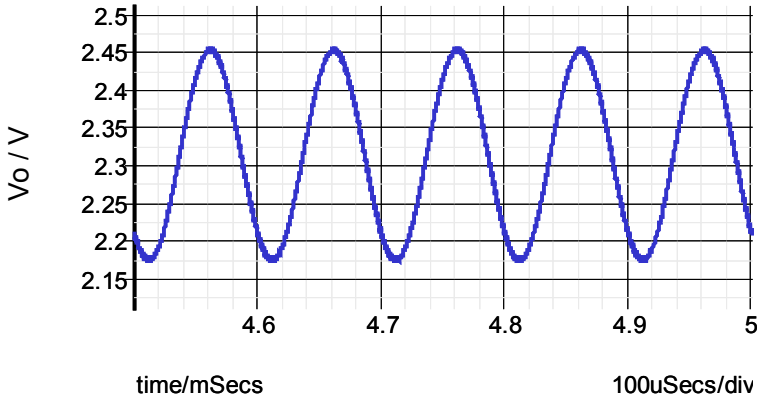

(b) Leading-edge modulation.

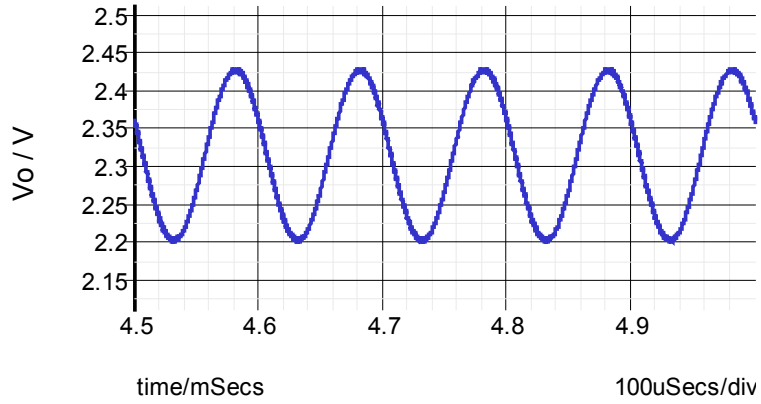

(c) Double-edge modulation.

Figure A.5. Simulated V_o waveforms with 20% duty cycle for 1-MHz open-loop buck converters with 990-kHz V_c perturbations and different modulation schemes.

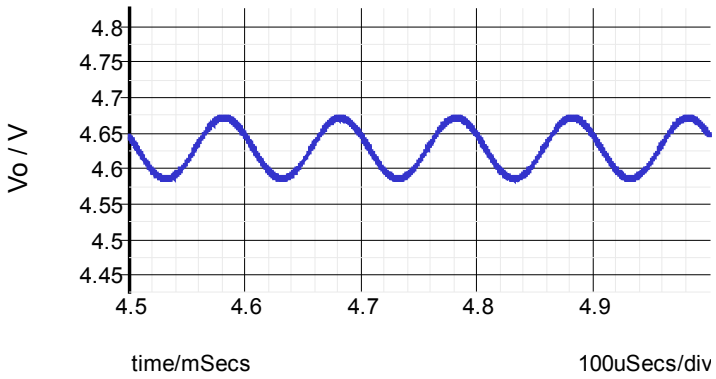

(a) *D*=40%.

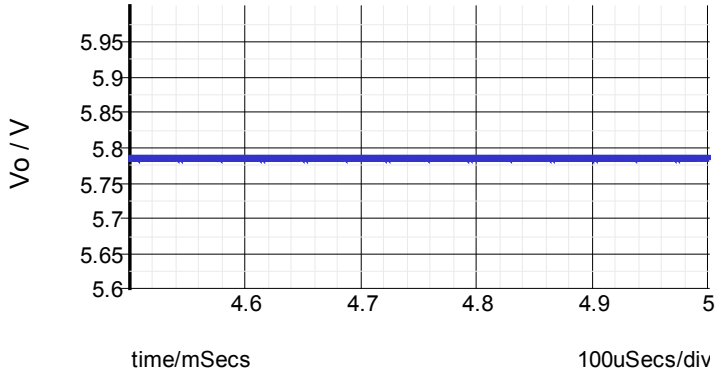

(b) *D*=50%.

Figure A.6. Simulated V_o waveforms for 1-MHz open-loop buck converters with 990-kHz V_c perturbations and the double-edge modulation.

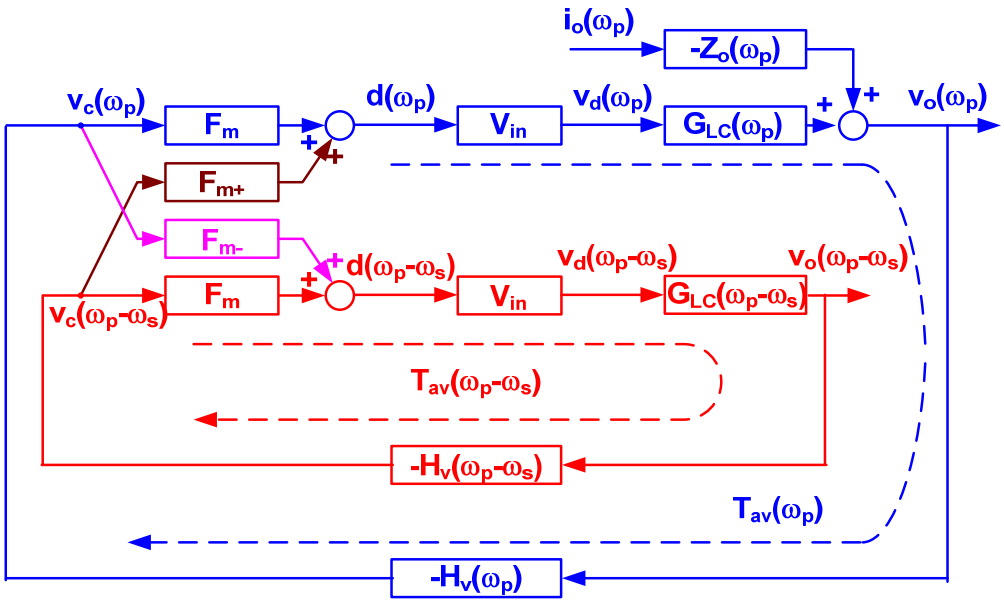

Figure A.7. The generalized multi-frequency model of a voltage-mode-controlled buck converter.

Since the loop gain's magnitude and phase reductions around the switching frequency are caused by the sideband effect represented by the second term, the bandwidth is strongly dependent on the coupling coefficients of F_{m+} and F_{m-}. From Table 3.1, $F_{m+} \cdot F_{m-}$ for the trailing-edge and leading-edge modulations is independent from the duty cycle, D. However for the double-edge modulation, it changes with D.

Assuming V_R=1, Figure A.8 shows the relative magnitudes of $F_{m+} \cdot F_{m-}$ as a function of the duty cycle. Unlike the other two modulations, the double-edge modulation has the ability to cancel the sideband effect when the duty cycle is 50%. Consequently, there is less sideband effect for the double-edge modulations when the duty cycle is close to 50%.

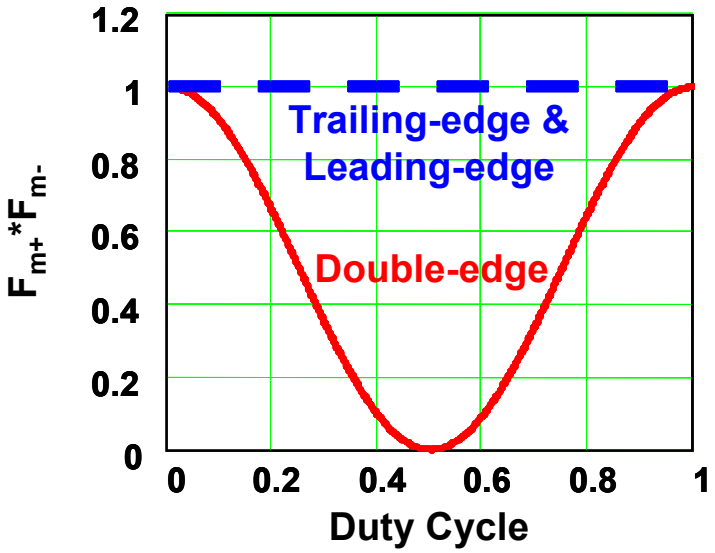

Figure A.8. Comparison of the magnitude of sideband effect, $F_{m+}*F_{m-}$, assuming V_R=1.
(Red solid line: double-edge modulation; Blue dotted line: trailing-edge and leading-edge modulation.)

As shown in Figure A.9, for the same bandwidth and a 50% duty cycle, more phase margin is achieved with the double-edge modulation as compared with the trailing-edge and leading-edge modulations. However, with a small duty cycle of 10%, the cancellation of the sideband effect is insignificant. This phase margin improvement with the double-edge modulation is strongly depended on the operation duty cycle. The benefit is maximized only when the duty cycle is around 50%, however, this is not likely to happen in VR applications.

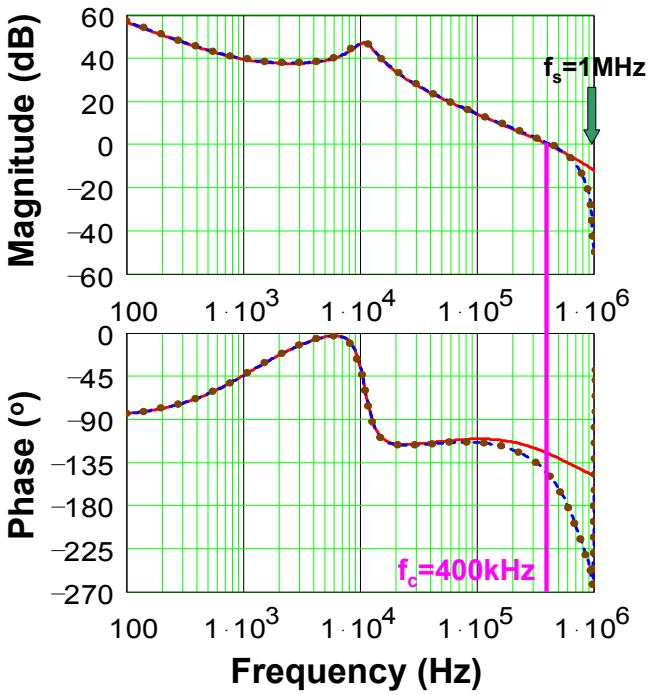

(a) D=50%.

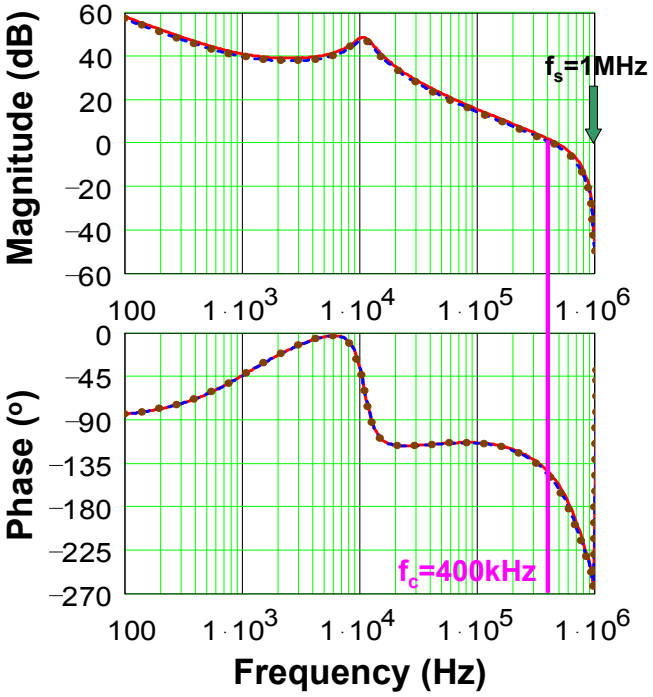

(b) D=10%.

Figure A.9. Loop gain comparison among PWM methods.

(Red solid line: double-edge modulation; Blue dashed line: trailing-edge modulation; Brown dotted line: leading-edge modulation.)

With 12-V input voltage, most VRs operate with a steady-state duty cycle around 10-15%. In some applications, such as the two-stage solution or the laptop systems, the duty cycle might be larger with lower input voltage. However, during the load transient from the microprocessors, the duty cycle of the VR may be saturated. In the practical design, all the possible operating conditions should be considered when pushing the bandwidth. Therefore, the benefit from the double-edge modulation is limited.

In summary, when the duty cycle is around 50%, the double-edge modulation can cancel the sideband effect for the buck converters. However, the cancellation is insignificant when the duty cycle is small. Therefore, in practical designs, the advantage is limited for pushing the control-loop bandwidth.

Appendix B. Analyses with Input-Voltage Variations

In the previous discussions, it is assumed that the input voltage of the buck or multiphase buck converter is constant. The nonlinearity of the switch function has not been considered. By this way, the function of the switches can be regarded as a simple gain. In this appendix, the detailed model of the switches is derived considering the influence of the input-voltage variations.

As an example, the converter with the trailing-edge modulation is considered. For simplicity, the case for an open-loop buck converter with only the input perturbation is studied first, as shown in Figure B.1. With only the input-voltage perturbation, the phase voltage waveform is illustrated as in Figure B.2.

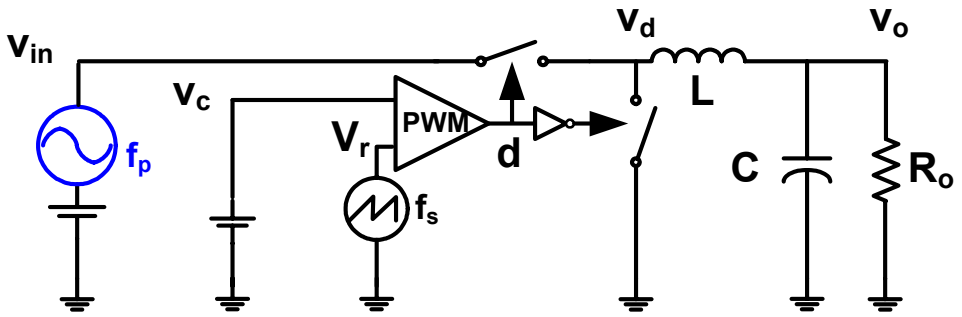

Figure B.1. An open-loop buck converter with the input-voltage perturbations.

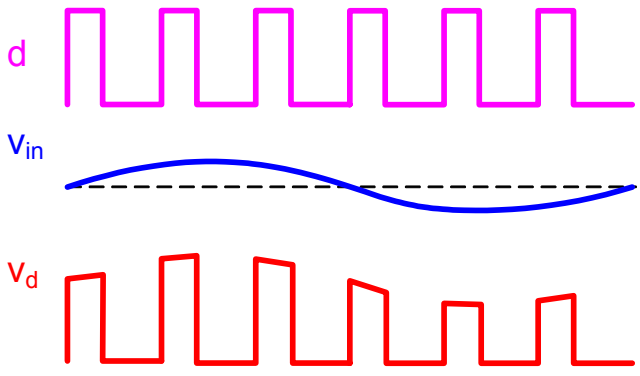

Figure B.2. The phase voltage waveform with the input-voltage perturbation assuming a constant duty cycle.

In this case, the nonlinearity exists because of the switches shown in Figure B.3. To obtain the extended describing functions for the switches, the similar approach of modeling the PWM comparator using the Fourier analysis is applied.

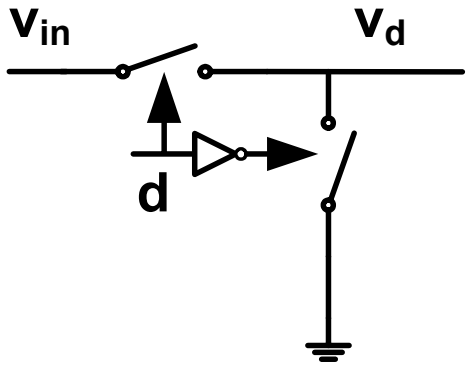

Figure B.3. Switches in the converters.

With a sinusoidal input voltage of

$$v_{in}(t) = V_{in} + \hat{v}_{in}\sin(\omega_p t - \theta), \tag{B.1}$$

it is assumed that the perturbation frequency, ω_p, and the switching frequency, ω_s, have the relationship of

$$\frac{\omega_p}{\omega_s} = \frac{N}{M}. \tag{B.2}$$

where N and M are positive integers. Then the Fourier coefficient at ω_p for the phase voltage is expressed as

$$v_d(\omega_p) = \frac{1}{2\pi N}\sum_{k=1}^{M}\int_{(k-1)\omega_p T_s}^{(k-1)\omega_p T_s+\omega_p D T_s} v_{in}(t)e^{-j\omega_p t}\,d(\omega_p t). \tag{B.3}$$

It is obtained that when $\omega_p \neq k\omega_s/2$, k=1, 2, 3, …,

$$v_d(\omega_p) = Dv_{in}(\omega_p). \tag{B.4}$$

Meanwhile,

$$v_d(\omega_p-\omega_s)=\frac{1}{2\pi(N-M)}\sum_{k=1}^{M}\int_{(k-1)(\omega_p-\omega_s)T_s}^{(k-1)(\omega_p-\omega_s)T_s+(\omega_p-\omega_s)DT_s} v_{in}(t)e^{-j(\omega_p-\omega_s)t}d((\omega_p-\omega_s)t). \quad \text{(B.5)}$$

It is derived that when $\omega_p \neq k\omega_s/2$, k=1, 2, 3, …,

$$v_d(\omega_p-\omega_s)=\frac{e^{j2\pi D}-1}{2j\pi}v_{in}(\omega_p), \quad \text{(B.6)}$$

Similarly, it is obtained that

$$v_d(\omega_p)=\frac{e^{-j2\pi D}-1}{-2j\pi}v_{in}(\omega_p-\omega_s). \quad \text{(B.7)}$$

These extended describing functions are summarized in Table B.1. The relationship between the same frequency input and output components is a simple gain of duty cycle, which is the same as the result from the average model. The extended describing functions between different frequencies are illustrated in Figure B.4.

For the case as Figure B.1, the model for the circuit is illustrated in Figure B.5. To verify the relationship between different frequencies components, the switching-model simulation with input sinusoidal perturbations are performed. A 999-kHz perturbation is inserted to the input voltage of a 1-MHz buck converter with 1.2-V output, 80-mΩ load resistor, 200-nH inductor, and 1-mF capacitor.

Table B.1. Extended describing functions from the input voltage to the phase voltage.

		Output components	
		$v_d(\omega_p)$	$v_d(\omega_p-\omega_s)$
Input components	$v_{in}(\omega_p)$	D	$\frac{e^{j2\pi D}-1}{2j\pi}$
	$v_{in}(\omega_p-\omega_s)$	$\frac{e^{-j2\pi D}-1}{-2j\pi}$	D

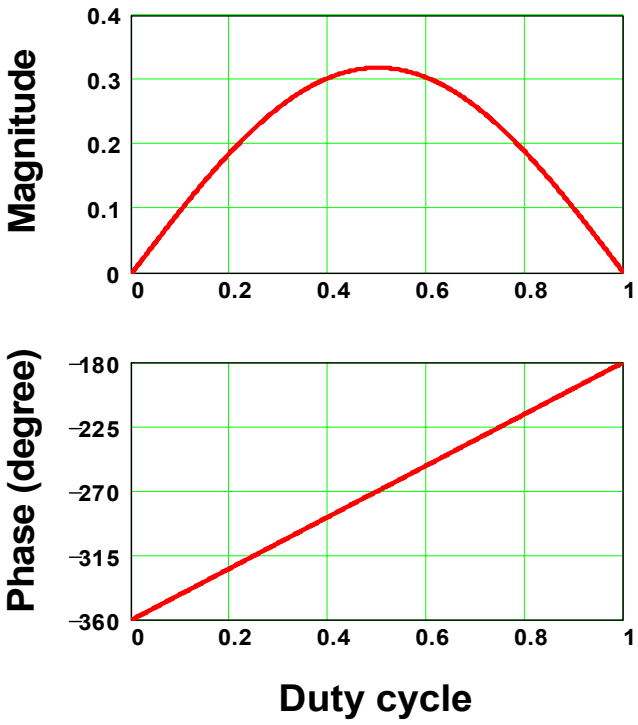

Figure B.4. Describing function of $v_d(\omega_p-\omega_s)/v_{in}(\omega_p)$.

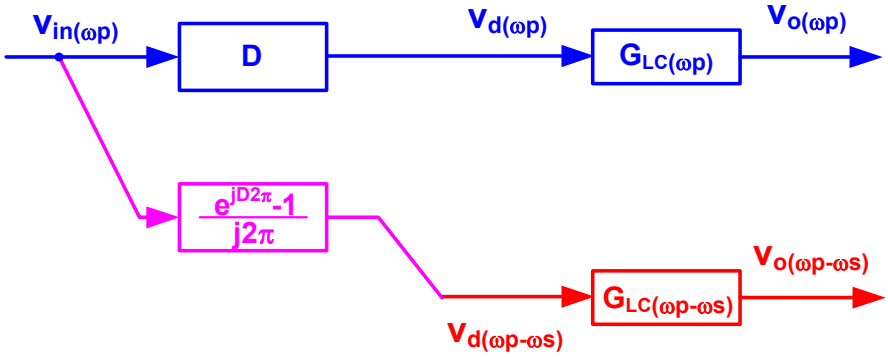

Figure B.5. Multi-frequency model of the buck converter considering the input-voltage perturbation.

The sideband component of the 1-kHz component at the output voltage is measured. Compared with the calculated value, Figure B.6 demonstrates the validity of the model.

It is complicated when there are both perturbations at the control voltage and the input voltage. For the case as shown in Figure B.7, there are two nonlinearities. The nonlinearity of the PWM comparator can be modeled the same way as in Chapter 3. The nonlinearity of the switches is discussed as follows.

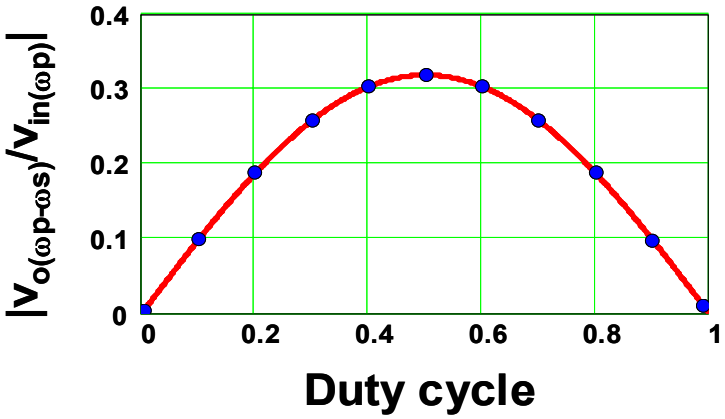

Figure B.6. Comparison between the simulation and modeling with the input-voltage perturbation. (Red solid line: prediction using multi-frequency model; Blue dots: switching-model simulation results.)

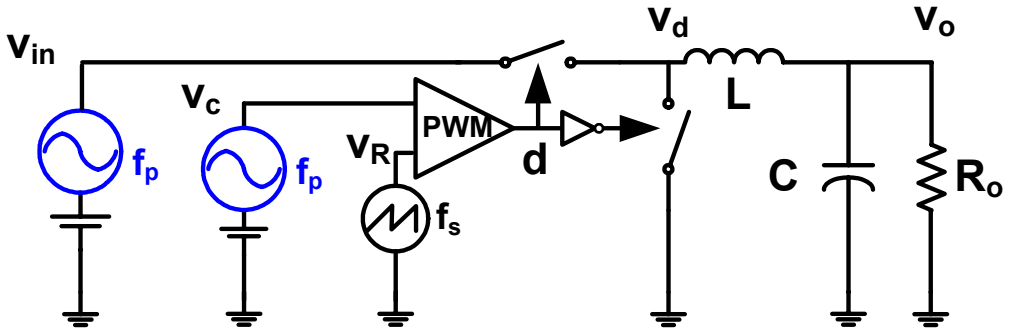

Figure B.7. Buck converter with perturbations at both the control voltage and input voltage.

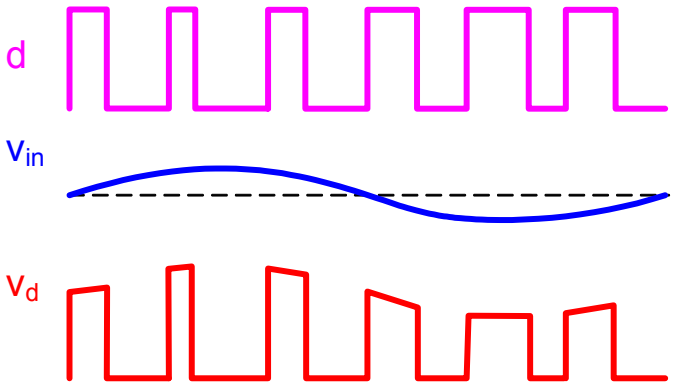

Figure B.8. Function of the switches in the buck converters.

As shown in Figure B.8, the function of the switches is

$$v_d(t) = v_{in}(t) \text{ when } d(t) = 1, \tag{B.8}$$

$$v_d(t) = 0 \text{ when } d(t) = 0. \tag{B.9}$$

Therefore, the phase voltage can be expressed by

$$v_d(t) = d(t) \cdot v_{in}(t). \tag{B.10}$$

In the frequency domain, the relationship is represented by the convolution,

$$v_d(\omega) = d(\omega) \otimes v_{in}(\omega). \tag{B.11}$$

It is rewritten as

$$v_d(\omega_p) = d(0) \cdot v_{in}(\omega_p) + d(\omega_p) \cdot v_{in}(0) + \ldots. \tag{B.12}$$

With small signal assumption, the higher order components are ignored. Therefore, it is obtained that

$$v_d(\omega_p) = D \cdot v_{in}(\omega_p) + d(\omega_p) \cdot V_{in}, \tag{B.13}$$

and

$$v_d(\omega_p - \omega_s) = D \cdot v_{in}(\omega_p - \omega_s) + d(\omega_p - \omega_s) \cdot V_{in}. \tag{B.14}$$

Therefore, the super-positioning can be used to address perturbations from both the input voltage and control voltage. With (B.14), the multi-frequency model including the nonlinearities of both the PWM comparator and the switches is illustrated in Figure B.9.

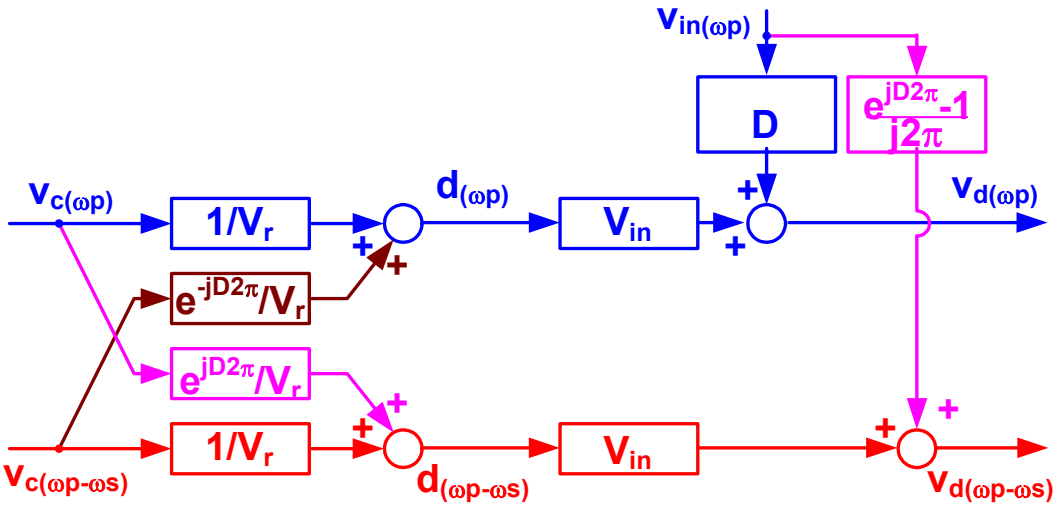

Figure B.9. Multi-frequency model of the nonlinearities of the buck converter.

Based on the previous analysis, a voltage-mode-controlled buck converter with the input-voltage perturbation is modeled, as in Figure B.10. It is derived that the audio-susceptibility considering the sideband effect is

$$\frac{v_o(\omega_p)}{v_c(\omega_p)}=\frac{D\cdot G_{LC}(\omega_p)}{1+\dfrac{T_{av}(\omega_p)}{1+T_{av}(\omega_p-\omega_s)}}+\frac{\dfrac{e^{-jD2\pi}-1}{2j\pi}\cdot G_{LC}(\omega_p)\cdot T_{av}(\omega_p-\omega_s)}{1+T_{av}(\omega_p)+T_{av}(\omega_p-\omega_s)}. \tag{B.15}$$

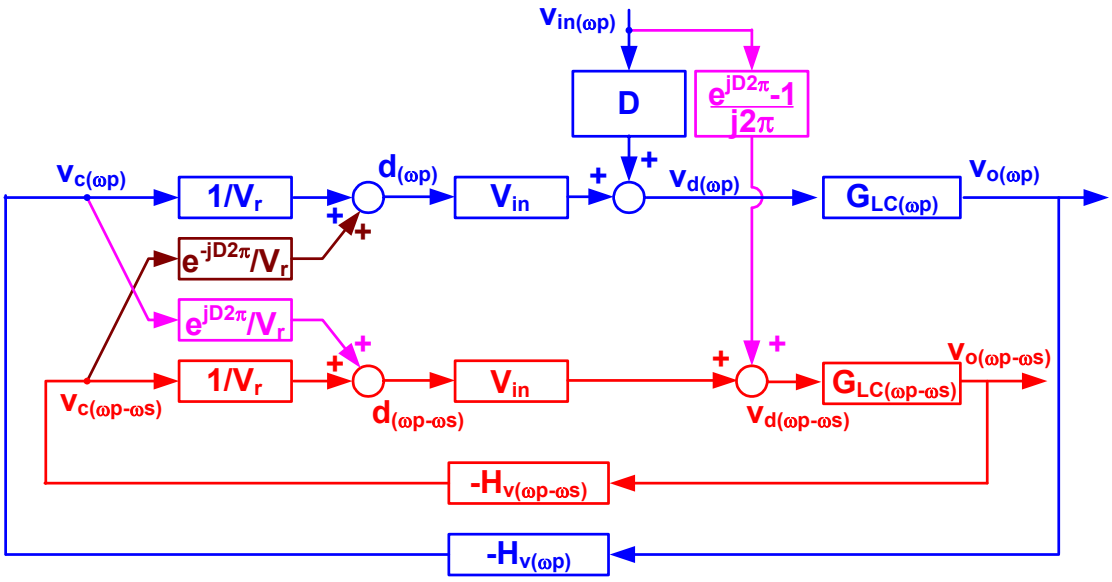

Figure B.10. Multi-frequency model of a voltage-mode-controlled buck converter with the input-voltage perturbation.

The comparison of the closed-loop audio-susceptibility is shown in Figure B.11. Clearly, the average model is accurate compared with the simulation result in the low-frequency range. However, because of the existing sideband effect, the high-frequency performance can only be predicted by the multi-frequency model.

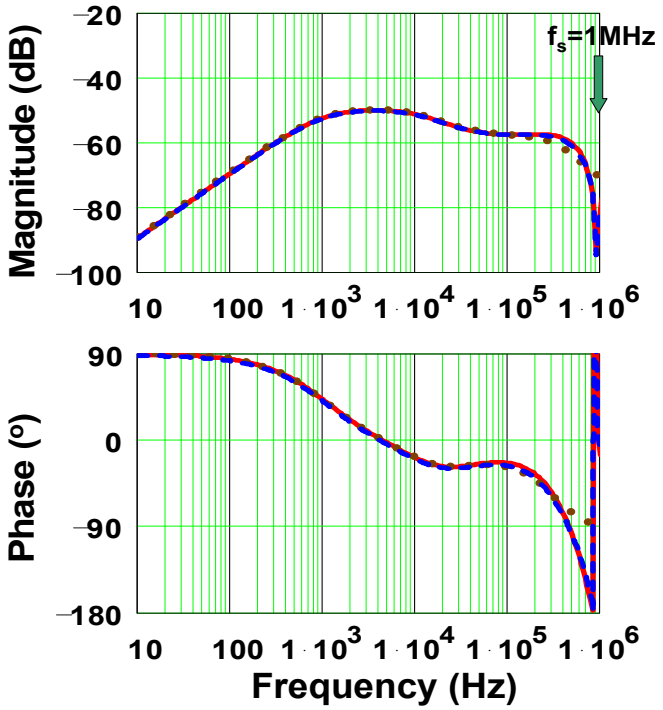

(a) D=10%.

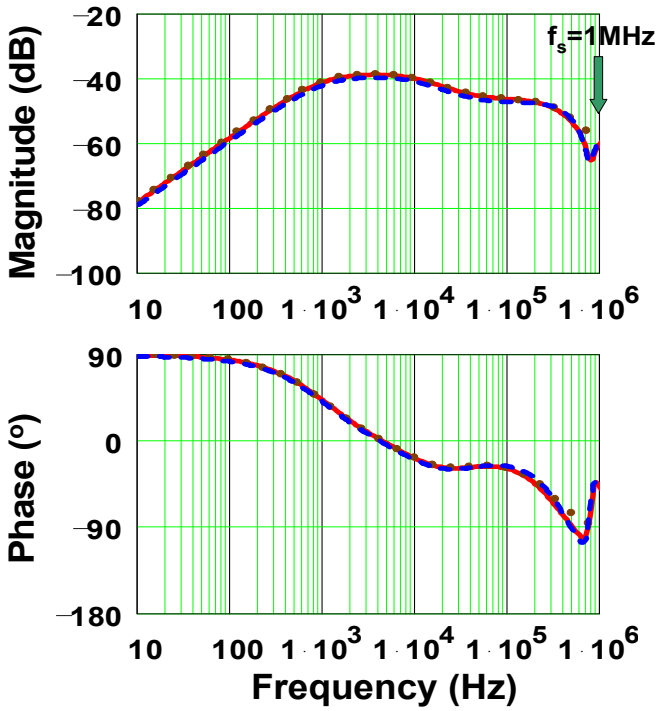

(b) D=40%.

Figure B.11. Comparison of the closed-loop audio-susceptibility.

(Red solid line: SIMPLIS simulation result; Blue dashed line: average-model result; Brown dotted line: multi-frequency model result)

References

[1] R. Hiremane, "From Moore's Law to Intel Innovation—Prediction to Reality," *Technology@Intel Magazine*, April 2005.

[2] D. P. Jajeh, "Intel Accelerates in A New Direction," *Circuit Posted*, November 2004.

[3] Intel Corporation, "Platform 2015: Intel Processor and Platform Evolution for the Next Decade," *Intel White Paper*, March 2005.

[4] B. Crepps, "Building the Multi Building the Multi-Core Future: Power Efficient Architecture," *Intel Developer Forum*, August 2005.

[5] E. Stanford, "New Processors Will Require New Powering Technologies," *Magazine of Power Electronics Technology*, Feburary 2002, pp. 32-42.

[6] E. Stanford, "Microprocessor Roadmap," *Intel Power Summit*, August 2005.

[7] A. Rozman, and K. Fellhoelter, "Circuit Considerations for Fast Sensitive, Low-Voltage Loads in a Distributed Power System," *IEEE APEC*, 1995, pp. 33-42.

[8] M. Zhang, M. Jovanovic, and F. C. Lee, "Design Considerations for Low-Voltage On-board DC/DC Modules for Next Generations of Data Processing Circuits", *IEEE Transactions on Power Electronics*, March 1996, pp. 328-337.

[9] F. Goodenough, "Advanced Microprocessors Demand Amperes of Current at <2V," *Electronic Design*, January 20th, 1997.

[10] X. Zhou, X. Zhang, J. Liu, P.-L. Wong, J. Chen, H. Wu, L. Amoroso, F. C. Lee, and D. Chen, "Investigation of Candidate VRM Topologies for Future Microprocessors," *IEEE APEC*, 1998, pp. 145-150.

[11] X. Zhou, P.-L. Wong, R. Watson, L. Amoroso, X. Sun, H. Wu, P. Xu, B. Yang, W. Chen, M. Donati, F. C. Lee and A. Q. Huang, "Voltage Regulator Module for Future Generation of Processors," *VPEC Annual Seminar Tutorial*, 1998.

[12] X. Zhou, "Low-Voltage High-Efficiency Fast-Transient Voltage Regulator Module," *Ph.D Dissertation*, Virginia Tech, Blacksburg, VA, July 1999.

[13] P. Xu, X. Zhou, P.-L. Wong, K. Yao, and F. C. Lee, "Design and Performance Evaluation of Multi-Channel Interleaving Quasi-Square-Wave Buck Voltage Regulator Module," *HFPC*, 2000, pp. 82-88.

[14] Intel Corporation, "Voltage Regulator-Down (VRD) 10.1 Design Guide for Desktop LGA775 Socket," *Intel Design Guides*, April 2005.

[15] Y. Ren, K. Yao, M. Xu, and F. C. Lee, "Analysis of the Power Delivery Path from the 12-V VR to the Microprocessor," *IEEE Transactions on Power Electronics*, November 2004, pp. 1507-1514.

[16] Y. Ren, "High Frequency, High Efficiency Two-Stage Approach for Future Microprocessors," *Ph.D Dissertation*, Virginia Tech, Blacksburg, VA, April 2005.

[17] L. Amoroso, M. Donati, X. Zhou, and F. C. Lee, "Single Shot Transient Suppressor (SSTS) for High Current High Slew Rate Microprocessor," *IEEE APEC*, 1999, pp. 284-288.

[18] A. M. Wu, and S. R. Sanders, "An Active Clamp Circuit for Voltage Regulation Module (VRM) Applications," *IEEE Transactions on Power Electronics*, September 2001, pp. 623-634.

[19] A. Barrado, R. Vazquez, E. Olias, A. Lazaro, and J. Pleite, "Theoretical Study and Implementation of a Fast Transient Response Hybrid Power Supply," *IEEE Transactions on Power Electronics*, July 2004, pp. 1003-1009.

[20] Y. Ren, A. Schmit, M. Xu, F. C. Lee, A. Sharma, X. Wu, and K. D. Ngo, "Hybrid Power Filter with Output Impedance Control," *IEEE PESC*, 2005, pp. 1434-1440.

[21] K. Yao, K. Lee, M. Xu, and F. C. Lee, "Optimal Design of the Active Droop Control Method for the Transient Response," *IEEE APEC*, 2003, pp.718-723.

[22] P.-L. Wong, F. C. Lee, P. Xu, and K. Yao, "Critical Inductance in Voltage Regulator Modules," *IEEE Transactions on Power Electronics*, July 2002, pp. 485-492.

[23] P.-L. Wong, "Performance Improvements of Multi-Channel Interleaving Voltage Regulator Modules with Integrated Coupling Inductors," *Ph.D Dissertation*, Virginia Tech, Blacksburg, VA, March 2001.

[24] K. Yao, M. Xu, Y. Meng, and F. C. Lee, "Design Considerations for VRM Transient Response Based on the Output Impedance," *IEEE Transactions on Power Electronics*, November 2003, pp. 1270-1277.

[25] K. Yao, "High-Frequency and High-Performance VRM Design for the Next Generations of Processors," *Ph.D Dissertation*, Virginia Tech, Blacksburg, VA, April 2004.

[26] G. W. Wester, and R. D. Middlebrook, "Low-Frequency Characterization of Switched DC-DC converters," *IEEE Transactions on Aerospace and Electronic Systems*, May 1973, pp. 376-385.

[27] R. D. Middlebrook, and S. Cuk, "A General Unified Approach to Modeling Switching-Converter Power Stage," *IEEE PESC*, 1976, pp. 18-34.

[28] A. R. Brown, and R. D. Middlebrook, "Sampled-Data Modeling of Switching Regulators," *IEEE PESC*, 1981, pp. 349-369.

[29] R. Tymerski, "Frequency Analysis of Time-Interval-Modulated Switched Networks," *IEEE Transactions on Power Electronics*, April 1991, pp. 287-295.

[30] R. Tymerski, "Application of the Time Varying Transfer Function for Exact Small-Signal Analysis," *IEEE Transactions on Power Electronics*, March 1994, pp. 196-205.

[31] D. J. Perreault, and G. C. Verghese, **"**Time-Varying Effects and Averaging Issues in Models for Current-Mode Control," *IEEE Transactions on Power Electronics*, May 1997, pp. 453-461.

[32] V. J. Thottuvelil, and G. C. Verghese, "Simulation-Based Exploration of Aliasing Effects in PWM Power Converters," *IEEE Workshop on Computers in Power Electronics*, 1998, pp. 19-22.

[33] G. C. Verghese, and V. J. Thottuvelil, "Aliasing Effects in PWM Power Converters," *IEEE PESC*, 1999, pp. 1043-1049.

[34] R. D. Middlebrook, **"**Describing Function Properties of a Magnetic Pulse-Width Modulator," *IEEE Transactions on Aerospace & Electronic Systems*, May 1973, pp. 386-398.

[35] Hewlett-Packard Company, *Operating and Service Manual for Model 3570A Network Analyzer*, 1977.

[36] J. Groves, "Small Signal Analysis of Nonlinear Systems with Periodic Operating Trajectories," *Ph.D Dissertation*, Virginia Tech, Blacksburg, VA, April 1995.

[37] Transim Technology Corporation, "Power Design Tools," *SIMPLIS Technical Reference Manual*, 1994.

[38] A. R. Brown, and R. D. Middlebrook, "Sampled-Data Modeling of Switching Regulators," *IEEE PESC*, 1981, pp. 349-369.

[39] B. Y. Lau, and R. D. Middlebrook, "Small-Signal Frequency Response Theory for Piecewise-Constant Two-Switched-Network DC-to-DC Converter Systems," *IEEE PESC*, 1986, pp. 186-200.

[40] G. C. Verghese, C. A. Bruzos, and K. N. Mahabir, "Averaged and Sampled-Data Models for Current Mode Control: A Re-Examination," *IEEE PESC*, 1989, pp. 484-491.

[41] R. B. Ridley, "A New, Continuous-Time Model for Current-Mode Control," *IEEE Transactions on Power Electronics*, April 1991, pp. 271-280.

[42] E. X. Yang, F. C. Lee, and M. M. Jovanovic, "Small-Signal Modeling of Power Electronic Circuits Using Extended Describing Function Technique**,"** *VPES Seminar*, 1991, pp. 167-178.

[43] E. X. Yang, F. C. Lee, and M. M. Jovanovic, "Small-Signal Modeling of Series and Parallel Resonant Converters**,"** *IEEE APEC*, 1992, pp. 785-792.

[44] E. X. Yang, F. C. Lee, and M. M. Jovanovic, "Small-Signal Modeling of LCC Resonant Converter ," *IEEE PESC*, 1992, pp. 941-948.

[45] J. Groves, "Small-Signal Analysis Using Harmonic Balance Methods," *IEEE PESC*, 1991, pp. 74-79.

[46] R. D. Middlebrook, "Predicting Modulator Phase Lag in PWM Converter Feedback Loops," *Eighth International Solid-State Power Conversion Conference (Powercon 8)*, 1981, pp. H4.1-H4.6.

[47] Delta Electronics, *Power Inductor SPL146 Type Specifications*.

[48] Panasonic, *Power Choke Coil PCCN6B Specifications*.

[49] Linear Technology, "3-Phase Buck Controller for Intel VRM9/VRM10 with Active Voltage Positioning," *LTC3738 Datasheet*, 2004.

[50] Texas Instruments, "High-Frequency, Multiphase Controller," *TPS40090 Datasheet*, 2004.

[51] Analog Devices, "6-Bit Programmable 2/3/4-Phase Synchronous Buck Controller," *ADP3168 Datasheet*, 2004.

[52] Maxim, "VRM 9.0, Dual-Phase, Parallelable, Average Current-Mode Controller," *MAX5037 Datasheet*, 2004.

[53] P.-L. Wong, Q. Wu, P. Xu, B. Yang, and F. C. Lee, "Investigating Coupling Inductor in Interleaving QSW VRM," *IEEE APEC*, 2000, pp. 973-978.

[54] J. Zhou, M. Xu, and F. C. Lee, "Small Signal Modeling of a High Bandwidth Voltage Regulator Using Coupled Inductors," *IEEE PESC*, 2005, pp.2790-2796.

[55] J. Zhou, "High Frequency, High Current Density Voltage Regulators," *Ph.D Dissertation*, Virginia Tech, Blacksburg, VA, April 2005.

[56] P. Harriman, "New Control Method Boosts Multiphase Bandwidth," *Power Electronics Technology*, January 2003, pp. 36-45.

Vita

The author, Yang Qiu, was born in Beijing, China, in 1976. He received his Bachelor and Master degrees in Electrical Engineering from Tsinghua University, Beijing, China, in 1998 and 2000, respectively.

Since fall 2000, the author has been working toward the Ph.D. degree in the Center for Power Electronics Systems (CPES) at Virginia Polytechnic Institute and State University, Blacksburg, Virginia. His research interests include modeling and control of converters, high-frequency power conversion, low-voltage high-current conversion techniques, resonant converters, and distributed power system.